Study of the Superconducting Properties of Some Rare-Earth and Transition Metal Borides with Quasi-low-dimensional Crystal Structures

Jaskaran Singh

A thesis submitted for the partial fulfillment of
the degree of Doctor of Philosophy

Department of Physical Sciences
Indian Institute of Science Education and Research (IISER) Mohali
Knowledge city , sector 81, SAS Nagar, Manauli PO, Mohali 140306, Punjab, India

August 2022

To my parents

Declaration

The work presented in this thesis has been carried out by me under the guidance of Dr. Yogesh Singh at the Indian Institute of Science Education and Research Mohali. This work has not been submitted in part or in full for a degree, a diploma, or a fellowship to any other university or institute. Whenever contributions of others are involved, every effort is made to indicate this clearly, with due acknowledgment of collaborative research and discussions. This thesis is a bonafide record of original work done by me and all sources listed within have been detailed in the bibliography.

Jaskaran Singh
(Candidate)

In my capacity as the supervisor of the candidate's thesis work, I certify that the above statements by the candidate are true to the best of my knowledge.

Dr. Yogesh Singh
(Supervisor)

Acknowledgments

My journey to complete this thesis is replete with personalities and experiences that helped shape this document to its final form. It is a pleasure to be able to finally thank all those people who have supported and helped me during this journey.

First and foremost, I would like to express my sincere gratitude to Dr. Yogesh Singh, my thesis supervisor, for allowing me to work in his excellent research group and for providing an open and scientific learning atmosphere. Without his advice and involvement, the work that I have carried out during my Ph.D. would not have been possible. His constant support and guidance helped me throughout the research and writing of this thesis.

I would also like to thank my doctoral committee members, Dr. Sanjeev Kumar and Dr. Goutam Sheet, for their help and insightful comments during this journey. I would also like to thank Dr. Abhishek Chaudhuri for his support and encouragement. I would like to acknowledge our collaborators, Dr. D. Srivastava (Central University of Rajasthan), Prof. A. Thamizhavel (Tata Institute of Fundamental Research, Mumbai), and Dr. Ritu Gupta (PSI, Zurich), for their help and support. I would also like to acknowledge our collaborators at IISER Mohali, Dr. S. Gayen, Dr. M. Aslam, Anooja Jayaraj, Soumya Datta, and Dr. Goutam Sheet. Their invaluable support made it possible to conduct this research. My sincere thank to Soumya Datta for giving his time for discussions.

I would like to especially thank Dr. Anzar Ali and Dr. Gaurav Sharma for sitting with me till late at night to help me with various data analysis and measurements. Without their help, it is impossible to imagine this document in its final form.

I am also grateful to Dr. Jaskaran Singh Nirankari and Dr. Kirandeep Kaur for their suggestions on the thesis writing. I would like to thank Dr. Varinder Singh, who has always been a source of inspiration due to his hard-working attitude and for always helping me whenever I needed it. I would also like to thank Harwinder Singh for helping me with the graphics.

Besides the above, I would like to acknowledge my other lab members with whom I have had a wonderful time. I thank Dr. Kavita Mehlawat, Dr. Ashwini Balodhi, Dr. Amit Vashist, Shama, Anooja Jayaraj, Charanpreet Singh, Kavita Chaudhary, Ankit Labh, Pradeep Yadav, Vipul, Savita, Barkha, Sarvesh and Shubhankar for their help and cooperation. I am grateful to Anooja Jayraj for assisting me in the projects. I sincerely thank Shama for her help with the sealing of the quartz tubes. I am also grateful to other postdoctoral fellows in our group, Dr. Gyaneshwar, Dr. R.K. Gopal, and Dr. Ritu Rawat.

I am also grateful to our former Head of the Department (HOD), Prof. Sudeshna Sinha, for her kind support and help in starting this journey.

A special thanks to my teachers Mrs. Davinder Kohli, Dr. S.L. Verma, Dr. Vishwamitter, and Dr. Sandeep Sehajpal, for their constant motivation throughout my career.

I would like to thank Prof. Arvind (Vice-Chancellor, Punjabi University Patiala) for his constant support and encouragement.

This journey would have been extremely stressful if not for the IISER community. The time spent with the above lab mates and my friends Deepak, Rakesh, Mayank, Subendhu, Suman, Feroz, Gurdeep, Jagmeet, Varinder Bhagat, Keshav, Satnam, Arash, Preetinder, Sheesh Ram, Yashpreet, Harpreet, Sailesh, Ramu, Sumit, Shyaam, Kirat, Haritha, Jasleen, Guratinder, will be sorely missed. I would also like to thank my friends from outside IISER, especially Varinder, Manoj, and Kashmir. My sincere gratitude to my dear friend Mr. Feroz Ahmed. It would have been very difficult for me to finish my work at IISER without his constant support.

I would like to take this opportunity to thank our former Director, Professor N. Sathyamurthy, offices of Dean Academics and Dean R&D, for granting me leave for joining Punjabi University Patiala as an Assistant Professor and simultaneously allowing me to pursue my Ph.D.

I am also thankful to IISER Mohali for providing the XRD facility and other research facilities. I would like to acknowledge the use of the PPMS Sonipat (CFMS 14T, Cryogenic Ltd.), Central Research Facility, IIT Delhi for transport measurements. I acknowledge the library at IISER Mohali and the computer department for their direct and indirect support in my work at IISER.

I acknowledge the financial support provided by UGC-CSIR, India.

Last but the most significant are my parents, who believed in me and supported me with unconditional love throughout my life. There are no words to express my gratitude to my parents. It is because of their love and blessings that I have been able to complete this work.

Abstract

The phenomenon of superconductivity has been studied intensively not only for the fundamental physics involved but also for the promise of technological applications. The transition from the normal to the superconducting phase is accompanied by remarkable changes in measurable properties like electric transport, magnetization, and heat capacity, among others. Measurements of these properties provide a powerful tool to address the nature of superconductivity. Superconductors with anomalous properties, which are different from conventional superconductors, are always interesting to study and challenging to understand. Multigap superconductivity is an example of this kind. In multigap superconductors, energy gaps of different magnitudes exist on different, disconnected parts of the Fermi surface, giving rise to non-BCS observations of various physical properties. Following the report of high T_c superconductivity in MgB_2 and subsequent discovery of its multigap nature, there has been increased interest in investigating metal borides with similar structures. MgB_2 has a layered crystal structure that is composed of flat graphite-like sheets of boron atoms separated by hexagonal close packing layers of transition metal atoms. These sheets of Boron atoms are considered to be crucial in giving MgB_2 its novel properties.

This thesis presents our investigations on the superconducting properties of polycrystalline samples of TB_2 (T = Ru, Os) and $RRuB_2$ (R = Y, Lu). These materials have several ingredients which make them a candidate for novel superconductivity. The transition metal elements provide the possibilities of multiple orbitals, which can make up a Fermi surface with many sheets. The light mass of Boron could provide for a high T_c. Additionally, these materials have layered or quasi-low-dimensional structure motifs. OsB_2, which crystallizes in an orthorhombic structure (*Pmmn*) containing deformed Boron sheets instead of a flat Boron array as in MgB_2, has previously been reported to exhibit multigap superconductivity and RuB_2 is isoelectronic and isostructural to OsB_2. (Y, Lu)RuB_2 compounds crystallize in an orthorhombic structure (space group *Pnma*), having a zigzag chain of rare-earth atoms, with dimerized Boron and have been reported to exhibit a relatively large value of superconducting temperature. Magnetization, resistivity, and heat capacity measurements were performed on the polycrystalline samples of RuB_2. The temperature dependence of heat capacity in the superconducting state, a reduced heat capacity anomaly at superconducting transition, and the value of Ginzberg-Landau parameters indicate that RuB_2 is a rare two gap type-I superconductor. Theoretical calculations of band structure and the Fermi surface for RuB_2 also support the possibility of multigap superconductivity. Various measurements on $RRuB_2$ (R = Y, Lu)

and estimation of the various superconducting parameter has been carried out. The magnetic field-temperature (H-T) phase diagram shows an anomalous linear trend, pointing to possible unconventional superconductivity. In $LuRuB_2$, the Δ(T) dependence which deviates from BCS predictions and the small Δ/k_BT_c value also suggest unconventional superconductivity, supporting conclusions from the H-T phase diagram. On the other hand, T_c of both OsB_2 and $LuRuB_2$ reduces with the application of pressure, supporting an electron-phonon mediated superconductivity in both these families of compounds.

List of publications:

First author papers:

1. *Possible multigap type-I superconductivity in the layered boride RuB_2.*
   Jaskaran Singh, Anooja Jayaraj, D. Srivastava, S. Gayen, A. Thamizhavel, and Yogesh Singh
   PHYSICAL REVIEW B 97, 054506 (2018).

2. *Unconventional temperature dependence of upper critical field H_{c2} in the rare-earth ternary boride superconductors $RRuB_2$ (R = Lu, Y).*
   Jaskaran Singh, A. Jayraj, M. Aslam, Y. Singh et al
   Manuscript Under Preparation

3. *Evidence of time reversal symmetry breaking in layered boride RuB_2.*
   Jaskaran Singh, R. Gupta, Y. Singh et al
   Manuscript Under Preparation

Contributed papers:

4. *Spectroscopic signature of two superconducting gaps and their unusual field dependence in RuB_2*
   Soumya Datta, Aastha Vasdev, Soumyadip Halder, **Jaskaran Singh**, Yogesh Singh and Goutam Sheet
   Journal of Physics: Condensed Matter, Volume 32, Number 31 (2020).

5. *Doping-induced metal to insulator transition and the thermal transport properties in germanium.*
   Anzar Ali, **Jaskaran Singh** and RK Gopal.
   AIP Conference Proceedings 2115, 030453 (2019).

Contents

List of Figures

List of Tables

CHAPTER 1

Introduction

1.1 Introduction

In 1911, just three years after the successful liquefaction of Helium, H. Kamerlingh Onnes and his assistant Gilles Holst discovered the phenomenon of superconductivity when they observed a sharp drop in resistance of pure Mercury at 4.2 K [2]. Since then, this phenomenon has attracted a lot of attention from both experimentalists and theorists due to its promising potential for applications in real-life scenarios. W. Meissner and R. Ochsenfeld found in 1933 that when a metal becomes a superconductor, it completely expels a weak magnetic field from its interior [3]. It means that a superconductor is more than just a perfect conductor; they also show perfect diamagnetism. The exclusion of magnetic fields was discovered to be a non-classical occurrence since it could not be described using Maxwell's equations. In 1934, Gorter and Casimir proposed a phenomenological two-fluid model of superconductivity, which can explain superconductors' thermal and acoustic properties [4]. In 1935, the London brothers published two equations that provided a phenomenological explanation for perfect diamagnetism in superconductors and provided a characteristic length scale called London penetration depth [5]. In 1937, L. V. Shubnikov and coworkers reported the mixed state, also known as the Shubnikov phase, in which a magnetic field can penetrate into a superconductor in the form of flux tubes [6]. Ginzburg and L. Landau provided a phenomenological theory of superconductivity in 1950, which can explain the behavior of superconductors in strong magnetic fields [7], and A. Abrikosov theoretically explained the Shubnikov phase using this theory [8]. Already in 1950, Frohlich and, independently, Bardeen had proposed that superconductivity is caused by vibrating atoms in the material and suggested an isotope effect, which was proven experimentally by E. Maxwell and C. A. Reynolds in the same year [9, 10, 11]. In 1957, Bardeen, Cooper, and Schrieffer presented the first successful microscopic theory of superconductivity, establishing that it is a quantum phenomenon that occurs on a macroscopic scale [12]. The BCS theory provides a satisfactory picture for so-called conventional superconductors where superconducting phase transition is governed entirely by the opening of an isotropic superconducting energy gap around the Fermi surface.

Many new superconductors were discovered in the 1970s and 1980s that show unconventional superconductivity, which does not fit into the BCS picture. These include, e.g., heavy fermion and organic superconductors. In 1986, Bednorz and Muller discovered copper oxide-based high-temperature superconductors (HTS), having quasi-two-dimensional layered structures [13]. Although many models are proposed to explain unconventional behaviors in these superconductors [14, 15, 16], the question regarding the basic microscopic mechanism of superconductivity still remains very challenging to date. In the year 2001, the layered crystal structure compound MgB_2 was found to superconduct at 39 K [17], which is highest in non-oxide compounds and shows anomalous superconducting properties [18, 19, 20, 21]. This discovery revived the interest in non-oxide compounds, especially in Boron containing compounds with similar structures.

1.2 Basic Properties of superconducting State

The superconducting state, like any other state of matter, has its own set of fundamental features, which any superconductor will exhibit regardless of the mechanism of superconductivity or the material. The following are the basic properties of the superconducting state.

1.2.1 Absence of Resistance

A fascinating property of superconductors that led Kamerlingh Onnes [2] to the discovery of the phenomenon of superconductivity is their zero resistance to a small dc current. In a typical metal, the thermal vibrations disrupt the periodicity of the

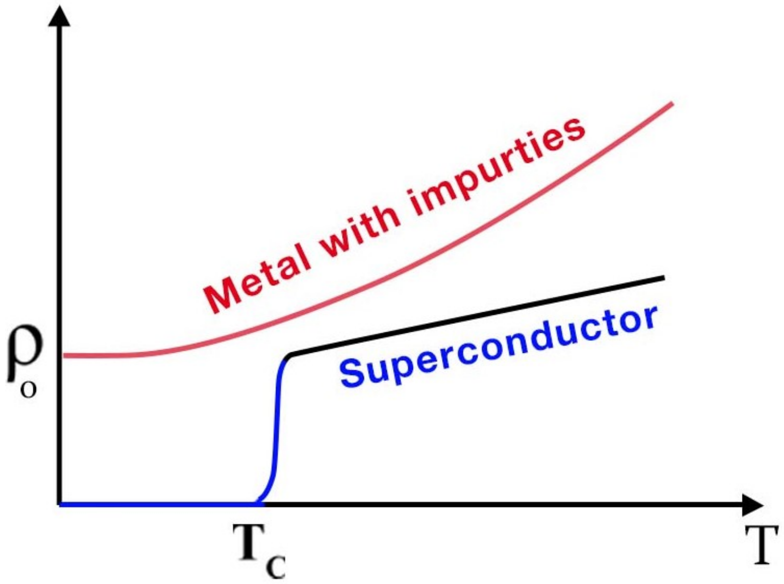

Figure 1.1: The temperature dependence of electrical resistivity in case of a metal with impurities (Red curve) and a superconductor (Blue curve). As temperature decreases, resistivity of metals decreases and then saturates to a value ρ_o near absolute zero temperature. The blue curve shows abrupt drop in resistivity to zero at T_c signaling the transition to a superconducting phase.

lattice and produce phonons, which cause the conduction electrons to scatter. This is the dominating scattering process at high temperatures (e.g., 300 K). Impurities or lattice defects also cause the scattering of conduction electrons, which are more dominant at low temperatures. Lowering the temperature reduces the thermal vibrations of atoms. As a result, a metal's resistivity decreases as the temperature drops. At absolute zero, the resistivity is mainly due to impurities and lattice defects which gives a residual resistivity ρ_o (Fig. 1.1). If the metal is pure and free of lattice imperfections, we can expect zero resistivity at absolute zero temperature. For superconductors, the situation is different; resistivity abruptly falls to zero as it is cooled below a certain temperature called the critical temperature T_c (Fig. 1.1). The critical temperature T_c is characteristic of the material. Above T_c, the material is said to be in the normal state, and below T_c, it is in the superconducting state. In the presence of impurities, the transition from the normal to the superconducting state at T_c may get broadened. The sharpness of transition is, therefore, a measure of the quality or purity of the sample.

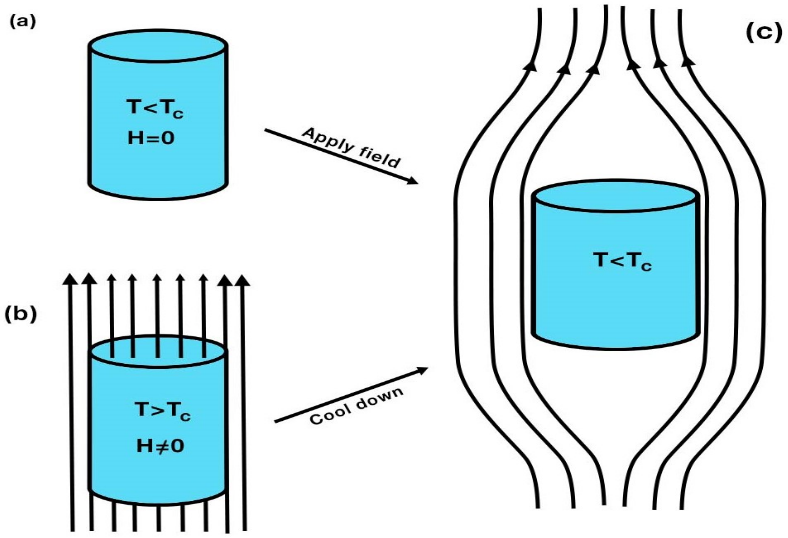

Figure 1.2: The expulsion of a weak magnetic field from the bulk of material below superconducting transition temperature T_c. (a) The material is cooled below T_c in zero field (ZFC), then the field is applied, which is excluded from the superconductor. (b) The material is cooled below T_c in the presence of field (FC), showing expulsion of the field in the superconducting state.

1.2.2 Perfect Diamagnetism

In 1933, Meissner and Ochsenfeld [3] discovered that a superconducting material always expels weak magnetic field lines from its bulk (Fig. 1.2), implying that $\mathbf{B} = 0$ inside the superconductor. This phenomenon is called the Meissner effect. In a magnetic field, screening currents are formed and flow through the superconductor's surface, canceling the flux density in its interior. This current produces a magnetization $\mathbf{M} = -\mathbf{H}$ (perfect diamagnetism) in the superconductor's interior. Perfect diamagnetism in superconductors has two main aspects, as illustrated in Fig. 1.2. The first is, if the material is zero-field-cooled (ZFC) that is cooled below Tc in the absence of a magnetic field and then is exposed to a magnetic field, the field will be excluded from the superconductor (Fig. 1.2a). The second is that if the same material in the normal state is first placed in a magnetic field, the field will penetrate the material. If this material is then field-cooled (FC), that is, cooled below Tc in the presence of this field, the field will still be expelled from the material (Fig. 1.2b). The magnetic field decays to zero over an extremely thin surface layer with a thickness of the order of λ_L (discussed in section 1.3).

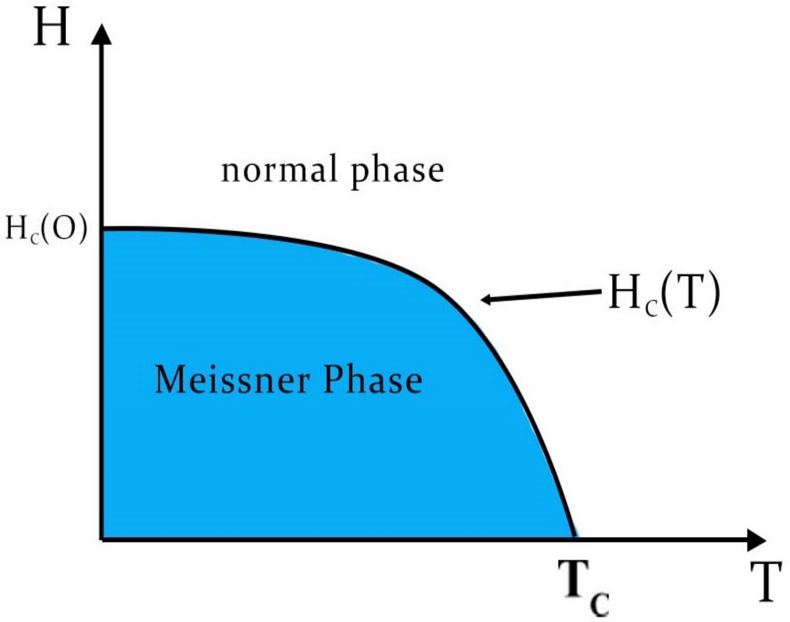

Figure 1.3: The variation of critical field with temperature T. The Curve $H_c(T)$ separates the superconducting phase from the normal phase.

1.2.3 Critical field

Each superconductor has a critical magnetic field H_c beyond which the superconducting state is destroyed, and the material returns to the normal state. The variation of thermodynamic critical field H_c with temperature is approximately given by the following phenomenological expression:

$$H_c(T) \simeq H_c(0)\left[1-(T/T_c)^2\right], \tag{1.1}$$

where $H_c(0)$ represents the critical field value at zero temperature. This temperature dependence of critical field is shown in Fig. 1.3; the curve $H_c(T)$ separates the superconducting phase from the normal phase. The applied magnetic field raises the superconductor's free energy by an amount given by

$$f_\mathrm{n} - f_\mathrm{s} = \frac{\mathrm{H}_c^2}{8\pi}, \tag{1.2}$$

where f_n and f_s are the free energy densities in the normal and superconducting state, respectively, at zero fields. Because the normal state free energy is approximately independent of the applied magnetic field, the superconductor's free energy density is reduced by amount $\frac{\mathrm{H}_c^2}{8\pi}$. This difference is called the condensation energy of the superconducting state at absolute zero temperature.

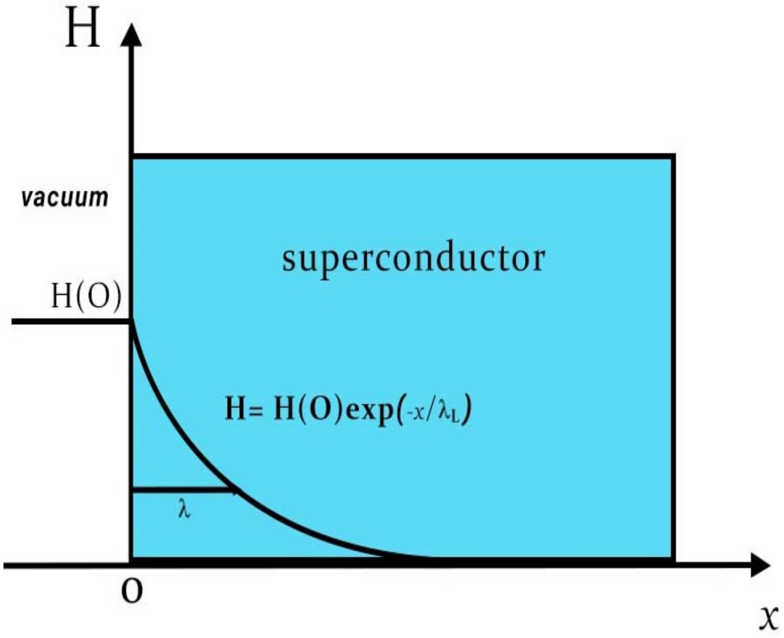

Figure 1.4: The magnetic field penetration into a superconducting material. Outside the material magnetic field is $H(0)$ and inside falls exponentially with characteristic length λ_L.

1.3 London Equations

In 1935, the London brothers [5, 22], proposed two equations to explain perfect conductivity and perfect diamagnetism seen in superconductors. These equations are:

$$\frac{\partial \boldsymbol{j}_s}{\partial t} = \frac{e^2 n_s}{m}\mathbf{E}, \tag{1.3}$$

$$\nabla \times \boldsymbol{j}_s = -\frac{e^2 n_s}{mc}\mathbf{H}. \tag{1.4}$$

Where, $\boldsymbol{j}_s$ is the current density, **E** and **H** represents electric and magnetic fields respectively, m and e denote the electronic mass and charge, n_s denotes the superfluid density, i.e., fraction of electrons participating in superconducting current. The above equations are derived in the domain of the two-fluid model of superconductivity [22, 23]. In this model, the total number density n of free electrons is assumed to be made up of superconducting electrons and normal electrons, with number densities n_s and n_n, respectively. As the temperature rises from 0 to T$_c$, the n_s value falls from n to 0 and n_n from 0 to n.

The first equation describes a situation of perfect conductivity through the free acceleration of an electric charge [22]. The second equation, when combined with

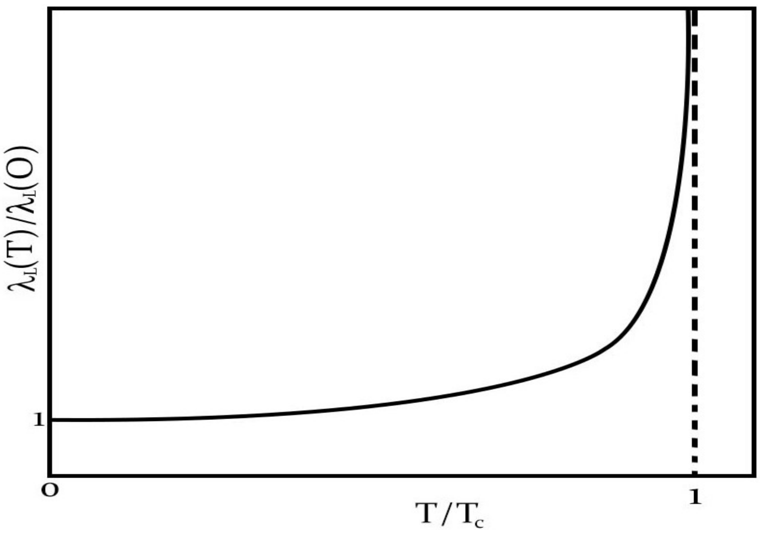

Figure 1.5: The variation of penetration depth λ_L with temperature T. At T= T$_c$, λ_L diverges.

Ampere's law, gives

$$\nabla^2 \mathbf{H} = \frac{1}{\lambda_L^2} \mathbf{H}, \tag{1.5}$$

where λ_L is called London penetration depth, which determines the length scale of magnetic field penetration in a superconductor and is given by

$$\lambda_L = \sqrt{\frac{mc^2}{4\pi e^2 n_s}}. \tag{1.6}$$

The penetration depth of most elemental superconductors is typically in the range of 10-2000 nm. In one dimension, the solution of Eq. (1.5) is

$$H(x) = H(0) \exp\left(-x/\lambda_L\right). \tag{1.7}$$

This shows that the magnetic field inside the superconductor diminishes exponentially (Fig. 1.4), giving zero fields inside the bulk, resulting in the Meissner effect.

As n_s depends upon the temperature so does λ_L. The temperature dependence of penetration depth is given by following empirical relation:

$$\lambda_L(T) = \lambda_L(0) \left[1 - (T/T_c)^4\right]^{-1/2}. \tag{1.8}$$

As shown in Fig. 1.5, at the transition temperature T$_c$, λ_L diverges, resulting in complete penetration of magnetic field inside the material.

1.3.1 Pippard's Coherence Length

The electrodynamics of superconductors discussed above was based on local electrodynamics. It means that in Eq. (1.4), current at any position is determined by the magnetic field at that position. However, this is only true if the current carriers are significantly smaller than the length scale over which the magnetic field varies, i.e., smaller than the penetration depth λ_L. Otherwise, local London electrodynamics is not appropriate. Pippard [24] developed the nonlocal generalization of the London equations and established the second fundamental length scale in a superconductor. He argued that the wave function of a superconducting state should have a characteristic dimension ξ_0 over which superconducting properties such as superfluid density varies. Only electrons possessing energy within $k_B T_c$ of the Fermi energy play a role in superconductivity. These electrons participating in superconducting current have a momentum range of $\Delta p \approx \frac{k_B T_c}{v_F}$, where v_F is the Fermi velocity and k_B denotes the Boltzmann constant. Using uncertainty principle, ξ_0 can be estimated to be

$$\xi_0 = \alpha \frac{\hbar v_F}{k_B T_c}, \tag{1.9}$$

here, α is a numeric constant; with a value of 0.18 predicted by BCS theory. ξ_0 is called the coherence length of the pure superconductor. In BCS theory, ξ_0 is physically related to the size of the Cooper pairs. $\lambda_L << \xi_0$, is the case of nonlocal electrodynamics. As temperature increases and approaches T$_c$, λ_L diverges at T$_c$ whereas ξ_0 is independent of temperature. So near T$_c$, all superconductors behave in the Local electrodynamics regime, so they can be described by the London equations.

Another important factor is the mean free path 'l' of the electron. In metals containing impurities and imperfections, the mean free path reduces due to increased scattering. So in an impure metal, effective coherence length ξ is given by $\frac{1}{\xi} = \frac{1}{l} + \frac{1}{\xi_0}$ [25, 22]. For disordered systems, where $l << \xi_0$, the superconductor is said to be in the "dirty limit," and its opposite limit is referred to as the "clean limit." In the clean limit, i.e., for pure metals, it gives $\xi \approx \xi_0$. In the next section, we'll see that the Ginzburg Landau (GL) theory of superconductivity also introduced the concept of a coherence length.

1.4 Ginzberg-Landau Theory of Superconductivity

In this section, we'll look at Ginzburg and Landau's (GL) [7, 26] phenomenological approach to the superconducting phase transition. Many natural processes, such as the boiling of liquid and magnetic transitions, can be considered as a transition from an ordered to a disordered state. Each of these transitions has an order parameter which is zero in the disordered state and non zero in the ordered state. GL theory starts with some assumptions that are later validated by the fact that they accurately describe numerous properties of the superconducting state of the material. In this theory, the superconducting state is described by a complex order parameter $\Psi(\mathbf{r})$, which is nonzero in the superconducting state and disappears in the normal state. The order parameter can be written as $\Psi(\mathbf{r}) = |\Psi(\mathbf{r})|\mathrm{e}^{i\theta}$, where θ is the phase of order parameter and the square of the modulus of order parameter, $|\Psi(\mathbf{r})|^2$, gives the superfluid density. The Ginzburg-Landau theory's basic assumption is that, close to the transition temperature below T_c, where $\Psi(\mathbf{r})$ is small and changes slowly in space, free-energy density f_s in superconducting state can be expanded as series in $|\Psi(\mathbf{r})|^2$ [22],

$$f_s = f_n + \alpha|\Psi|^2 + \frac{\beta}{2}|\Psi|^4 + \frac{1}{2m^*}\left|\left(-i\hbar\nabla - \frac{e^*}{c}\mathbf{A}\right)\Psi\right|^2 + \frac{\mathbf{h}^2}{8\pi}, \tag{1.10}$$

where, f_n is the normal state free energy; e^* and m^* are the effective charge and effective mass of the Cooper pairs; respectively, α and β are temperature-dependent phenomenological coefficients that depend upon the material.

Minimization of the free energy with respect to Ψ and $\mathbf{A}$ gives the order parameter $\Psi(\mathbf{r})$. From this minimization, the Ginzburg-Landau equations are given as:

$$\frac{1}{2m^*}\left(\frac{\hbar}{i}\nabla - \frac{e^*}{c}A\right)^2\Psi + \beta|\Psi|^2\Psi = -\alpha(T)\Psi, \tag{1.11}$$

and corresponding equation of current is,

$$\boldsymbol{j}_s = \frac{e^*\hbar}{i2m^*}\left(\Psi^*\nabla\Psi - \Psi\nabla\Psi^*\right) - \frac{e^{*2}}{m^*C}|\Psi|^2\boldsymbol{A}. \tag{1.12}$$

With $\Psi = |\Psi|e^{i\theta}$ and using Eq. (1.11), velocity of a super electron can be written as:

$$\boldsymbol{v}_s = \frac{\hbar}{2m^*}\left(\nabla\theta - \frac{2e^*}{\hbar c}\boldsymbol{A}\right). \tag{1.13}$$

Eqs. (1.11) and (1.12) are two coupled differential equations that may be solved to determine superconducting state parameters. The equations can be solved numerically in most cases. However, in some simple cases, closed-form solutions can be found, and in others, approximate solutions are obtained. In simple cases, GL equations can be converted to a normalized form, and solutions for other cases can be obtained. Many superconducting parameters emerge as a consequence when these equations are expressed in a normalized form.

If we consider a case of zero field inside a superconductor and with homogeneous boundary conditions i.e $\nabla^2\Psi = 0$, Eq. (1.10) becomes:

$$f_s = f_n + \alpha|\Psi|^2 + \frac{\beta}{2}|\Psi|^4; \tag{1.14}$$

The minimization of above equation with $|\Psi(\mathbf{r})|^2$ inside a superconductor gives

$$|\Psi|^2 = -\frac{\alpha}{\beta}. \tag{1.15}$$

Using this in Eq. (1.14), we get

$$f_n - f_s = \frac{\alpha^2}{2\beta}. \tag{1.16}$$

As free energy in the superconducting state is lower than the normal state, so above equation implies that β must be positive. At T = T$_c$, Ψ must be zero , and below T$_c$ it is finite. Then it follows from Eq. (1.15) that α = 0 at T = T$_c$, and is negative for T < T$_c$. As a result, in a first approximation (in the vicinity of T$_c$);

$$\alpha \propto (T - T_c)\,. \tag{1.17}$$

Eq. (1.16) can be written as

$$\begin{aligned} f_\mathrm{s} &= f_\mathrm{n} - \frac{1}{2}\left(\frac{\alpha^2}{\beta}\right) \\ &= f_\mathrm{n} - \frac{1}{2}(\alpha_0)\left[1 - \frac{T}{T_\mathrm{c}}\right]^2, \end{aligned}$$

where α_0 is some constant. The quantity $\frac{1}{2}\left(\frac{\alpha^2}{\beta}\right)$ represents the energy released by the transition of normal electrons to the super electron and is called condensation energy per unit volume of superconducting electrons. From Eq. (1.2), this is related to the thermodynamical critical field H_c, as:

$$\frac{1}{2}\left(\frac{\alpha^2}{\beta}\right) = \frac{H_c^2}{8\pi}. \tag{1.18}$$

Flux quantization is another crucial characteristic that emerges from the GL theory. The phase coherence and a single-valued requirement of the wave function are proven to generate quantized magnetic flux in a small superconducting ring. The quantum of flux is denoted by Φ_0 and is equal to $hc/2e$ [27].

1.4.1 Two Fundamental Length Scales

G-L equations, when solved in case of inhomogeneous boundary conditions e.g., at the superconducting-insulating interface, introduces two characteristic length scales [22]:

$$\xi_{GL}^2 = \frac{\hbar^2}{4m^*|\alpha|}, \tag{1.19}$$

and

$$\lambda^2 = \frac{m^* c^2 \beta}{8\pi e^{*2}|\alpha|}. \tag{1.20}$$

Where ξ_{GL} is called the coherence length, and it differs from the Pippard coherence length fundamentally. Physically, ξ_{GL} is the length scale measured from the superconductor's surface across which the order parameter varies significantly. For most of the elemental superconductors, ξ_{GL} values are in the range of 10 to 100 nm. The second fundamental length scale λ, which arises when one investigates the behavior of applied magnetic field in the vicinity of boundary, is called penetration depth and is the same as London penetration depth defined in section 1.3. So, London equations can also be obtained from GL theory. Using Eq. (1.17), it can be seen that in the vicinity of T_c, the temperature dependence of ξ_{GL} and λ are similar. Therefore, their ratio is unaffected by temperature. Combining Eqs. (1.18), (1.19), and (1.20) one gets an important relation:

$$\xi_{GL}(T) = \frac{\Phi_0}{2\sqrt{2}\pi H_c(T)\lambda_L(T)}. \tag{1.21}$$

The GL theory shows that near Tc, ξ_{GL} evolves differently in the clean and dirty limit as follow [22]:

In clean limit

$$\xi_{GL}(T) = 0.74 \frac{\xi_0}{(1 - T/T_c)^{1/2}},$$

and in dirty limit

$$\xi_{GL}(T) = 0.855 \frac{(\xi_0 l)^{1/2}}{(1 - T/T_c)^{1/2}}.$$

1.4.2 Type-I and Type-II Superconductors

Superconductors are divided into two categories based on their response to an external magnetic field. If we consider a very thin superconducting slab (thickness< λ_L), the magnetic field at the core does not drop to zero. As a result, the amount of energy that must be expelled in going from normal to superconducting state is reduced, implying that a very thin sheet's critical field is considerably larger than that of a thick slab. Therefore, it seems energetically favorable for a thick slab to partition itself into an alternating sequence of thin normal and superconducting segments. Although the magnetic energy is reduced in this manner, there is another energy to consider: the energy required to create the normal-superconductor interfaces. Such subdivisions are possible only if the magnetic energy is more than the interface energy. The interface energy approximately is given by:

$$\sigma_{\mathrm{ns}} \approx \frac{H_{\mathrm{c}}^2}{8\pi} \left(\xi_{GL} - \lambda_{\mathrm{L}}\right). \tag{1.22}$$

At a normal-superconductor interface, the number density of supercurrent carriers does not rise abruptly from zero to its value in the core of the superconductor but rises gradually over a distance ξ_{GL}. Magnetic field, on the other hand, enters a surface layer with a width of λ_{L}, and full expulsion happens only in the core of the superconductor. The first term in Eq. (1.22) represents free energy acquired by condensation into the superconducting state, whereas the second term represents the cost of rejecting flux from the boundary layer.

The variation of order parameter and a magnetic field near the metal-superconductor interface for the type-I and type-II superconductors are shown in Fig. 1.6. Whether a material is of type I or type II superconductor is determined by the relative size of the coherence length and London penetration depth. The Ginzburg-Landau theory gives a more refined treatment and introduces the Ginzburg-Landau parameter

$$\kappa = \lambda_L / \xi_{GL}. \tag{1.23}$$

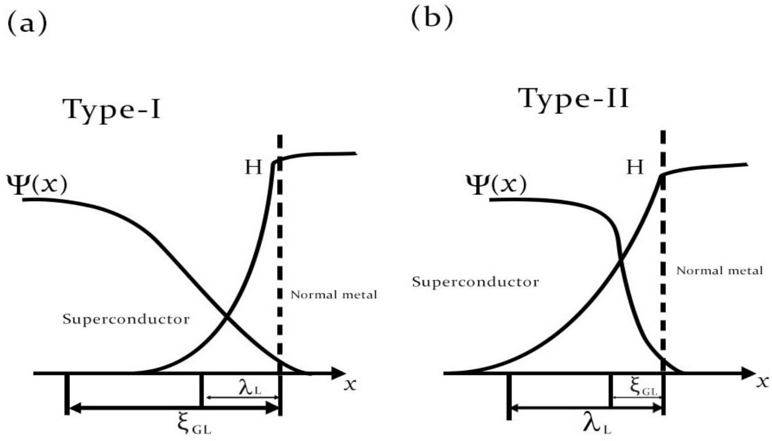

Figure 1.6: Variation of the order parameter $\Psi(x)$ and magnetic field H at metal-superconductor boundary. (a) for type-I superconductor ($\kappa < 1/\sqrt{2}$) and (b) for type-II superconductor ($\kappa > 1/\sqrt{2}$)

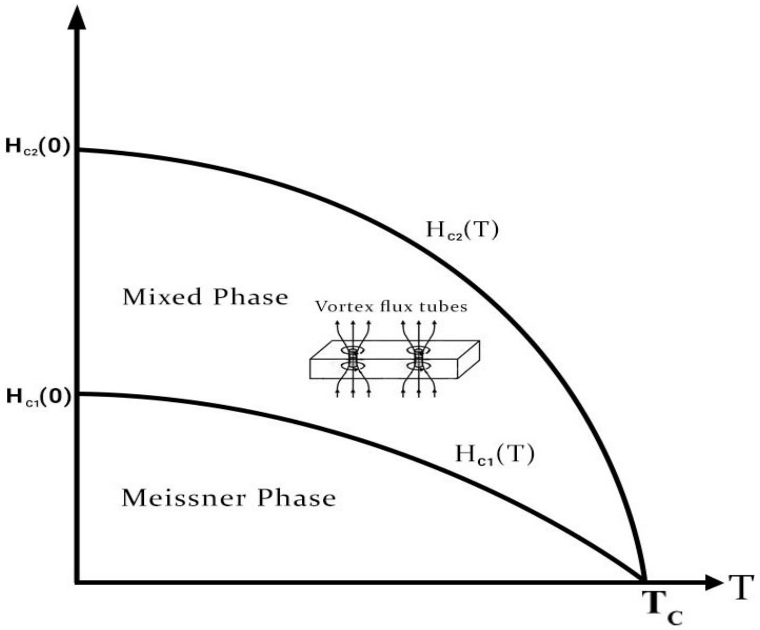

Figure 1.7: Phase diagram for a typical type II superconductor. Below $H_{c1}(T)$, material exists in Meissner state in which it shows complete expulsion of magnetic field, between $H_{c1}(T)$ and $H_{c2}(T)$ it shows mixed state in which magnetic field can penetrate the material in the form of flux tubes and above $H_{c2}(T)$ it is in the normal phase.

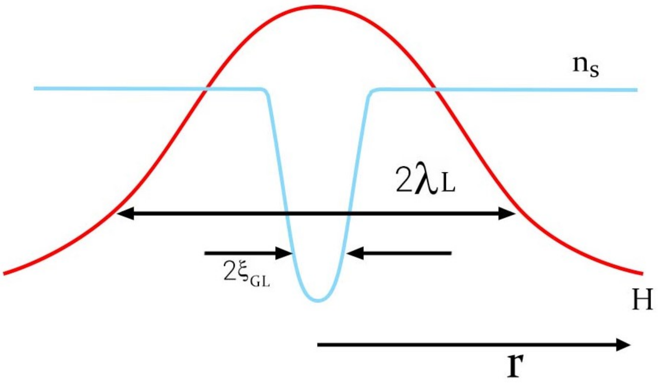

Figure 1.8: Spatial Variation of magnetic field H, and super current density n$_s$ around the vortex center. At the vortex center n$_s$ is zero and has maximum value at a distance ξ_{GL} from the vortex center.

In 1957, Abrikosov [8] showed that $\sigma_{\mathrm{ns}} = 0$ for $\kappa = 1/\sqrt{2}$. The criteria for superconductivity of type-I or type-II is determined as

$$\text{type I: } \kappa < 1/\sqrt{2},$$
$$\text{type II: } \kappa > 1/\sqrt{2}.$$

We have already seen the phase diagram of type-I superconductors (Fig. 1.3). At all fields below a critical field H$_c$, type-I superconductors exhibit perfect diamagnetism, and above H$_c$, superconductivity is completely lost. Type-I superconductors make up the majority of elemental superconductors. Abrikosov established that for $\kappa > 1/\sqrt{2}$ (type-II), σ_{ns} is negative, which results in an equilibrium state in which the field lines can enter the superconductor in the form of flux tubes called vortex that forms a triangle pattern [28, 29]. Figure 1.7 shows the phase diagram for type-II superconductors. Two critical fields, H$_{c1}$ and H$_{c2}$, characterize Type II superconductors, both of which are temperature-dependent. Below H$_{c1}$, the material is perfect diamagnetic. Vortices emerge above the lower critical field H$_{c1}$, and flux penetration continues to increase until the higher critical field H$_{c2}$ where vortex cores almost overlap, at which point superconductivity is destroyed completely. The phase between H$_{c1}$ and H$_{c2}$ is called the mixed-phase or Shubnikov phase [6]. We can say that λ_L is the vortex's width, i.e., it defines the radius containing the magnetic flux. The super electron density n_s is zero at the vortex's center, and ξ_{GL} is the distance across which n_s reaches its maximum value (Fig. 1.8). A large coherence length hinders n_s from rising quickly and can provide the shielding current required to restrict the flux, preventing the formation of a vortex. The magnetiza-

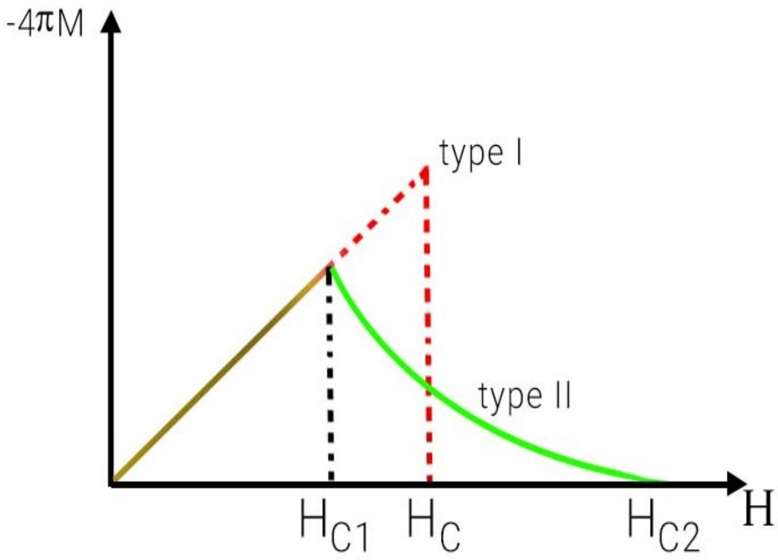

Figure 1.9: Magnetization M as a function of magnetic field H for type-I (Red line) and type-II (Green line) superconductors.

tion M as a function of magnetic field H for type-I and type-II superconductors are shown in Figure(Fig. 1.9). The area under the M-H curve is the same as for a type-I superconductor as it represents the difference in free energy between normal and superconducting states. In the mixed-phase, a type II material has a lower magnetic moment than a type-I material.

The mean free path of conduction electrons in alloys and compounds is considerably shorter than in pure metals. As a result, type-II superconductivity is common in alloys and compounds. The upper critical field in the framework of Ginzburg-Landau theory is given by [22]:

$$\mathrm{H_{c2}} = \sqrt{2}\kappa \mathrm{H_c}. \tag{1.24}$$

Using Eqs. (1.21) and (1.23), one obtains

$$\mathrm{H_{c2}} = \sqrt{2}\kappa \mathrm{H_c} = \frac{\Phi_0}{2\pi\xi_{GL}^2}. \tag{1.25}$$

The lower critical field in the limit $\kappa >> 1$, is given by

$$\mathrm{H_{c1}} \simeq \mathrm{H_c}\frac{\ln k}{\sqrt{2}k}. \tag{1.26}$$

1.5 BCS Picture of Superconductivity

In 1956, Cooper showed that when two electrons with an attractive potential are added to a filled Fermi sphere, they can bound to form a pair. This bound state is called the Cooper pair [30]. Only Cooper pairs with net momentum zero (K = k1 + k2 = 0) are likely to form, which means electrons have equal and opposite momentum and also opposing spin in pairs. Following this idea, Bardeen, Cooper, and Schrieffer (BCS) in 1957 gave the first successful microscopic theory of superconductivity [12, 31]. The basic idea of the theory is that at sufficiently low temperature, electrons near the Fermi surface become unstable against the formation of Cooper pairs, and it is electron-lattice interaction, no matter how weak, which is responsible for creating an attractive potential resulting in the binding of two electrons. Gor'kov showed that Ginzburg-Landau's theory can be developed from the BCS theory [32]. In the language of second quantization, the BCS pairing Hamiltonian is written as:

$$H = \sum_{\mathrm{k}\sigma} \varepsilon_{\mathrm{k}} n_{\mathrm{k}\sigma} + \sum_{\mathrm{kk}'} V_{\mathrm{kk}'} c^*_{\mathrm{k}\uparrow} c^*_{-\mathrm{k}\downarrow} c_{-k'\downarrow} c_{\mathrm{k}'\uparrow}. \tag{1.27}$$

The first term in the Eq. (1.27) describes the kinetic part of the non-interacting electron gas, whereas the second term represents the pairing interaction, in which electrons scatter from state k' to state k via exchange of phonon. $c_{-k'\downarrow} c_{\mathrm{k}'\uparrow}$ represents annihilation of pair and $c^*_{\mathrm{k}\uparrow} c^*_{-\mathrm{k}\downarrow}$ represents the creation of pair with equal and opposite momenta and spin. V$_{kl}$ is a scattering matrix element, and BCS theory replaces it with an effective constant potential -|V|. This pairing interaction can crudely be seen to arise as follows. An electron creates lattice distortion as it attracts the positive ions. The second moving electron will experience this distortion. As a result, a weak indirect attractive interaction between these electrons may emerge.

Only a small fraction of electrons participate in the electron-lattice interaction to form cooper pairs, particularly those in a shell of thickness $\hbar\omega_D$ (ω_D is Debye frequency) in the vicinity of the Fermi surface (Fig. 1.10). All Cooper pairs condense into the same phase-coherent macroscopic quantum state resulting in zero resistance. As a result of this pairing, an energy gap opens around the Fermi surface (Fig. 1.11). Each electron gains energy Δ and a pair gains 2Δ. Cooper pairs only exist in the BCS ground state, and excitation is equivalent to separating them into normal electrons. This gap must be overcome in order for the electrons to go into their normal state. A Cooper pair's binding energy turns out to be very low, around $10^{-4} - 10^{-3}$ eV; this means very low temperatures are required to keep the

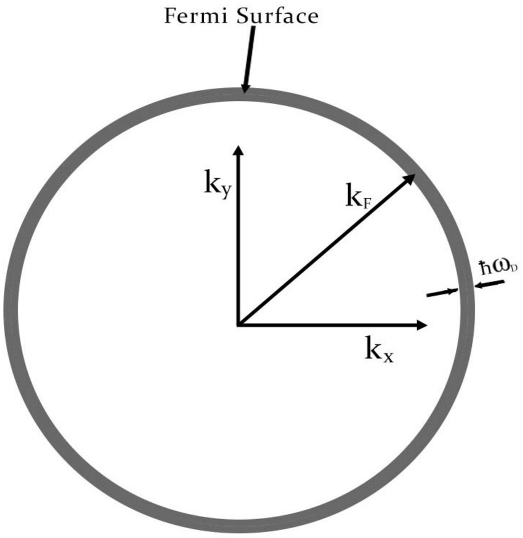

Figure 1.10: In the BCS theory, only electrons that lie within a shell of thickness $\hbar\omega_D$ near the Fermi surface interact through phonons.

binding intact.

From BCS theory, the energy gap is given by the relation

$$\Delta(0) = 2\hbar\omega_D \exp\left(-\frac{1}{VN(\varepsilon_F)}\right), \tag{1.28}$$

where, V is the effective electron-lattice interaction potential and $N(\varepsilon_F)$ represents density of states at Fermi level. $\Delta(0)$ is the energy gap at absolute zero temperature.

Bogoliubov-Valatin [33, 34] canonical transformation of the BCS Hamiltonian and mean-field approximations gives a self-consistent approach to deal with excited states at finite temperature. In superconductors, the elementary excitations are electron and hole-like quasi particles that result from the Cooper pairs breaking. Energy of these quasi particles is determined as:

$$E_\mathrm{k} = \sqrt{\varepsilon_\mathrm{k}^2 + \Delta^2}, \tag{1.29}$$

where ε_k is the energy of single particle relative to Fermi energy. It means that there is a gap of magnitude Δ in the energy spectrum. The dependence of gap on temperature can be found numerically using:

$$\frac{1}{N(\varepsilon_F)V} = \int_0^{\hbar\omega_D} \frac{\tanh\frac{1}{2}\beta\left(\varepsilon^2+\Delta^2\right)^{\frac{1}{2}}}{(\varepsilon^2+\Delta^2)^{\frac{1}{2}}} d\varepsilon, \tag{1.30}$$

where ε is the single-particle energy relative to the Fermi energy and $\beta = 1/k_\mathrm{B}T$.

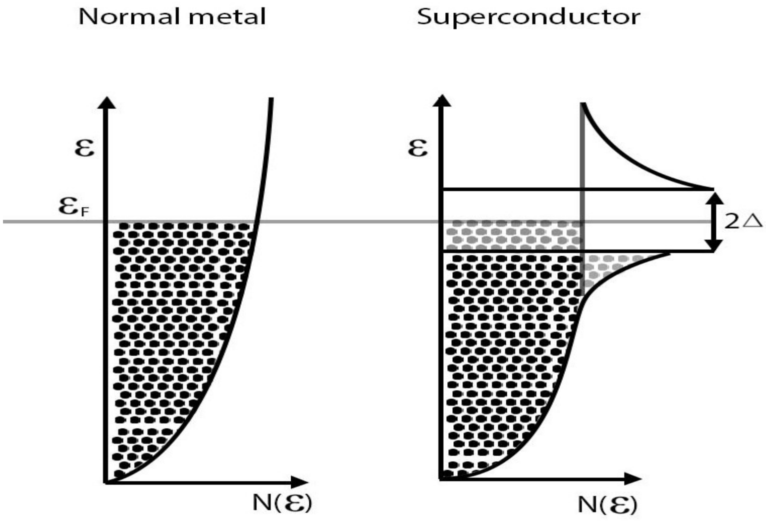

Figure 1.11: The density of states of a superconductor is compared to that of a normal metal. In case of superconductor, an energy gap of magnitude 2Δ opens up in the density of states around the Fermi level.

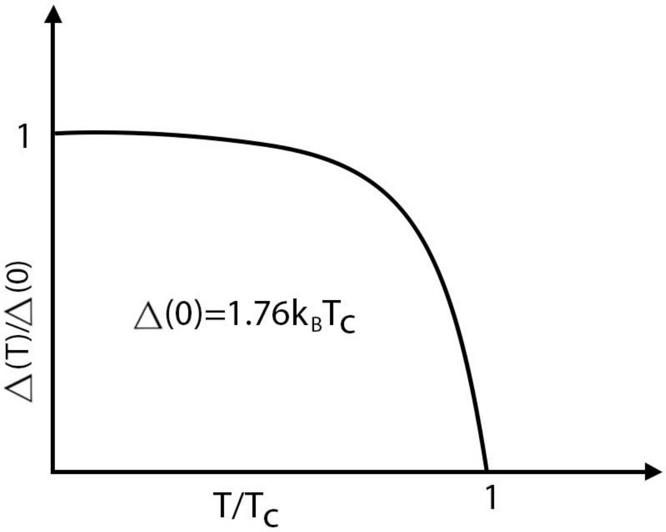

Figure 1.12: Variation of the normelized superconducting gap with temperature. At T=0 K, gap has maximum value and becomes zero at transition temperature T_c.

The superconducting transition temperature (T$_c$) in BCS theory is the temperature at which the binding energy of Cooper pairs becomes zero. Taking $\Delta(T) \rightarrow 0$ at T→T$_c$ in Eq. (1.30), one can get the expression for the critical temperature T$_c$ as:

$$k_B T_c = 1.13\hbar\omega_D \exp\left(-\frac{1}{VN(\varepsilon_F)}\right). \tag{1.31}$$

Compairing Eq. (1.28) and (1.31), we get one of the most important BCS predictions;

$$\frac{\Delta(0)}{k_B T_c} = 1.76. \tag{1.32}$$

The temperature dependence of superconducting gap in weak coupling limit can be approximated as $\frac{\Delta(T)}{\Delta(0)} \approx 1.76\left(1 - \frac{T}{T_c}\right)^{1/2}$ and this dependence is shown in Fig. 1.12.

1.5.1 BCS Coherence Length

Using the uncertainty principle, one can find the size of the Cooper pair. It is characterized by the BCS coherence length $\xi_{BCS} = \hbar v_F/\pi\Delta$, where v_F is the Fermi velocity of electron. Because of the weak binding strength, the coherence length is very long. For most superconductors, ξ_{BCS} is 100-1000 nm. So a Cooper pair is an extended object, 100-1000 lattice constants long. Therefore, around a million other Cooper pairs are present in the space spanned by a Cooper pair resulting in overlap of all the pairs and creating a collective state.

1.5.2 Heat capacity

The specific heat of superconductors is one of the most investigated properties. In heat capacity measurement, the entire sample responds, in contrast to many other measurements that are only sensitive to a portion of the sample. So it represents a bulk measurement that considers the entire sample.

At temperatures much below the Debye temperature θ_D, a normal metal's heat capacity C_n is the sum of a linear component C_{el} arising from conduction electrons and a phonon term C_{ph} i.e

$$C_n = \gamma_n T + \beta T^3, \tag{1.33}$$

γ_n is called the Sommerfeld coefficient [35]. The electronic contribution to the specific heat in the free-electron approximation is given by

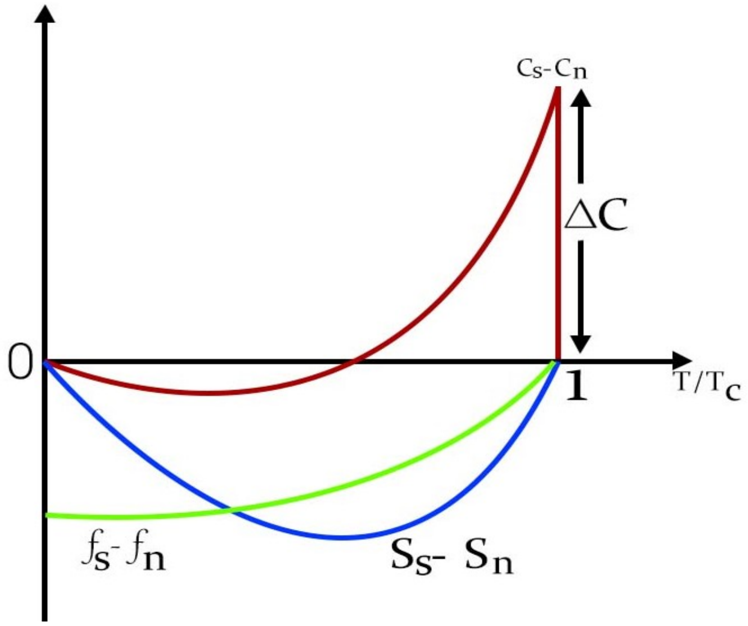

Figure 1.13: The temperature variation of difference of thermodynamic variable in superconducting state and their values in the normal state. All curves are in zero magnetic field. The symbol f represents the free energy, S represents the entropy and and C represents the electronic heat capacity.

$$\gamma_n T = \frac{\pi^2 N(\varepsilon_{\mathrm{F}}) k_{\mathrm{B}}^2}{3} T.$$

In the Debye model, the phonon contribution is given by

$$C_{\mathrm{ph}} = \beta T^3 = \left(\frac{12\pi^4 R}{5}\right)\left(\frac{T}{\theta_D}\right)^3,$$

where R represents the molar gas constant. From heat capacity C versus temerature T measurements one can easily find out Debye temperature θ_D and density of states $N(\varepsilon_{\mathrm{F}})$.

In a zero magnetic field, the transition from the normal to the superconducting phase is a second-order phase transition. In second-order phase transition, Gibbs free energy and its first-order derivatives are always continuous, whereas the second derivatives exhibit finite-step discontinuities. From the temperature dependence of difference of entropy in superconducting and normal phase ($S_{\mathrm{s}} - S_{\mathrm{n}}$), shown in Fig. 1.13, $S_{\mathrm{s}} = S_{\mathrm{n}}$ at T_c. This implies that no latent heat is involved in the transition. However, there is a jump in the specific heat. At $0 < T < T_c$, $S_{\mathrm{s}} < S_{\mathrm{n}}$, indicating that the superconducting phase is more ordered than the normal state.

The BCS theory (in the weak electron-phonon coupling limit), electronic specific

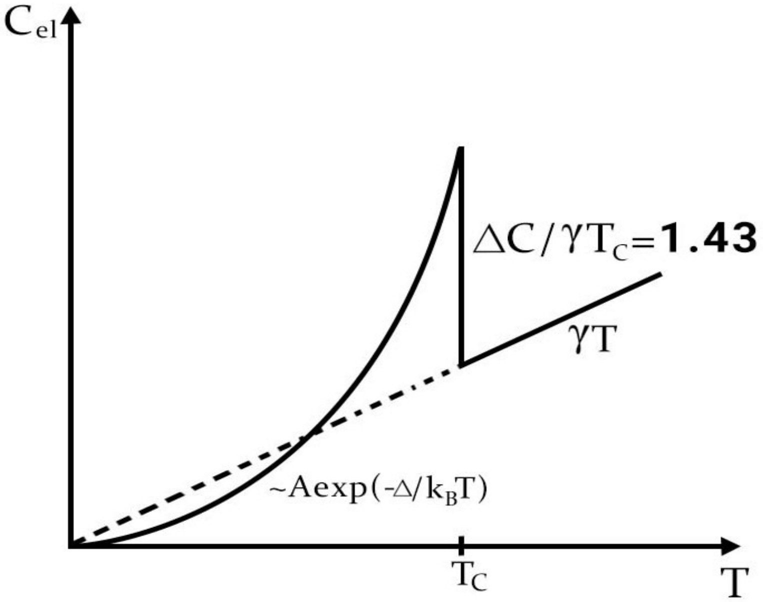

Figure 1.14: The temperature dependence of electronic heat capacity of a superconductor. At T=T_c, heat capacity shows a jump with normalized jump height of $\frac{C_s-\gamma T_c}{\gamma T_c} = 1.43$ (BCS prediction). Below T_c, heat capacity rises exponentially with temperature $\approx A\exp\left(-\frac{\Delta}{k_\mathrm{B}T}\right)$.

heat at the superconducting transition jumps abruptly from its normal-state value $\gamma_n T_c$ and the normalized jump height is:

$$\frac{\Delta C}{\gamma T_c} = \frac{C_s - \gamma T_c}{\gamma T_c} = 1.43, \tag{1.34}$$

where C_s is the electronic heat capacity in the superconducting state. In superconducting state for temperatures $T << T_c$, BCS theory predicts that electronic contribution to the specific heat will have exponential dependence on temperature (Fig. 1.14)

$$C_\mathrm{s} \approx A\exp\left(-\frac{\Delta}{k_\mathrm{B}T}\right) \tag{1.35}$$

The exponential dependence of specific heat on temperature means that in the superconducting state, electrons that condense in Cooper pairs no longer contribute to energy transfer. The value of specific-heat jump increases in the strong electron-phonon coupling limit, i.e. when $\Delta > 1.76k_BT_c$, $\Delta C/\gamma T_c > 1.43$. In an applied magnetic field, the latent heat of transition is not zero. It means that in the presence of a magnetic field, the transition from normal to superconducting phase is the first-order phase transition.

1.5.3 Isotope effect

In the BCS picture of superconductivity, electron-lattice interaction is responsible for creating attraction between electron pairs. Finding experimental confirmation for this mechanism is always of great interest. From Eq. (1.31) , $T_c \propto \omega_D$. If we model lattice vibrations as coupled harmonic oscillations, then the frequency of lattice vibrations is inversely proportional to $\sqrt{M}$, where M is the mass of lattice ion. This gives

$$T_c \propto 1/\sqrt{M}. \tag{1.36}$$

It implies that different isotopes of the same superconducting metal have different superconducting transition temperatures, and the majority of superconducting materials are experimentally found to obey the above equation [22, 23, 9]. The existence of the isotope effect shows that the vibrations of the crystal lattice play a key role in superconductivity [10].

1.5.4 Electron-phonon coupling strength

The parameter $\lambda_{\rm ep} = N(\varepsilon_F)V$ is called the electron-phonon coupling constant. The calculation of T$_c$ in section 1.5 assumed a mean-field approach, in which λ_{ep} was taken as constant, which is valid only for weak coupling limit i.e. for $\lambda_{\rm ep} = N(\varepsilon_F)V << 1$. In the weak coupling limit Coulomb interaction can be added in Eq. (1.31) as:

$$k_BT_c = 1.13\hbar\omega_D \exp\left(-\frac{1}{\lambda_{\rm ep} - \mu^*}\right) \tag{1.37}$$

where μ^* is called the coulomb pseudo-potential. However, the details of the electron-phonon interaction must be considered in strong coupling superconductors ($\lambda_{\rm ep} >> 1$). As illustrated in Eliashberg calculations [36], the electron-phonon interaction strength $\lambda_{\rm ep}$ is determined by the function $\alpha^2(\omega)F(\omega)$, where $F(\omega)$ represents the density of states of phonon spectrum, $\alpha^2(\omega)$ describes the electron-phonon interaction. McMillan [37] gives the superconducting transition temperature as:

$$T_c = \frac{\theta_D}{1.45}\exp\left[-\frac{1.04(1+\lambda_{\rm ep})}{\lambda_{\rm ep} - \mu^*(1+0.62\lambda_{\rm ep})}\right], \tag{1.38}$$

where θ_D is Debye temeprature defined as $\hbar\omega_{\rm D} = {\rm k_B}\theta_{\rm D}$. The Debye frequency appears in McMillan's Tc formula in both the pre-exponential factor and the electron-phonon coupling constant. This explains the deviation from mass isotope effect in most superconductor.

1.6 Effect of Pressure on Superconductivity

The high-pressure studies on superconductors are significant because pressure has a considerable impact on the superconducting transition temperature T$_c$ [38]. The variation in temperature primarily alters the occupancy of energy levels, whereas the variation in pressure application mainly results in modifying these energy levels. The rate of change of T$_c$ values as a function of pressure/chemical composition can be used to determine if a novel superconducting material is capable of exhibiting high Tc values or not. The greater the $\mathrm{d}T_\mathrm{c}/\mathrm{d}P$ value, the more likely the novel material will have higher T$_c$ values at ambient pressure as a result of chemical substitution. Some non-superconducting materials have also been discovered to exhibit superconductivity when subjected to high pressures [39]. The study of the dependence of superconducting properties on pressure can help in testing theoretical models and provide insight into the pairing mechanism.

In the BCS expression of critical temperature Eq. (1.31), the variations in the isotopic mass M mainly affect the prefactor ω_D, with a minor effect on exponent, whereas under the application of pressure, the exponent factor is mainly modified as pressure effectively changes both the density of states as well as the lattice vibrations. The main cause for the observed fall in T$_c$ with increasing pressure in some BCS superconductors is a significant decrease in the pairing interaction rather than a decrease in $N(\varepsilon_F)$. The argument can be further supported if we look at the McMillan's [37] expression without Coulomb potential, as change in coulomb potential with pressure is negligible. Using this, the electron-phonon coupling parameter can be expressed as

$$\lambda_{\mathrm{ep}} = \frac{N(\varepsilon_F)\left\langle I^2\right\rangle}{M\left\langle\omega^2\right\rangle}, \tag{1.39}$$

where $\left\langle I^2\right\rangle$ denotes the average square electron-phonon scattering matrix element and $\left\langle\omega^2\right\rangle$ represents mean square phonon frequency. In simple approximation $M\left\langle\omega^2\right\rangle \approx M\langle\omega\rangle^2 \approx M(k/M) = k$, where k denotes the lattice spring constant. Therefore Eq. (1.31) can be written as

$$T_c \approx \sqrt{k/M}\cdot\exp[-k/\eta], \tag{1.40}$$

where $\eta = N(\varepsilon_F)\left\langle I^2\right\rangle$ is called the Hopfield parameter and changes very gradually with pressure [40, 41]. Under pressure, the spring constant k increases significantly. As a result, a rapid decrease in T_c with increasing pressure is observed as drop in the $(-k)$ component in the exponent dominates over the increment in the prefactor $\sqrt{k}$.

In the BCS picture of superconductivity, high density of states at Fermi energy results in higher transition temperature T_c. In transition metals, the d-electron states at Fermi energy has high density of states as d-band is narrow and can accommodate up to ten electrons, favoring superconductivity at greater temperatures than basic s, p metals. In many cases, T_c rises as the Hopfield parameter rises rapidly under pressure. The multiatom systems have greater T_c values than single-atom systems because their structural flexibility allows for more optimization. The highest T_c values are seen in quasi 2D solids like MgB_2 and high-T_c cuprate oxides. These compounds, under both ambient and high-pressure conditions, exhibit a tremendous deal of structural and electrical complexity, which has hampered attempts to gain a basic understanding of the mechanisms that cause the superconductivity. The measured dT_c/dP dependence in the case of MgB_2 is compatible with BCS picture (electron-phonon coupling) [42, 43].

1.7 Unconventional superconductor

In conventional superconductors, Cooper pairs with opposite spin and momentum $(k_1 + k_2 = 0$ and $s_1 + s_2 = 0)$ are formed through electron-electron interaction mediated by phonons. Angular momentum l of each Cooper pair is zero resulting in a BCS ground state with zero angular momentum. In conventional superconductors, the gap Δ is isotropic means it has no k dependence, as illustrated in Fig. 1.10. This illustrates that no matter from which section of the Fermi surface you try to excite the electron, you must supply the same amount of energy to bridge the gap and such a superconducting ground state is commonly described as having an s-wave symmetry (just using the shape of atomic orbitals as an analogy). The order parameter ψ of a superconducting state is a complex quantity . The variations in $|\psi|$ are proportionate to variations in Δ. If $|\psi|$ or energy gap Δ is positive everywhere, then order parameter is also said to have an s-wave symmetry. If Δ is constant, it is called isotropic s-wave symmetry and if Δ varies in real space, then it is said to have anisotropic s-wave symmetry.

Unconventional characters can result from a variety of reasons.[14, 15, 16]. In most unconventional superconductors, each Cooper pair's electrons still have the opposite momentum and spin; however, the angular momentum of a Cooper pair is non-zero in most cases [44]. In the finite momentum pairing, the pair's angular momentum l can be either an even multiple of $\hbar$ (singlet pairing) or an odd multiple of $\hbar$ (triplet pairing).

When $l = 2$, it is common to refer to the superconducting ground state as having a d-wave symmetry. If we look at the Fermi surface of the filled fermi sea, the superconducting gap Δ is k dependent. In d wave- symmetry, The energy gap has two positive and two negative lobes, as well as four nodes or gapless points between the lobes. d wave pairing is accepted to exist in many high Tc superconductors [45]. The density of cooper pairs at nodal sites is zero; hence the single-particle excitation spectrum has no gaps in this direction. The angular resolved spectroscopy confirmed the presence of d wave superconductivity. Triplet pairing or p wave pairing occurs when $l = 1$.

1.8 Multigap Superconductivity

Multigap superconductors are another kind that shows anomalous superconducting behaviors. As we have discussed in the above section, in conventional superconductors collective behavior of electrons on the Fermi surface makes equal contributions to the pairing mechanism, resulting in a constant isotropic superconducting gap. If distinct superconducting gaps exist on different disconnected parts of the Fermi surface, a different situation can arise, resulting in anomalous superconducting behaviors which are different from conventional superconductors. The multi-band superconductivity was first studied theoretically by Suhl et al. [46].

In the situations in which two bands with more or fewer wandering electrons overlap, the Hamiltonian of BCS theory can be extended as

$$H = \sum_{\mathrm{k}\sigma} \varepsilon_{\mathrm{k}1} c_{\mathrm{k}\sigma}{}^{*} c_{\mathrm{k}\sigma} + \sum_{\mathrm{k}\sigma} \varepsilon_{\mathrm{k}2} d^{*}_{\mathrm{k}\sigma} d_{\mathrm{k}\sigma} - \sum_{\mathrm{kk}'} V_{11} c^{*}_{\mathrm{k}\uparrow} c^{*}_{-\mathrm{k}\downarrow} c_{-\mathrm{k}'\downarrow} c_{\mathrm{k}'\uparrow} - V_{22} \sum_{\mathrm{kk}'} d^{*}_{\mathrm{k}\uparrow} d^{*}_{-\mathrm{k}\downarrow} d_{-\mathrm{k}'\downarrow} d_{\mathrm{k}'\uparrow}$$
$$- V_{12} \sum_{\mathrm{kk}'} \left(c^{*}_{\mathrm{k}\uparrow} c^{*}_{-\mathrm{k}\downarrow} d_{-\mathrm{k}'\downarrow} d_{\mathrm{k}'\uparrow} + d^{*}_{\mathrm{k}\uparrow} d^{*}_{-\mathrm{k}\downarrow} c_{-\mathrm{k}'\downarrow} c_{\mathrm{k}'\uparrow} \right), \tag{1.41}$$

where c_{k}, c^{*}_{k} represents annihilation and creation operators of elctrons from first band and d_{k}, d^{*}_{k} represents annihilation and creation operators of elctrons from second band. V_{11} and V_{22} represents effective interaction energies resulting from

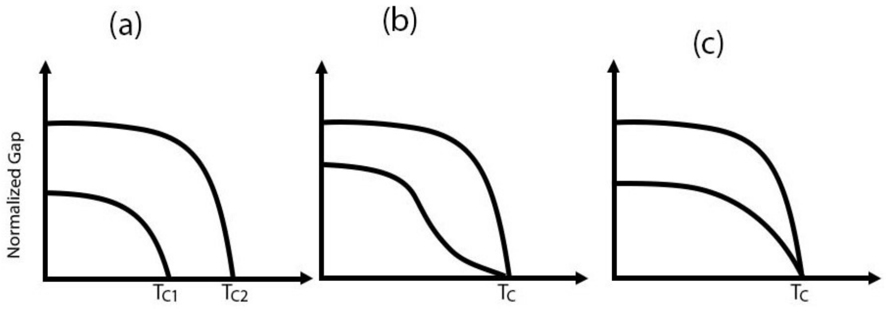

Figure 1.15: Evolution of the superconducting gaps. (a) If there is no inter band pairing, (b) If inter band pairing is weak, and (c) If there is strong inter band pairing.

electron-phonon scattering processes arising with in first band and second band respectively, whereas V_{12} represents interband scattering processes.

According to the two-band framework, when electrons on different Fermi sheets in the material have different electron-phonon-coupling strengths, distinct superconducting energy gaps can occur. The amount of interplay between the bands is determined by their relative ability for pair exchange. In most superconductors exhibit multi-band conduction, but strong inter-band pairing ($V_{12} >> V_{11}, V_2$) leads to the same gap magnitude on all the bands (Fig. 1.15 c). Due to interband pairing, a smaller band will be pushed to the same transition temperature as the strong coupling band, resulting in a single transition temperature for the material.

If there is no interband pairing, i.e., $V_{12} = 0$, then each of the superconducting bands will behave differently and have different critical temperatures as shown (Fig. 1.15 a).

If $V_{12} << \sqrt{(V_{11}V_{22})}$, then only weak interband pairing occurs. In this case, if two gaps have sufficiently different magnitudes, then they can be resolved experimentally. The evolution of gaps in the case of weak pairing is depicted in Fig. 1.15 b. For measurements like resistivity, the fingerprint of a second band is usually weak because the zero resistance transition that occurs already from the stronger coupling band; will mask the resistance transition of the weak coupling band. In order to investigate the two bands, the momentum resolved probes like directional PCAR spectroscopy (point contact Andreev reflection) are the most effective ways.

Although this multigap or multi-band superconductivity was already addressed theoretically in 1959, it was first conclusively found in the MgB_2 compound only in 2001-2002 [17, 18, 47]. This compound has unusual superconducting properties, including a reduced heat capacity jump, a highly anisotropic critical field with extremely high values (20 T in bulk, 32 T in thin films), and non-BCS behaviors of various superconducting parameters like superfluid density and superconducting heat capacity [18, 19, 20, 21],. All of these anomalous features have been successfully explained using two-gap *s*-wave models of superconductivity. Further, band structure calculations of the Fermi surface also confirmed the existence of at least two bands with different characters. One band is a heavy hole band made up of Boron-σ orbitals, whereas the other has a smaller gap and is made up of Boron-π orbitals. There are now many other superconductors known to exhibit multigap superconductivity.

Some Iron based superconductors are also reported to show unconventional behaviour similar to that observed in MgB_2. $Lu_2Fe_3Si_5$ [48, 49], $FeSe_x$ [50] and FeS [51] compounds also show multigap superconductivity. The so-called "11" and "122" families of Fe-based high temperature superconductors (Fe-HTSs) are also reported to show multiple superconducting energy gaps [52]. Measurements on single crystal of these compounds showed that the penetration depth anisotropy and upper critical field anisotropy resembles with that of MgB_2.

1.9 Layered Borides

The BCS theory of superconductivity suggests that elements having low atomic mass can result in higher phonon frequencies which may, in turn, cause higher superconducting transition temperatures. Light elements such as Lithium (Li) and Beryllium (Be) have been shown to exhibit superconductivity but at high pressures [53]. However, the discovery of superconductivity in MgB_2 at 39 K [17] strongly supports the prediction of higher T_c in materials with lighter elements. This discovery has sparked a renewed interest in this material and materials with similar structural characteristics. The critical temperature of MgB_2 is higher than the value of T_c predicted by the BCS theory. MgB_2 shows traits of conventional superconductors such as isotope effect, and shift of T_c to lower values with the application of the magnetic field. However, the quadratic T-dependence of the penetration depth $\lambda(T)$ and reversal of the sign of Hall coefficient indicates the unconventional behavior as observed in high-T_c cuprates. The observation of conventional and unconventional behavior in MgB_2 is interesting, and the key to this behavior may lie in the crystal structure of MgB_2 [18, 19, 20, 21].

MgB_2 exhibits a hexagonal structure (Fig. 1.16) of AlB_2 type with space group $P6/mmm$. This type of structure is common among the boride compounds [53]. The structure of MgB_2 is a layered structure (as observed in cuprates) with graphite-type

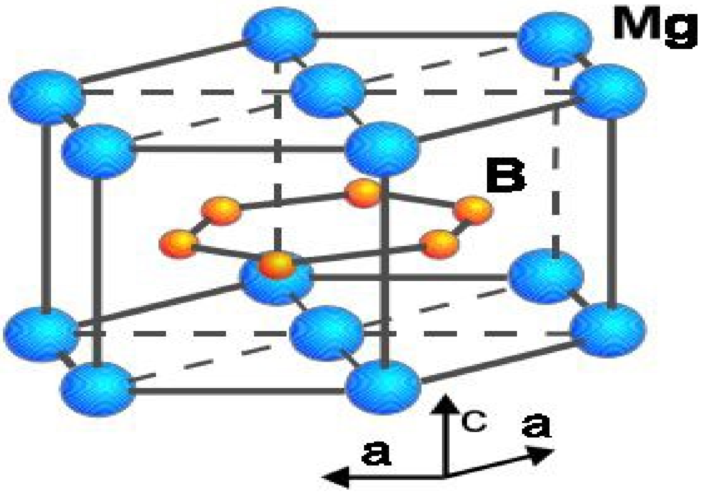

Figure 1.16: Crystal structure of MgB_2. (Reprinted from **Supercond. Sci. Technol. 14 R115**)

layers of Boron separated by hexagonal closed pack (HCP) layers of magnesium. Each magnesium atom lies on top of the center of the hexagons formed by the Boron atoms and donates their electrons to the underlying Boron layer. Calculations of the band structure of MgB_2 revealed that there are at least two types of bands at the Fermi surface. The first is a small band made up of boron σ orbitals, whereas the second is a larger band made up mostly of π boron orbitals with a reduced effective mass. The distance between boron layers leads to a very strong coupling of -bonding states to in-plane vibrations of boron atoms. This strong coupling results in the formation of strong electron pairs, which are the principal contributors to the superconducting properties of MgB_2 [47]. The possibility of unconventional superconductivity and high T_c in diborides has led to a lot of work on diboride compounds. A lot of structurally related compounds (TB_2; T= Ti, Zr, Hf, V, Cr, Nb, Ta, and Mo) have since been investigated for superconducting properties. Among the binary diborides, OsB_2 and RuB_2 are compounds that form an orthorhombic structure with *Pmmn* space group and are reported to become superconductors at 2.1 K and 1.6 K respectively[54, 55]. These materials also exhibit a layered structure, but it is different from that of MgB_2 and other compounds in this family with AlB_2 type structure. Instead of the graphite-like arrays of boron atoms which are separated by layers of transition metal atoms in an HCP arrangement, OsB_2 and RuB_2 have sheets of a deformed 2-dimensional network of puckered boron hexagons. These boron sheets lie between the layers of transition metal atoms, as shown in the (Fig. 1.17)[56, 57, 58, 54].

Early experimental studies on MgB_2 [59, 60, 61, 62, 63] indicate the presence of

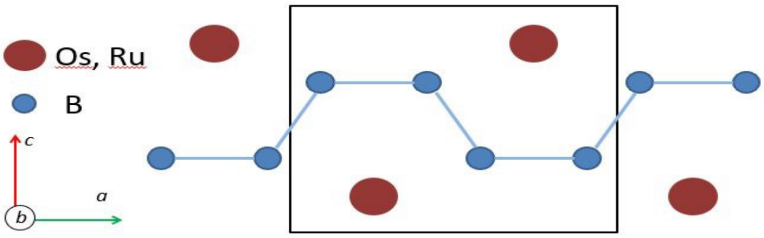

Figure 1.17: Crystal structure of AB_2 (A= Os, Ru)

multiple superconducting gaps, and the ab-initio studies on MgB_2 in reference [47] explaining these gaps opens an avenue of multi-band superconductivity in boride superconductors. The superconducting properties of OsB_2 have been investigated by previously [54, 64] and it was reported that the materials show the signature of unconventional superconducting properties like MgB_2. Although many superconducting properties of OsB_2 can be explained in the two-gap models of superconductivity, there is another study that suggests superconductivity in OsB_2 with single but highly anisotropic gap [65]. However, the mechanism of superconductivity is still uncertain. The pressure measurements and mass isotope effect suggest that MgB_2 is an electron-phonon coupling superconductor. Similar studies need to be done on OsB_2. The RuB_2 compound, which is isoelectronic and isostructural to OsB_2 can also be a candidate to exhibit similar anomalous superconducting properties as observed in OsB_2 and MgB_2. Another class of metallic boride compounds with interesting superconducting features are rare earth ternary borides RTB_2 that exhibit a relatively large value of superconducting temperature [66]. Stoichiometric RTB_2 (R: Rare earth; T: transition metal) phase crystallizes in an orthorhombic structure (space group *Pnma*), having a zigzag chain of rare-earth atoms, with dimerized Boron. Compounds with R = Y, Lu have been reported to exhibit a large superconducting transition temperature of $T_c \approx 7$, and 10 K [67, 68], and have also been reported to have a reduced heat capacity anomaly at T_c compared to weak-coupling BCS predictions. It is important to investigate the superconducting properties of the $RRuB_2$ (R = Y, Lu) compounds in detail in the search for unconventional behavior and mechanism of superconductivity exhibited by these compounds.

In this thesis we have studied the superconducting properties of TB_2 (T = Os, Ru) and $RRuB_2$ (R = Y, Lu).

CHAPTER 2

Experimental Details

This thesis contains an extensive study on poly-crystalline RuB_2, OsB_2, $LuRuB_2$ and $YRuB_2$ materials. This chapter discusses the detailed procedure of synthesis, structural characterization, and physical property measurement. The arc melting furnace has been used to synthesize the poly-crystalline samples of RuB_2, OsB_2, $LuRuB_2$ and $YRuB_2$. In order to improve the quality of the materials, further annealings were done in a vacuum tube furnace/box furnace.

2.1 Sample Preparation: Arc melting technique

Arc melting technique is commonly used to synthesize alloys by melting the metals [69]. In this technique, the materials are heated through an electric arc generated using high voltage/current via tungsten electrodes. The sample is placed on a copper hearth, which remains cool through cold water circulation using a commercial water chiller. The chamber is evacuated using a turbopump and then slightly filled with inert (Argon) gas to avoid material oxidation at high temperatures. The following significant steps were used to synthesize materials using arc melting techniques.

- The sample is placed below the tungsten electrode on a copper hearth. In this thesis, the furnace used to synthesize materials contains four tungsten electrodes, a so-called tetra arc furnace.

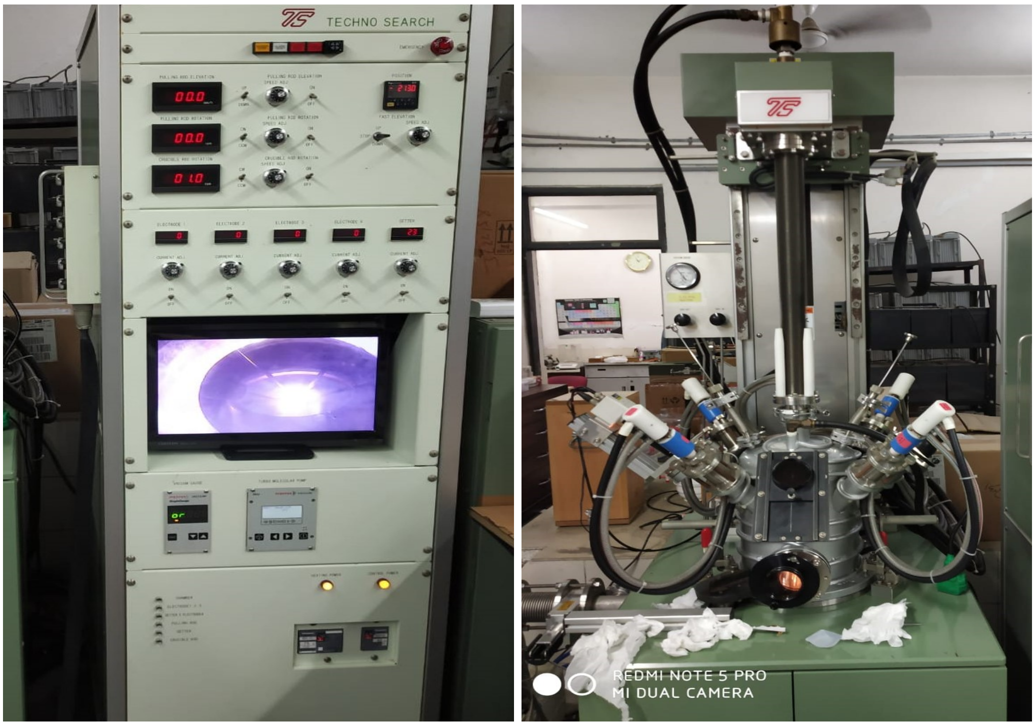

Figure 2.1: Tetra Arc Furnace, Left-side: The electric control unit and monitor screen , Right-side: Sample Chamber.

- The sample chamber is first evacuated using turbopump up to 1x10^{-6} mbar, then a low amount of argon gas ($\approx$3mbar) is filled to help make the electric arc.
- , In the beginning, a titanium getter is heated on a second small copper hearth in the chamber, since, at high temperature, titanium is a good absorber of gases which helps further purification of the sample chamber.

To make the material homogeneous, several heat treatments were given to the materials. In order to remove thermal defects, further annealing is done in a tube furnace in the presence of argon gas.

In the following, we describe the synthesis procedure used to make specific materials discussed in this thesis.

2.1.1 The synthesis procedure of RuB_2, OsB_2, $LuRuB_2$ and $YRuB_2$ compounds.

The polycrystalline sample of RuB_2 has been synthesized using arc melting techniques. The starting materials of Ru (5N, Alfa Aesar) and B (6N, Alfa Aesar) were taken in stoichiometric ratio. The materials are placed on a copper hearth, cooled

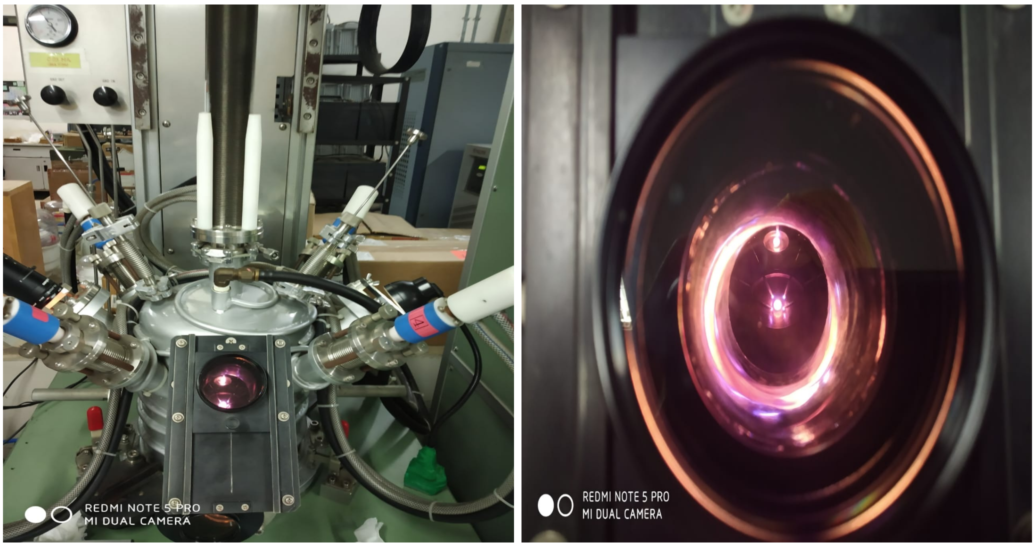

Figure 2.2: Image of material during melting

with a water chiller at 17°C. Zr was used as a getter to absorb all remaining Oxygen present in the vacuum chamber. The sample was flipped and melted 7-10 times to ensure homogeneous mixing. After melting, any weight loss was compensated by adding the required amount of boron and again melting. Figure 2.2 showed the images of material during melting.

As mentioned above, a similar procedure has been used to synthesize OsB_2, $LuRuB_2$, and $YRuB_2$. RuB_2 and OsB_2 compounds melt congruently. However, the $LuRuB_2$ and $YRuB_2$ compounds contain some small impurity phases even after several arc melting. Further annealing of the above samples was done after sealing in an evacuated quartz tube to improve the desired phase.

2.2 Structure Characterization: X-ray diffraction

The X-ray diffraction method is a frequently used technique for determining the crystal structure of any solid compound. It determines how the crystal's inner atoms or molecules are arranged. The first step after preparing any sample is the characterization of a crystalline material's phase. To do so, we first looked at its crystal structure and checked the sample's phase purity. X-rays are electromagnetic waves with wavelengths $0.5 - 2.5$ Å that are similar to the spacing between atoms in crystalline substances. The X-ray diffraction experiment has shown to be a handy tool for characterizing crystal structures. The systematic diagram of Bragg's X-ray diffraction is shown in figure 2.3.

W. L. Bragg and W. H. Bragg proposed an x-ray diffraction theory. According to

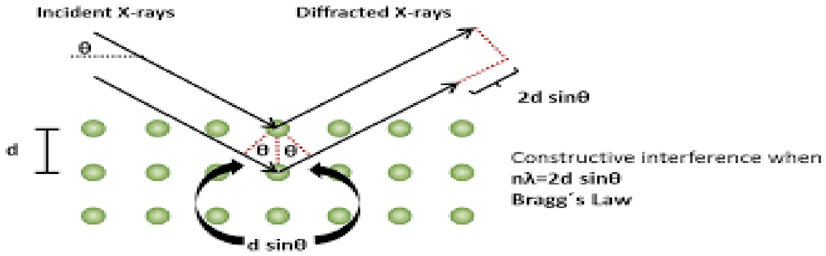

Figure 2.3: Schematic diagram of X-ray diffraction fullfilling Bragg's law

this idea, a crystal is made up of various sets of parallel atomic planes with identical interplanar spacing. Incident X-rays are reflected by parallel planes in the crystal, and the reflected rays are subsequently subjected to constructive interference. Bragg established Bragg's law, a simple mathematical condition Eq. 2.1 for observing a Bragg reflection [70].

$$2dsin\theta = n\lambda \tag{2.1}$$

where d is the inter-planar spacing between the (hkl) crystal planes, λ is the incident x-ray wavelength, θ is the incidence angle, and n is the order of reflection as a positive integer. To fulfill Bragg's criteria, either θ or λ needs to vary. The most common way is to fix the wavelength of the X-ray source and vary θ, and the intensity is measured vs 2θ. Bragg reflections are acquired at various 2θ values that satisfy the Bragg criterion. The intensity of peaks can be used to determine the unit cell characteristics of crystal structure and the arrangement of atoms.

where d is the inter-planar spacing between the (hkl) crystal planes, λ is the incident x-ray wavelength, θ is the incidence angle, and n is the order of reflection as a positive integer. To fulfill Bragg's criteria, either θ or λ needs to vary. The most common way is to fix the wavelength of the X-ray source and vary θ, and the intensity is measured vs. 2θ. Bragg reflections are acquired at various 2θ values that satisfy the Bragg criterion. The intensity of peaks can be used to determine the unit cell characteristics of crystal structure and the arrangement of atoms.

All polycrystalline samples were subjected to powder X-ray diffraction studies at the powder x-ray diffraction (PXRD) facility IISER Mohali, utilizing a Rigaku Ultima high-resolution X-ray diffractometer. We chose an angular range of 10° to 90° with a step size of 0.02° and a sample rotation speed of 120 rpm for our experiments. We examine phase purity by matching the obtained x-ray pattern with the expected data from the International center for diffraction database (ICDD) PDF-4 using PCW software after collecting experimental x-ray data of manufactured materials. General Structure Analysis Software (GSAS) [71] is used to refine Rietveld for better quantitative analysis.

2.3 Physical Property Measurement

After the synthesis and characterization of materials, the next step is to measure their physical properties. In this thesis, we investigated the superconducting properties of some rare-earth and transition metal borides, for which temperature and field-dependence magnetization, electrical resistivity, and heat capacity measurements were required. We used the Quantum Design (QD) Evercool-II Physical Property Measurement System (PPMS) with a superconducting magnet up to 9T.

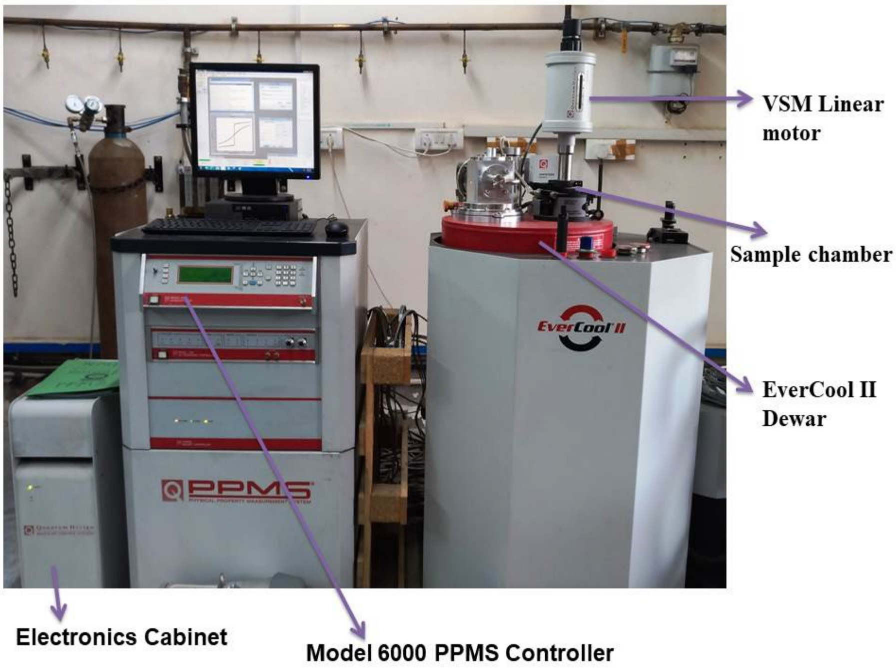

Figure 2.4: Quantum Design (QD) Physical Property Measurement System (PPMS)

2.3.1 Electrical Resistivity Measurements

The temperature and field dependence electrical resistivity between 2 K and 300 K is measured using the standard four-probe electrical transport option (ETO) in Quantum Design PPMS Evercool-II. Standard PPMS sample pucks as shown in figure 2.5 are used to attach samples for four-wire resistance measurements. The

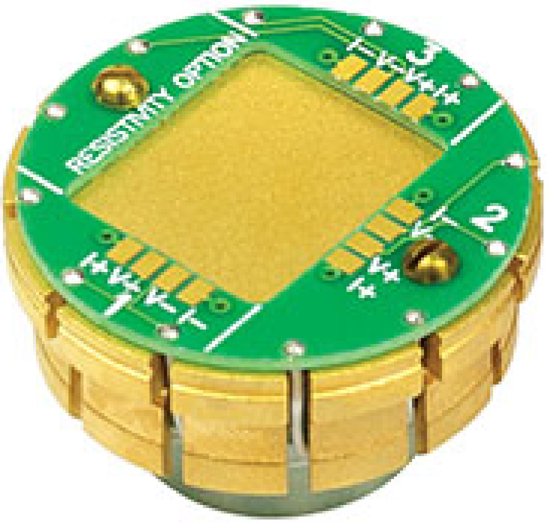

Figure 2.5: Quantum Design Resistivity Puck

resistivity sample pack has four contacts, two for sending current and two for measuring voltage [72]. The contribution of the leads and joints to the resistance measurement is considerably reduced when a sample is attached to a sample puck using four wires figure 2.6. Two current leads carry current through a sample, and two separate voltage leads detect the potential difference across the sample in a four-wire resistance measurement. The voltage leads draw a tiny current since the voltmeter has a very high resistance. A perfect voltmeter, in theory, draws no current at all. As a result, using the four-wire method can determine both the current and the voltage drop across the sample with a high degree of precision and compute the resistance using Ohm's law. The silver epoxy or paint from Ted Pella, INC has been used to make contacts on the sample. Quantum Design Resistivity option provides the current limit between $0.01 - 5000\ \mu$A and voltage limit between $1 - 95$ mV.

2.3.2 Vibrating sample magnetometer (VSM)

Experiments on magnetic materials necessitate using a device that can precisely measure the magnetization of any magnetic substance. The technique of vibrating sample magnetometry (VSM) is an effective way to determine the magnetization of any magnetic substance. S. Foner is the inventor of this technology [73], which works on the idea of electromagnetic induction.

In the VSM option, the magnetic sample oscillates sinusoidally inside a pick-up coil figure 2.7. The oscillating sample (magnet) produces an electromotive current in the pick-up coil, which is proportional to the magnetization of the magnetic sam-

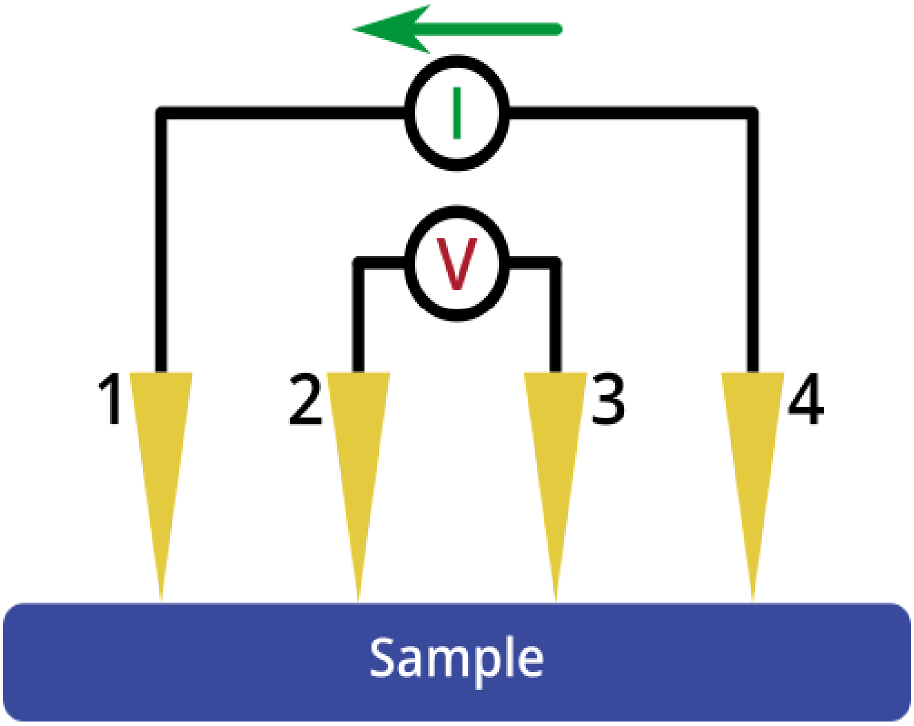

Figure 2.6: Four probe electrical resistivity measurement diagram

ple. Hence the VSM option consists of a pick-up coil to pick the current, a linear motor to move the sample up and down, a lock-in amplifier to lock the drive frequency signal, and an electronic setup to control the motion of the linear motor. The pick-up coil of VSM has two counter-wounded coils (clockwise wounded coil with x sign and counterclockwise with · sign) separated by a few mm, as shown in figure 2.7. The magnetic sample oscillates around one coil, and the second coil is used to cancel the signals coming from the background and sample holder. An oscillating sample produces an inductive voltage in pick-up coils which are separated by background signals. Hence, we finally get the value of magnetization from the sample only. We have used the commercial VSM option of QD PPMS to measure all the magnetization data. The time-dependent voltage induced by the motion of the magnetic sample in the pick-up coil follow the following equation:

$$V_{coil} = \frac{d\phi}{dt} = \frac{d\phi}{dz}\frac{dz}{dt} \tag{2.2}$$

Where ϕ is the change in magnetic flux by the motion of the magnetic sample, z is the vertical position of the sample, and t is time. The linear motor can operate up to 40 Hz frequency which gives high sensitivity and can measure the magnetic moment down to 10^{-6} emu. The vibrating sample magnetometer gives the magnetic moment of any magnetic sample in emu (CGS unit) or Am^2 (SI) unit.

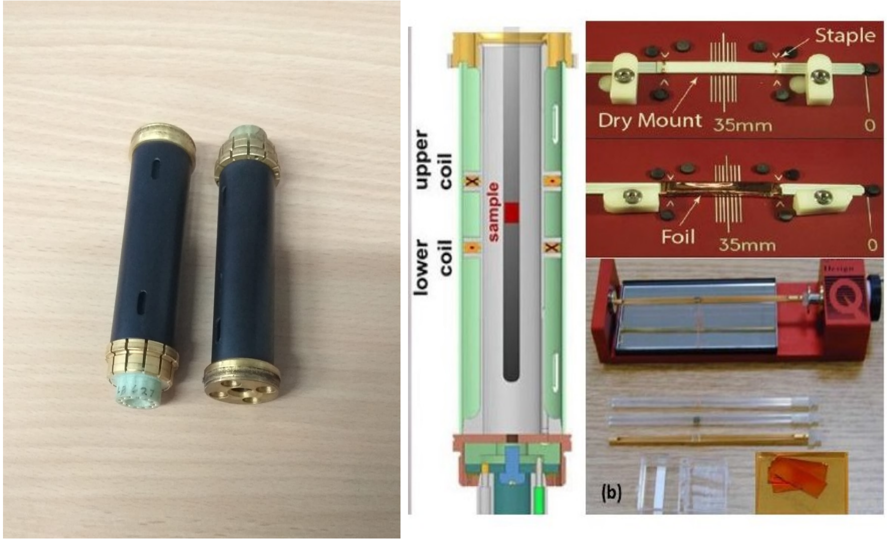

Figure 2.7: Left: Pick up coil, Middle: Pick up coils setup, Right: sample mounting platform

2.3.3 High Pressure Magnetic Measurements

In this thesis, we have studied the effect of pressure on the superconducting transition temperature using a High-Pressure Cell manufactured by Quantum Design Japan. The high-pressure cell is made of Beryllium Copper, which can hold a maximum of up to 1.3 GPa. It can be used with the QD-PPMS VSM option. The systematic diagram of the high-pressure cell is given in the figure 2.8. The sample is placed in a Teflon tube with pressure transmitting media (Daphne 7373 oil). A material whose pressure vs. magnetization is well known is used to calculate the exact measure of applied pressure. Lead (Pb) and Tin (Sn) wires have been used to calculate the applied pressure in this work. Figure 2.9 shows a typical cell compression vs sample load for the pressure cell. The applied pressure can be estimated by measuring the shift in T_c of Pb or Sn; e.g, for Pb if we know the shift in T_c, the corresponding change in pressure is estimated using:

$$dP(GPa) = \frac{dT(K)}{0.379(K/GPA)} \tag{2.3}$$

2.3.4 Heat Capacity

The thermodynamical measurements are essential in researching phase transition because they provide additional information that cannot be gained from magnetization data alone. The amount of heat required to raise a substance's temperature by

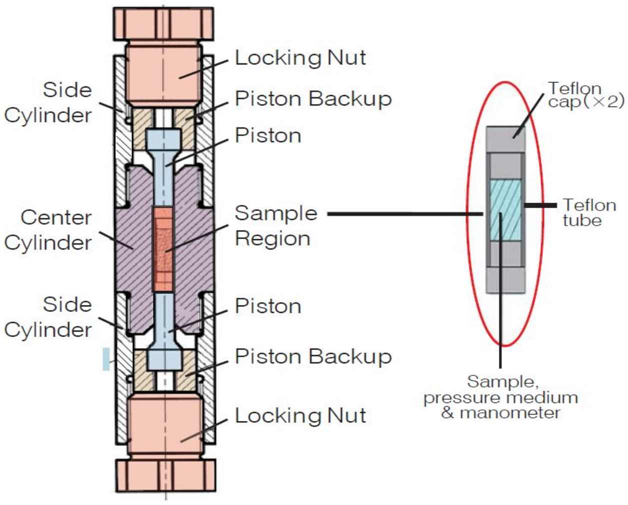

Figure 2.8: Diagram of High Pressure Cell Construction

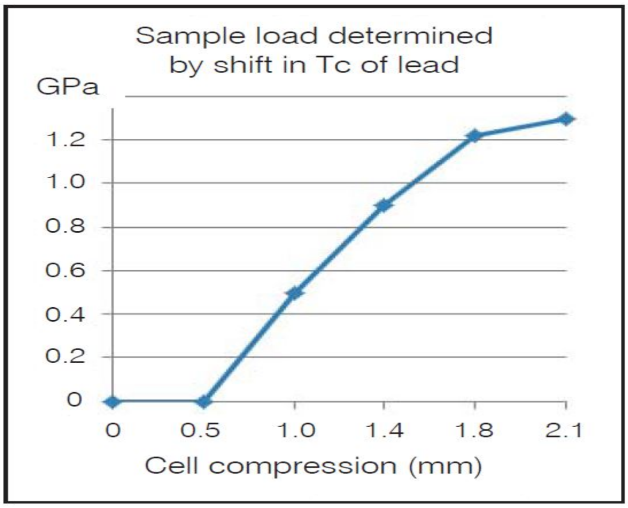

Figure 2.9: Typical sample load vs cell compression. The sample load is determined by measuring the shift in T$_c$ of a Pb manometer.

one unit is known as its heat capacity. It is a material's vast property. The heat capacity is divided by its mass to express the corresponding intense property (specific heat capacity), which may be computed using the following formula:

$$C = \frac{1}{m}\frac{\Delta Q}{\Delta T} \tag{2.4}$$

Heat capacity is an excellent tool for studying structural and magnetic phase transitions. All compounds addressed in this thesis have their heat capacity assessed using the heat capacity option in QD PPMS. The heat capacity of any substance can be measured using a variety of approaches; QD PPMS uses a relaxation technique

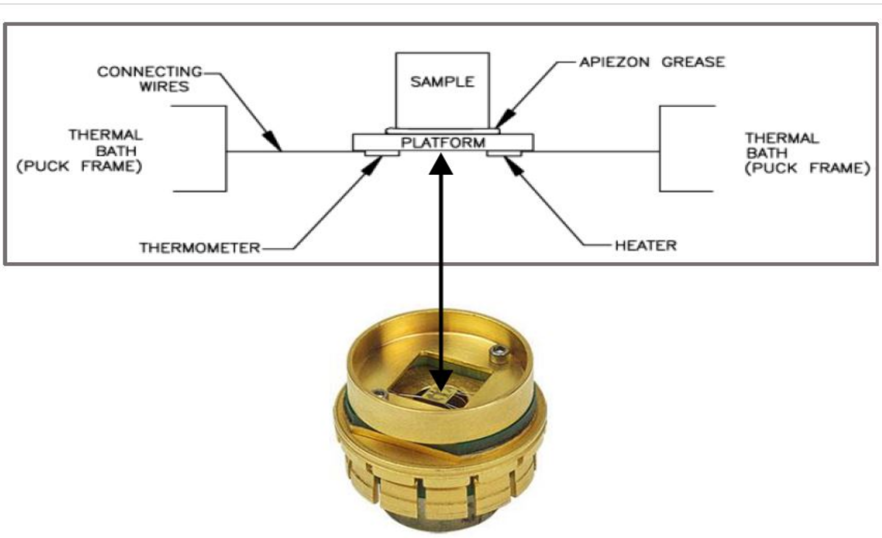

Figure 2.10: Schematic of Heat capacity puck designed by QD

[74]. The sample is placed on a platform connected to a bath with a weak thermal link and a constant temperature T_0. The sample is given a well-defined heat pulse that raises its temperature by ΔT (typically ΔT/T = 1%) to accomplish the measurement. The heater is then turned off, and the sample's temperature begins to fall until it reaches the bath temperature. The relaxation time τ can be estimated using the following relation:

$$T_S = T_o + \Delta T(exp(-t/\tau)) \tag{2.5}$$

The heat capacity is then calculated using the relaxation time τ relationship, which has the following relationship with the weak thermal link has known thermal conductivity κ:

$$C = \tau\kappa \tag{2.6}$$

Figure 2.10 shows the schematic design of a heat capacity puck. The platform's bottom side is where the heater and thermometer are linked. Apiezone-N grease is used to adhere the sample to the platform. The grease also acts as a thermal interface between the sample and the platform. A high vacuum of magnitude $10-6$ mbar is used to achieve the adiabatic condition.

Since this technique of measuring heat capacity is dynamic in nature, the thermal diffusivity and geometry of the sample must be such that the thermal diffusion time in the sample should be small compared to the time constant of the measurement. Otherwise sample will not reach the thermal equilibrium in time constant of measurement. In this thesis work, the materials under investigation are metallic means good thermal conductor and hence have sufficiently low diffusion time.

2.3.5 Point-Contact Andreev Reflection Spectroscopy (PCAR)

Many superconducting properties such as superconducting energy gap, phonon spectra and spin polariazation can be measured using PCAR spectroscopy technique [75, 76]. Isotropic as well as anisotropic superconducting energy gap can be measured using this technique. In this method, electrons are given an eV energy boost when they travel via a microcontact between two electrodes separated by a potential difference V. If the contact's lateral dimension is less than the typical length scale of the electrode materials, the contact is referred to as a point contact. In a metal the elastic and inelastic mean free paths of the electrons define the length scale. this spectroscopy technique studies the non-linearity of the current-voltage characteristics resulting from the elastic and inelastic scattering of the electrons. The point-contact Andreev reflection spectroscopy's connection design is depicted in Figure 2.11. In this technique current is sent across two electrodes while measuring the voltage drop across the other two electrodes.

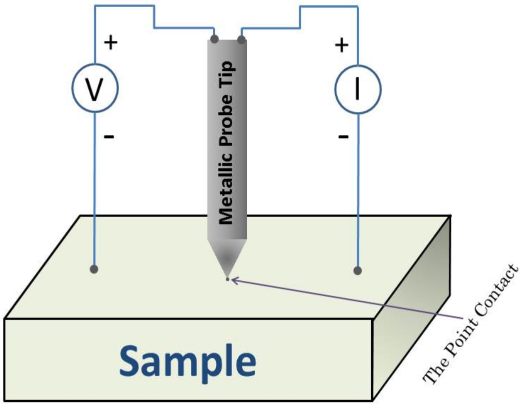

Figure 2.11: Connection design of point-contact spectroscopy..

When a voltage is applied to the normal-metal superconductor interface, the electron can be transported into the normal state on the superconducting side if the energy gained by electrons is greater than the superconducting energy gap. Since there is a superconducting energy gap and no states are available on the superconducting side, if the electron's energy is less than the superconducting energy gap, it cannot enter the superconducting state. In order to save energy, an electron that strikes the interface will then reflect back as a hole in the spin-down band, which will then result in the formation of a single cooper pair at the Fermi level on the superconducting side, turning a normal current into a supercurrent. This phenomenon is known as Andreev reflection [77]. This Andreev reflection can be measured using $\frac{G(V)}{G_n}$ vs. V characteristics, where $\frac{G(V)}{G_n}$ is called normalized conductance with G(V) $= \frac{dI}{dV}$ and V is the applied volatage. The point-contact Andreev reflection spectrum refers to this characteristic.This spectrum can be fitted by Blonder-Tinkham-Klapwijk (BTK) model [78].

CHAPTER 3

Superconducting properties of the layered transition metal borides TB_2 (T = Os, Ru)

3.1 Introduction

Superconductors with anomalous properties, which are different from conventional superconductors, are always interesting to study and challenging to understand. Following the report of high T_c superconductivity in MgB_2, which has a layered crystal structure, and subsequent discovery of its multigap nature [18, 47], there has been increased interest in investigating metal borides with similar structures. There are now several accepted candidate multi-gap superconductors such as $NbSe_2$ [79], RNi_2B_2C ($R=$ Lu and Y) [80], $Lu_2Fe_3Si_5$ [48, 49], Sr_2RuO_4 [81], and more recently FeSe [50, 82]. As discussed in chapter 1, the distinct superconducting gaps exist on different disconnected sections of the Fermi surface in multigap superconductors. Interbrand paring in most superconductors results in a single transition temperature for the material and the same gap magnitude on all bands. When interband pairing is weak, and the magnitudes of two gaps are sufficiently different, the distinct gaps can be resolved experimentally. Multigap superconductors are associated with several anomalous superconducting properties. For example, a reduced heat capacity jump at the superconducting critical temperature $\Delta C/\gamma T_c$, a non-BCS temperature dependence of the upper critical field, and a non-BCS penetration depth versus temperature. These anomalous properties are mostly connected with Fermi surface sheets with very different characters. This is exemplified most clearly in the case of MgB_2 [83, 84, 85, 86]. Transition metal boride compounds have several ingredients which make them candidates for novel superconductivity. The transition metal elements provide the possibility of multiple orbitals, which can make up a Fermi surface with many sheets. The light mass of Boron could provide for a high Tc. Additionally, they have layered or quasi-low-dimensional structural motifs.

Recently OsB_2, which has a layered structure with puckered honeycomb Boron planes alternating with Osmium planes stacked along the c-axis of an orthorhombic cell, has been studied for its super-hardness as well as for its superconducting properties. Several anomalous superconducting properties like upward curvature in the $H_c(T)$ curve, reduced heat capacity anomaly at T_c, non-BCS temperature dependence of the penetration depth, a small Ginzburg-Landau parameters $\kappa \sim 1$–2, and a first-order superconducting transition in a magnetic field have been observed for OsB_2 [54, 64]. These properties were interpreted as signatures of two-gap superconductivity. A fit by a two-gap model to the T dependent penetration depth data gave the values $\Delta_1 \approx 1.25 k_B T_c$ and $\Delta_2 \approx 1.9 k_B T_c$ for the two gaps, respectively [64]. The Fermi surface of OsB_2 consists of a quasi-two-dimensional sheet and two nested ellipsoidal sheets [87]. The two gaps were argued to open on the two ellipsoidal Fermi surface sheets which are very similar in character and size [64] unlike the two gaps in MgB_2 which open on two Fermi sheets which are very different in character [86].

However, an alternate view has recently been put forward for these anomalous properties of OsB_2 with proposal of extreme Type-I superconductivity (very small κ) and a single but highly anisotropic gap [65].

RuB_2 is iso-structural to OsB_2 and is also reported to become superconducting below $T_c \approx 1.5$ K [55]. Although its normal state properties have been studied in detail [54], the superconducting properties have not been explored. Given the anomalous superconducting properties of OsB_2, it would be interesting to make a detailed study of the superconducting properties of RuB_2 to look for similar anomalous properties. Although unconventional superconducting properties of OsB_2 are attributed to either two gaps or to a single anisotropic gap, It is interesting to find, by different isotope substitution or by the effect of pressure on T_c that whether superconductivity is electron-phonon mediated or not. This chapter presents our investigations on the superconducting properties of polycrystalline samples of RuB_2 and effect of pressure on superconducting properties of OsB_2. Our high-pressure studies of OsB_2 suggest an electron-phonon mediated superconductivity in this compound.

We confirm that RuB_2 exhibits bulk superconductivity below a critical temperature $T_c = 1.5$ K. The magnetization versus magnetic field data suggest Type-I superconductivity. We estimate an electron-phonon coupling constant $\lambda_{ep} = 0.39$–0.45 suggesting moderate coupling superconductivity in RuB_2. The extrapolated $T = 0$ critical field $H_c(0) \approx 122$ Oe is small and consistent with Type-I superconductivity. The normalized heat capacity jump at T_c was estimated to be $\Delta C/\gamma T_c \approx 1.1$, which is much smaller than the value 1.43 expected for a single *s*-wave BCS superconductor and suggests multi-gap superconductivity. This is confirmed by obtaining an excellent fit of the electronic specific heat data below T_c to a phenomenological two-gap model. The fit gave the gap values $\Delta_1/k_BT_c \approx 1.88$ and $\Delta_2/k_BT_c \approx 1.13$ for the two gaps. The jump in the heat capacity at T_c becomes larger in applied magnetic fields again suggesting Type-I behaviour. These suggestions are confirmed by estimates of the Ginzburg Landau parameter $\kappa = 0.1$–0.6 which is smaller than the value $1/\sqrt{2} \approx 0.707$, the border between Type-I and Type-II superconductivity. Thus RuB_2 could be the first multi-gap Type-I superconductor. Additionally we calculate the band-structure and obtain the Fermi surface of RuB_2. The band structure confirms metallic behaviour with majority contribution to the density of states (DOS) at the Fermi energy (ε_F) coming from Ru 4*d* and B 2*p* orbitals. We calculate the total DOS at $\varepsilon_F = 1.17$ states/eV f.u., where "f.u." stands for "formulae unit". This value is similar to the value reported for OsB_2 [54] . The Fermi surface consists of 4 sheets. There is one quasi-two-dimensional corrugated tubular sheet and two nested ellipsoidal sheet, very similar to OsB_2 [54]. An additional small 4$^{\text{th}}$ sheet is found which was not obtained for OsB_2.

3.2 Experimental and Theoretical Methods

Polycrystalline samples of RuB_2 and OsB_2 were synthesized by arc-melting technique. High purity elements of Os (99.95%, Alpha Aeser), Ru (5N, Alfa Aesar), and B (6N, Alfa Aesar) have been used in sample preparation. The required elements have been taken in stoichiometric ratios and arc-melted 5–10 times to promote homogeneity [54]. Powder x-ray diffraction confirmed that the synthesized materials are in single-phase and refinements, shown in Figure 3.1 of the powder X-ray pattern provided lattice parameters that match well with the reported values [54]. The magnetization M versus temperature T data for OsB_2 sample were measured from 1.9 K to 2.6 K by applying different pressure using an Easylab Mcell-10 pressure cell with the VSM option of a Quantum Design Physical Properties Mea-

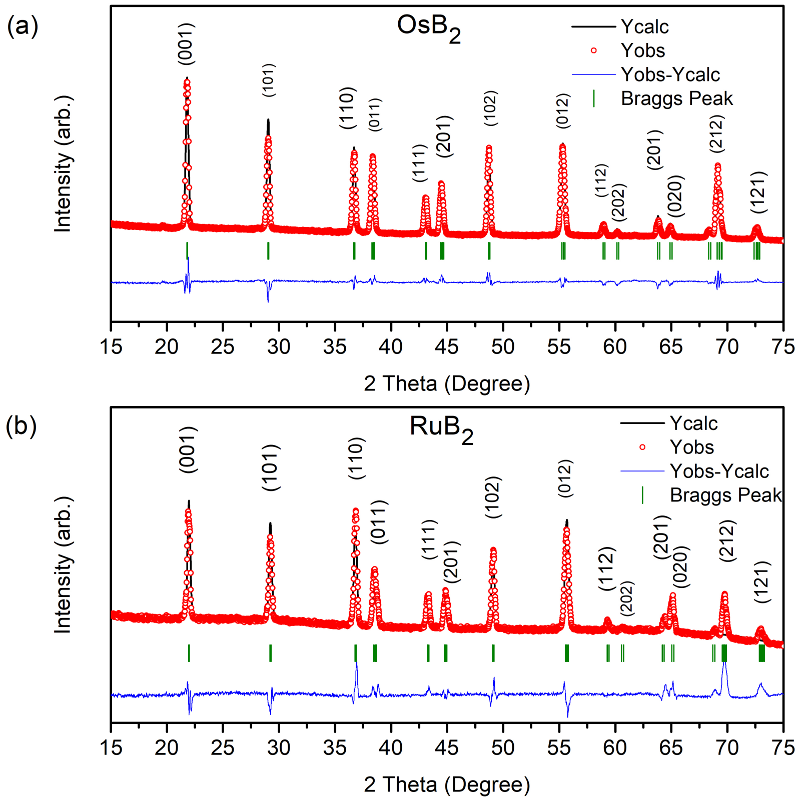

Figure 3.1: Refinements of the OsB_2 and RuB_2 powder X-ray diffraction data. The open symbols represent the observed X-ray diffraction pattern, the solid black lines represent the fitted pattern, the solid blue lines represent the difference between the observed and calculated intensities and the peak positions are represented by the vertical bars.

surement System (QD-PPMS). For RuB_2 sample, various measurements have been performed to find its superconducting properties. The dc magnetic susceptibility χ versus temperature data in the temperature range $T = 0.280$ K to 2 K and magnetization M versus field H data at $T = 310$ mK were measured using a He3 insert in a SQUID magnetometer from Cryogenics Limited, UK. The heat capacity C data from 85 mK to 3 K was measured sample using the dilution refrigerator (DR) option of a Quantum Design Physical Property Measurement System (QD-PPMS). The electrical transport from 300 mK to 300 K was measured using the He3 insert in a QD-PPMS. The first-principles density functional theory (DFT) calculations were done using the QUANTUM-ESPRESSO code [88]. Electronic exchange and correlation are described using the generalized gradient approximation (GGA) using Perdew-Bruke-Ernzerhof functional [89]. In the DFT calculation, spin-orbit coupling was not included. However, we have used scalar relativistic potential which takes scalar relativistic effects into account.

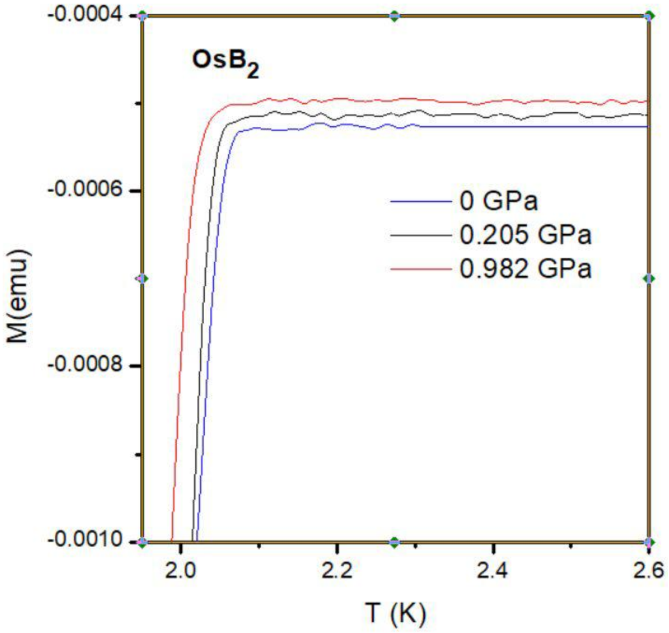

Figure 3.2: Magnetization M versus Temperature T for OsB_2 measured at various pressures.

3.3 Pressure Measurements on OsB_2 Superconductor

Figure 3.2 shows the results of magnetization M versus temperature T data for OsB_2 measured between 1.9 K to 2.6 K at various applied pressures. At 0 GPa pressure, a sharp drop in M confirms the superconducting transition with transition temperature $\approx$ 2.1 K. As we increase the pressure, a shift in T_c to lower values is clearly visible. At pressure of 0.982 GPa, superconducting transition temperature shifts below 2 K. As we have discussed in chapter 1, for conventional BCS superconductors the superconducting transition temperature is related to the lattice spring constant k as $T_\mathrm{c} \approx \sqrt{\frac{k}{M}} \exp\left\{\frac{-k}{N(\varepsilon_\mathrm{F})\langle I^2\rangle}\right\}$, where $N(E_\mathrm{f})$ is the electronic density of states at Fermi level, $\langle I^2 \rangle$ is the average square electron-phonon scattering matrix element. The spring constant k increases most rapidly under pressure, whereas the denominator in the exponent is only weakly pressure-dependent. The minor increase in the prefactor k is overwhelmed by the reduction from the -k in the exponent, resulting in a decrease in T_c with increasing pressure for electron-phonon coupled superconductors. From these observations, we conclude that OsB_2 is an electron-phonon coupled superconductor.

3.4 Superconducting Properties of RuB_2

3.4.1 Electrical Resistivity

The electrical resistivity ρ versus temperature T data for RuB_2 measured with an excitation current of 5 mA in zero applied magnetic field are shown in Fig. 3.3 between $T = 0.5$ K and 315 K. The $T = 315$ K value of resistivity is $\rho(315\ \mathrm{K}) \approx 22.5\ \mu\Omega$cm and the residual resistivity is $\rho(1.6\ \mathrm{K}) \approx 1.1\ \mu\Omega$cm giving a residual resistivity ratio RRR ≈ 21. This indicates that the sample is of good quality. The inset in Fig. 3.3 shows the $\rho(T)$ data below $T = 5.25$ K to highlight the sharp drop to zero resistance below $T_c = 1.5$ K signalling the onset of superconductivity in RuB_2.

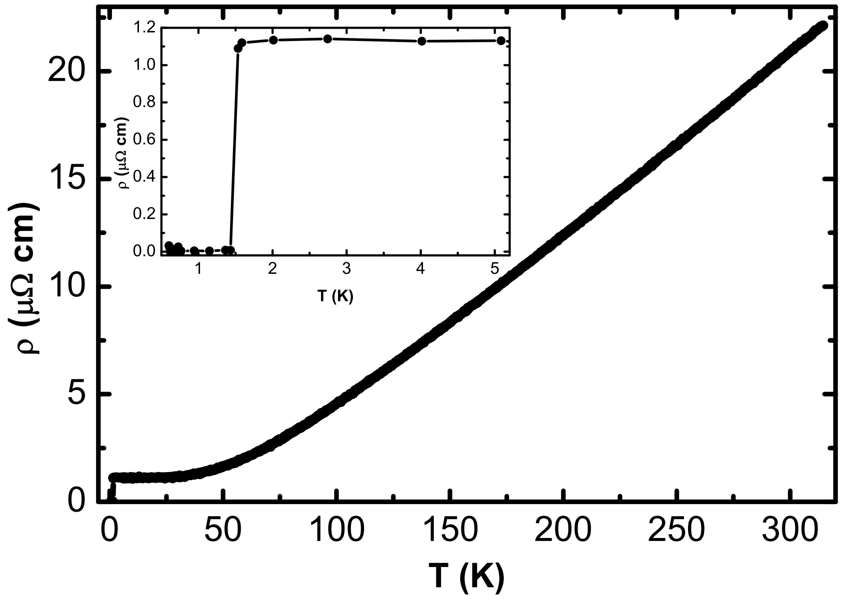

Figure 3.3: The electrical resistivity ρ versus temperature T for RuB_2 measured in zero magnetic field between $T = 0.4$–310 K. The inset shows the data below $T = 5.5$ K to highlight the abrupt drop at $T_c = 1.5$ K signalling the transition to the superconducting state.

3.4.2 Magnetic Properties

Figure 3.4 shows the results of magnetic measurements on RuB_2. Fig. 3.4 (a) shows the temperature dependence of the zero-field-cooled (ZFC) volume magnetic susceptibility χ_v normalized by $1/4\pi$. The data were measured in a field of 10 Oe between 0.28 K and 1.8 K. The sharp drop in χ_v to diamagnetic values below ≈ 1.55 K confirms the onset of the superconducting state. The inset in Fig. 3.4 (a)

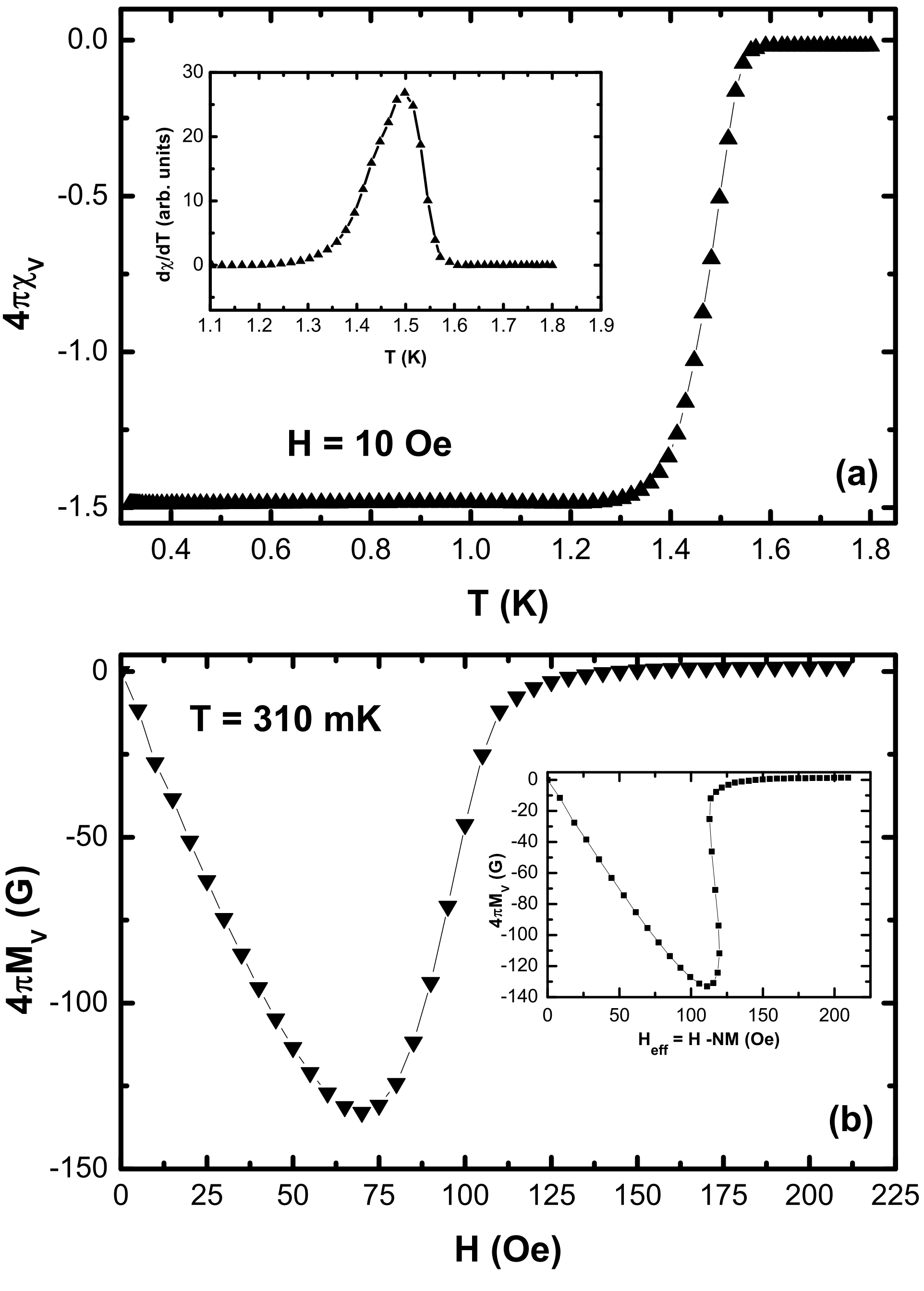

Figure 3.4: (a) The temperature T dependence of the zero field cooled (ZFC) dimensionless volume susceptibility χ_v in terms of the superconducting volume fraction $4\pi\chi_v$ of RuB$_2$ measured in a magnetic field $H = 10$ Oe. At low T, the $4\pi\chi_v$ values are more negative than -1 due to demagnetization effects. The inset shows the $d\chi/dT$ versus T data to highlight the superconducting transition at $T_c = 1.5$ K. (b) the volume magnetization M_v normalized by $1/4\pi$, versus applied magnetic field H measured at $T = 310$ mK. The inset shows the $4\pi M_V$ versus effective magnetic field $H_{\mathrm{eff}} = H - NM$ corrected for the demagnetization effects. These data show behaviour typical of Type-I superconductivity.

shows the $d\chi_v/dT$ vs T data and the peak position is taken as the superconducting critical temperature $T_c = 1.5$ K. The full-width-at-half-maximum (FWHM) of the peak in $d\chi_v/dT$ gives an estimate of the superconducting transition width and is ≈ 50 mK. The χ_v data have not been corrected for the demagnetization factor N. Thus, the observed value is $4\pi\chi_v = \frac{-1}{1-N}$ and therefore larger than -1 expected for 100% superconducting volume fraction. Assuming 100% superconducting volume fraction we estimate $N \approx 0.32$ from the data shown in Fig. 3.4 (a). However, often in polycrystalline samples the superconducting fraction is smaller than 100% and to estimate the actual superconducting fraction one needs the value of N. For idealized shapes of measured samples, N has been calculated. For example, $N = 1/3$ for a sphere and 1 for an ellipsoid of revolution. Our sample is an irregular shaped piece which looks like a squashed ellipsoid with dimensions $a \approx b = 1.61$ mm $\neq c = 1.35$ mm, broken from an arc-melted button. We therefore approximate our irregular shaped sample with a prolate ellipsoid with $c/a \approx 0.83$. For such an object, $N \approx 0.38$ [90]. Using this value of N we find a superconducting volume fraction of $\approx 90\%$.

Figure 3.4 (b) shows the volume magnetization M_v normalized by $1/4\pi$ versus magnetic field H for RuB_2 measured at a temperature $T = 310$ mK, well inside the superconducting state. The shape of the $4\pi M_v$ vs H data are very different from those expected for typical Type-II superconductors but are similar to that expected for a Type-I superconductor with demagnetization factors. To account for demagnetization effects the magnetization can be plotted versus an effective magnetic field $H_{\text{eff}} = H - NM$. This has been done using the $N \approx 0.38$ estimated above and the resulting $M(H_{\text{eff}})$ data are shown in Figure 3.4 (b) inset. These data look like the behaviour expected for a Type-I superconductor. The slight negative slope of the data at the transition most likely occurs from a slightly overestimated N.

3.4.3 Heat Capacity

Figure 3.5 (a) shows the specific heat C versus T data for RuB_2 measured between $T = 85$ mK and 3 K in magnetic fields $H = 0$ Oe and $H = 250$ Oe. A sharp anomaly near $T_c = 1.5$ K in the $H = 0$ data confirms bulk superconductivity in RuB_2. The data at $H = 250$ Oe doesn't show any signature of superconductivity and will be used as the normal state data. We will later show that this field is indeed much higher than the estimated critical field. The $C(T)$ data at $H = 250$ Oe were fit by the expression $C = \gamma_n T + \beta T^3$ where γ_n is the normal state Sommerfeld coefficient and the second term is the contribution from the lattice. The fit

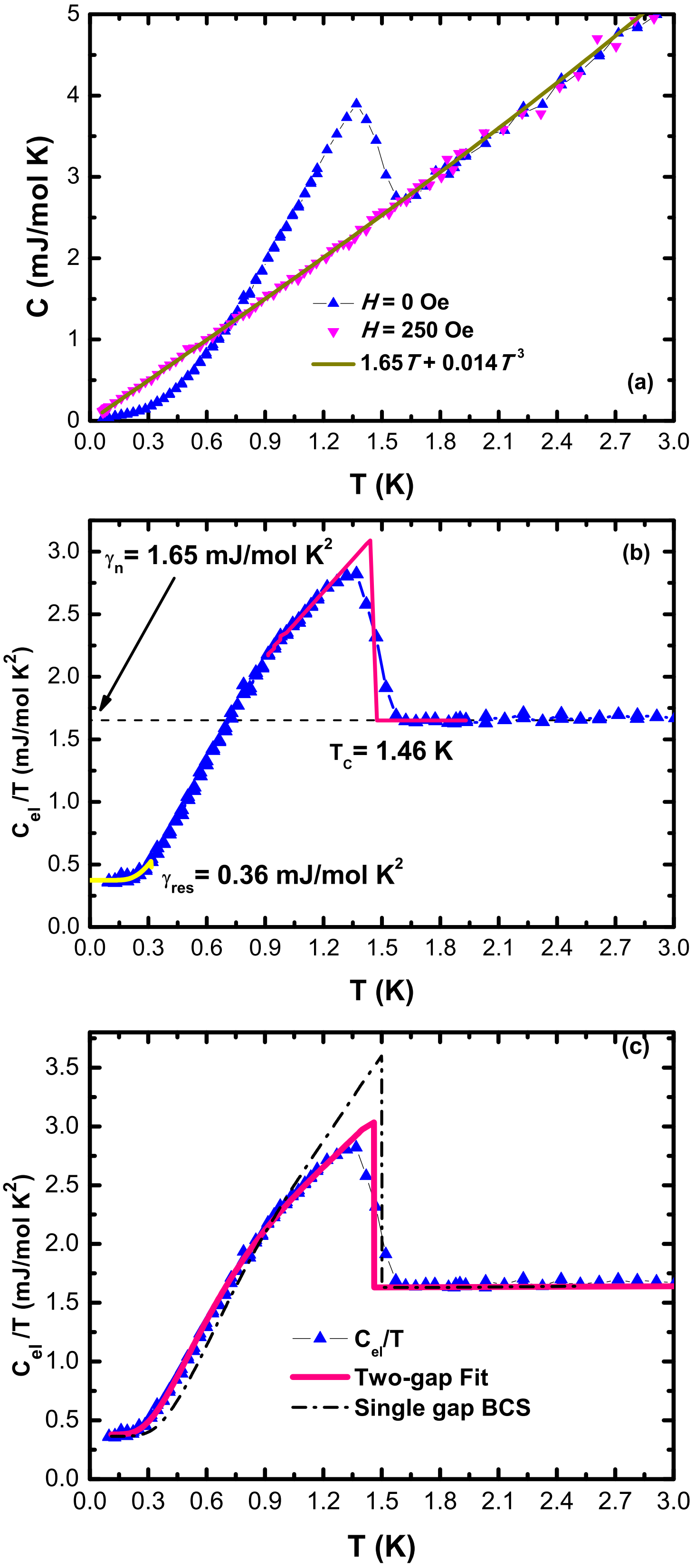

Figure 3.5: (a) Specific heat C versus T for RuB$_2$ measured in magnetic fields $H = 0$, and 250 Oe. (b) The electronic specific heat divided by temperature C_{el}/T versus T for RuB$_2$. An equal entropy construction is shown to give a $T_c = 1.46$ K and $\Delta C/\gamma T_c = 1.1$, where $\gamma = \gamma_n - \gamma_{res}$. (c) A two-gap model fit (solid curve) to the C_{el} data and expectation for a single BCS gap with $T_c = 1.5$ K (see text for details).

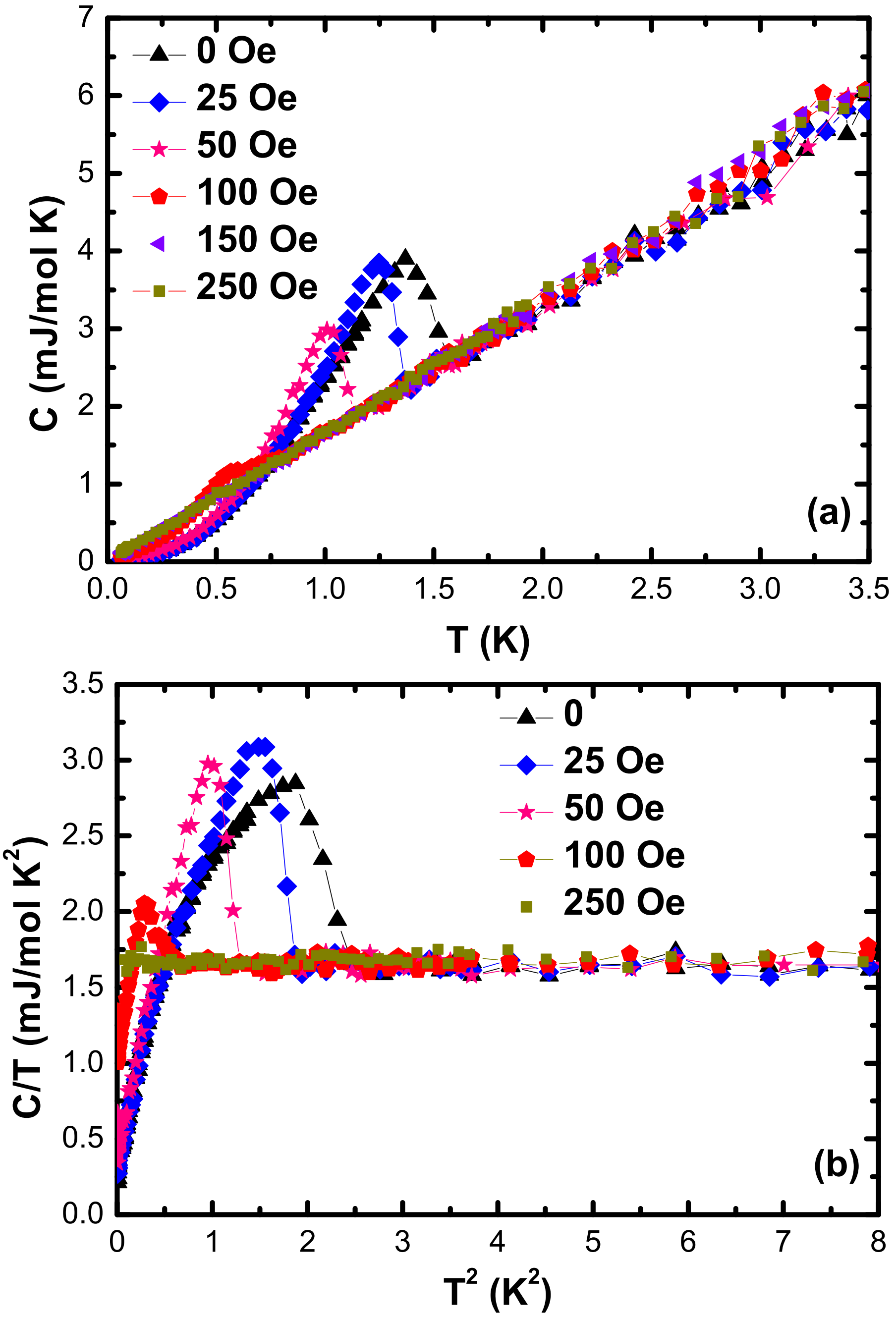

Figure 3.6: (a) Specific heat C versus T for RuB_2 measured in various magnetic fields H. (b) C divided by temperature C/T versus T^2 for RuB_2 at various H. The solid curve through the data is a fit by the expression $C = \gamma T + \beta T^3$. The peak height at T_c in zero field is characterised by the ratio $\Delta C/\gamma T_c$ and is estimated to be 0.8 for RuB_2.

shown as the solid curve through the $H = 250$ Oe data in Fig. 3.5 (a) gave the values $\gamma_n = 1.65(2)$ mJ/mol K^2 and $\beta = 0.014(2)$ mJ/mol K^4. This value of β gives a Debye temperature of $\theta_D = 720(30)$ K which is similar to the value found previously [64]. The lattice contribution βT^3 to the total specific heat $C(T)$ can be subtracted to get the electronic contribution $C_{el}(T)$. The $C_{el}(T)$ so obtained is shown in Fig. 3.5 (b). The sharp anomaly at T_c as well as the exponential fall at the lowest temperatures expected for s-wave superconductors is clearly visible. We also note that C_{el} tends to a finite value as $T \to 0$ suggesting some non-superconducting fraction in the sample. The data below ≈ 0.3 K were fit by the expression $C_{el}/T = \gamma_{res} + (A/T)exp(-\Delta/T)$, where γ_{res} is the residual Sommerfeld coefficient from the non-superconducting fraction of the sample and the second term is a phenomenological exponential decay expected for a gapped system. The fit shown as the solid curve through the data below $T \approx 0.3$ K in Fig. 3.5 (b) gives the value $\gamma_{res} = 0.36$ mJ/mol K^2. With the total $\gamma_n = 1.65$ mJ/mol K^2 and the residual non-superconducting $\gamma_{res} = 0.36$ mJ/mol K^2, the superconducting contribution becomes $\gamma_s = 1.29$ mJ/mol K^2. This suggests that $\approx 22\%$ of the sample volume is non-superconducting.

We can now analyze the specific heat jump height at T_c. The jump ΔC at T_c is normalized as $\Delta C/\gamma T_c$, where γ is the Sommerfeld coefficient of the superconducting part. The superconducting transition can be broadened and the jump height suppressed in real materials due to a distribution of T_c arising from sample inhomogeneities or disorder. To get a better estimate of ΔC and T_c we use an entropy-conserving construction. In such a construction the C_{el} data just below the maximum of the anomaly is fit by a polynomial and extrapolated to higher temperatures. The entropy is then evaluated and equated to the normal state entropy $\gamma_n T_c$. Such a construction gave the jump height $\Delta C/T_c = 3.07 - 1.65 = 1.42$ mJ/mol K^2 and $T_c = 1.46$ K as shown in the Fig. 3.5 (b). The T_c found by this entropy-conserving construction is quite close to the onset temperature 1.5 K indicating the sharp transition and suggesting a very good sample quality with very little disorder and inhomogeneities. Using the above $\Delta C/T_c = 1.42$ mJ/mol K^2 and the superconducting contribution $\gamma_s = 1.29$ mJ/mol K^2 we estimate $\Delta C/\gamma_s T_c = 1.44/1.29 \approx 1.12$. This value is much smaller than the value 1.43 expected for a single-gap s-wave superconductor. The reduced value of $\Delta C/\gamma T_c$ is similar to observations for MgB_2 [83] and OsB_2 [54, 64] and suggests multi-gap superconductivity.

To confirm this possibility we have attempted to fit our $C_{el}(T)$ data below T_c to a phenomenological two-gap model as has been reported for example for MgB_2 [91]. The $T = 0$ value of the two superconducting gaps Δ_1 and Δ_2, the critical temperature

T_c, and the fractional contribution of the first band x were the three fit parameters. An excellent fit, shown in Fig. 3.5 (c) as the solid curve through the C_{el}/T data below T_c, was obtained with the fit parameters $\Delta_1/k_BT_c \approx 1.88$, $\Delta_2/k_BT_c \approx 1.13$, $T_c \approx 1.47$ K, and $x = 0.58$. If we compare the values of the two gaps we estimate above to the single band BCS value $\Delta/k_BT_c = 1.76$ we see that our values agree with the theorem that for a two-gap superconductor one of the gaps will always be larger than the BCS value while the second gap will always be smaller [92]. For comparison, we also show in Fig. 3.5 (c) the simulated data for superconductor with a single BCS gap with $T_c = 1.47$ K which clearly doesn't match the data. Thus, the heat capacity data in Fig. 3.5 strongly indicate that RuB_2 could be a two-gap superconductor.

Figure 3.6 (a) shows the specific heat C versus T data for RuB_2 measured between $T = 85$ mK and 3.5 K at various applied magnetic fields H. All data were measured by cooling in zero field to the lowest temperature and then measuring while warming up in the desired magnetic field. As expected, the SC transition is pushed to lower temperatures in increasing fields and is not observed down to the lowest temperature for fields $H \geq 250$ Oe. The specific heat divided by temperature C/T versus T at various magnetic fields is plotted in Fig. 3.6 (b). From Fig. 3.6 (b) we observe that the magnitude of the peak at T_c initially increases in a magnetic field. In a magnetic field the transition for a Type-I superconductor becomes first-order. Thus, one should in principle observe a diverging anomaly at T_c. In real materials however, the anomaly is broadened due to sample inhomogeneity and as a consequence the anomaly looks like a jump larger than that in zero field. Thus the observed behaviour in Fig. 3.6 (b) also points to Type-I superconductivity in RuB_2. This is similar to what was observed for OsB_2[64] and for other Type-I superconductors like $ScGa_3$ and $LaGa_3$ [93, 94] and $YbSb_2$ [95]. This is consistent with the magnetization data of Fig. 3.4 (b) inset which also suggest Type-I superconductivity.

The above value of γ can be used to estimate the density of states at the Fermi energy (ε_F) for both spin directions $N(\varepsilon_F)$ by using the expression $\gamma = \frac{\pi^2}{6}k_B^2N(\varepsilon_F)$. Using $\gamma = 1.65$ mJ/mol K^2 we obtain $N(\varepsilon_F) \approx 1.40$ states/eV f.u. We will compare this value with estimations from band structure calculations later.

3.4.4 Superconducting Parameters

The $C(T,H)$ data presented above were used to extract the critical temperature at various magnetic fields. The critical field H_c versus T data thus obtained is

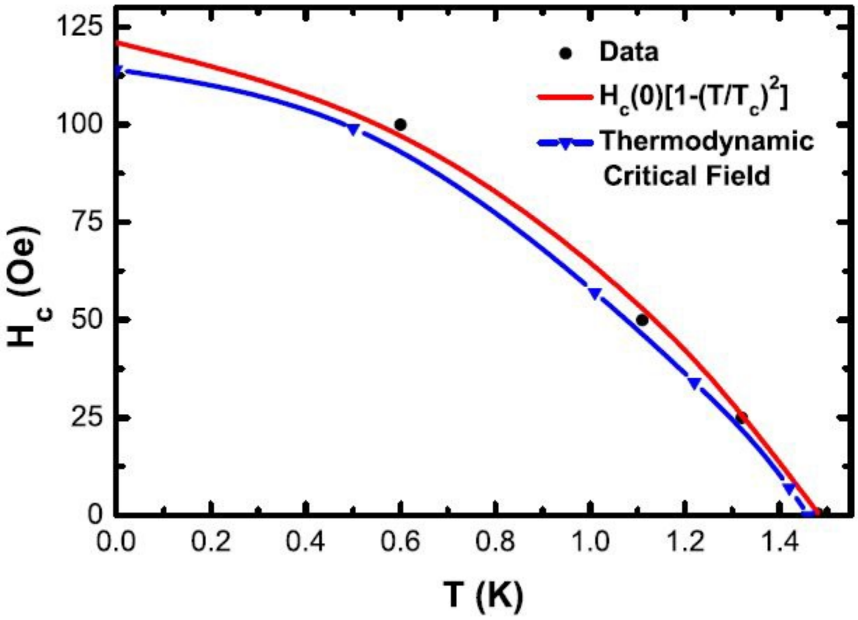

Figure 3.7: The critical field H_C versus T data extracted from the heat capacity C versus temperature T at various H. The solid curve through the data is a fit to the phenomenological BCS expression. The thermodynamic critical field $H_{tc}(T)$ obtained from the $C(T)$ data is also plotted for comparison. The solid curve through $H_{tc}(T)$ data is a guide to the eye (see text for details).

shown in Fig. 3.7. The data were fit by the phenomenological expression $H_c(T) = H_c(0)[1-(\frac{T}{T_c})^2]$ with $H_c(0)$ and T_c as fitting parameters, where $H_c(0)$ is the zero temperature critical field. The fit, shown as the solid curve through the data in Fig. 3.7, extrapolated to $T = 0$ gave the values $H_c(0) = 122$ Oe and $T_c = 1.48$ K. The excellent fit to the above expression suggests BCS superconductivity in RuB$_2$.

An estimate for the T dependent thermodynamic critical field $H_{tc}(T)$ can be made from the electronic heat capacity data obtained $C_{el}(T)$ using the expression $[\mu_0 H_{tc}(T)]^2/2 = F_{en} - F_{es} = -\gamma\left(T^2 + T_c^2\right)/2 + \int_T^{T_c} C_{el}(T)dT + T\int_0^T \frac{C_{el}(T)}{T}dT$, where F_{en} and F_{es} are the electronic free energies in the normal and superconducting state, respectively [22]. In particular, the $T = 0$ thermodynamic critical field $H_{tc}(0)$ can be estimated by inserting $T = 0$ in the above expression giving $(\mu_0 H_{tc}(0))^2/2 = -\gamma T_c^2/2 + \int_0^{T_c} C_{el}(T)dT$. Using $\gamma_s = 1.3$ mJ/mol K^2 and $T_c = 1.46$ K obtained from an equal entropy construction above, we estimate the $T = 0$ thermodynamic critical field $H_{tc}(0) \approx 114$ Oe. This is slightly smaller but close to the estimate 122 Oe made from the $H-T$ phase diagram and suggest type- I superconductivity in RuB$_2$. This is supported by estimates of the Ginzburg Landau parameter below. For comparison with the experimental $H-T$ diagram obtained from $C(T,H)$ data, the $H_{tc}(T)$ estimated by using the above expression are also shown in Fig. 3.7.

The electron-phonon coupling λ_{ep} can be estimated using McMillan's formula [37], which relates the superconducting transition temperature T_c to λ_{ep}, the Debye temperature θ_D, and the Coulomb pseudopotential μ^*. This formula can be inverted to get λ_{ep} in terms of the other parameters,

$$\lambda_{\text{ep}} = \frac{1.04 + \mu^* \ln(\frac{\theta_D}{1.45T_c})}{(1 - 0.62\mu^*)\ln(\frac{\theta_D}{1.45T_c}) - 1.04} \quad .$$

Using, $\theta_D = 700$ K obtained from heat capacity measurements above and using $T_c = 1.5$ K, we get $\lambda_{\text{ep}} = 0.37$ and 0.45 for $\mu^* = 0.1$ and 0.15, respectively. These values are slightly smaller than values obtained for OsB_2 [54] consistent with a slightly smaller T_c compared to OsB_2. These values of λ_{ep} are consistent with previous theoretical values [96] and suggest moderate-coupling superconductivity in RuB_2. The corresponding value for MgB_2 is $\lambda_{\text{ep}} \approx 1$ [97].

We now estimate the $T = 0$ values of the penetration depth $\lambda(0)$ and coherence length $\xi(0)$. RuB_2 has 2 formulae units per unit cell. This means that there are 4 electrons in one unit cell volume $V = 53.84$ Å^3. Therefore, the electron density is $n = 4/V = 7.4 \times 10^{-2}$ Å^{-3}. Assuming a spherical Fermi surface, we can use the above value of n to estimate the Fermi wave-vector $k_F = (3n\pi^2)^{1/3} = 1.3$ Å^{-1}. The London penetration depth is given by $\lambda(0) = (m^*/\mu_0 ne^2)^{1/2}$, where we take the effective mass m^* as the free electron mass m_e. Putting in values gives us $\lambda(0) \approx 47$ nm. The BCS coherence length can be estimated using the expression $\xi = \frac{0.18\hbar^2 k_F}{k_B T_c m^*} \approx 0.45$ μm. The Ginzburg Landau (GL) parameter can now be estimated as $\kappa = \lambda(0)/\xi \approx 0.1$ which is much smaller than the value $1/\sqrt{2} \approx 0.707$ separating Type-I and Type-II superconductivity. The above value of κ suggests that RuB_2 is an extreme Type-I superconductor. This is consistent with the low H_c and the $M(H_{\text{eff}})$ data presented above. The mean free path l can be estimated using the expression $l = v_F \tau$, where the Fermi velocity is $v_F = \hbar k_F/m^*$ and the scattering time is given by the expression for the Drude conductivity $\tau = m^*/ne^2\rho$. Using $m^* = m_e$ and the residual resistivity value $\rho(1.6\text{ K}) = 1.1$ $\mu\Omega$ cm, we estimate $l \approx 72$ nm. From the above estimates of ξ and l we conclude that $\xi >> l$, making RuB_2 a dirty limit superconductor. For a dirty limit superconductor we can make another estimate of the GL parameter as $\kappa = 0.75\lambda(0)/l \approx 0.66 < 0.707$, again consistent with Type-I behavior. We add that the estimation of the mean free path l is often affected by grain boundary scatterings, which can cause an underestimation of l. Thus the evaluated $\kappa \approx 0.66$ is an upper limit making our inference of type-I

Table 3.1: Lattice parameters obtained from relaxing the experimental unit cell of RuB_2

Lattice Parameters(Å)	Experimental	Calculated	%Error
a	4.644795	4.66487	0.43
b	2.865153	2.89674	1.1
c	4.045606	4.05224	0.16

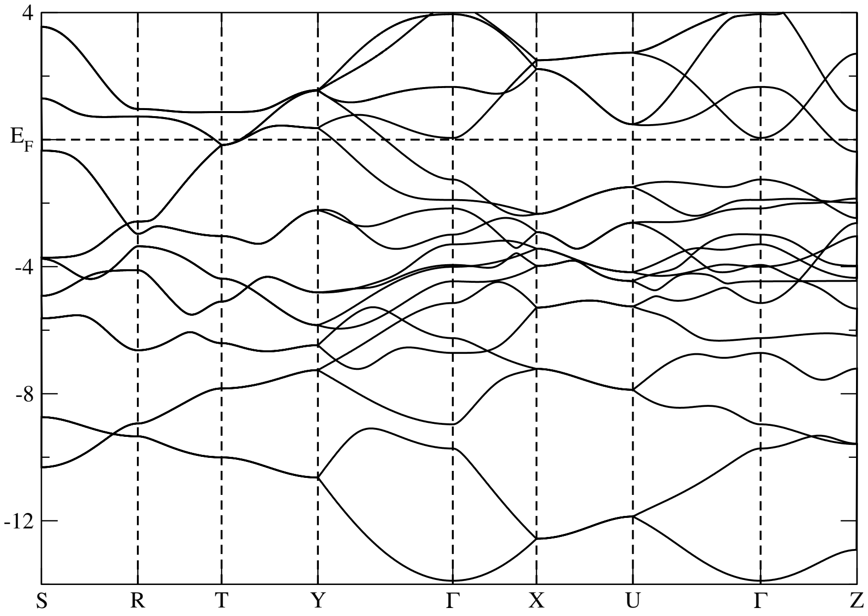

Figure 3.8: The calculated electronic band structure of orthorhombic RuB_2 along high symmetric points. E_F represents the Fermi level, which is set at 0 eV.

superconductivity even stronger.

3.4.5 Band Structure and Fermi Surface

RuB_2 crystallises in the orthorhombic crystal system, space group *Pmmn* (no. 59). Each unit cell contains two formula units (two Ru atoms and four B atoms). The ionic and lattice relaxation were performed to optimize the crystal structure by using variable cell relaxation. We have used an energy cutoff of 55 Ry for the plane wave basis. The Brillouin zone integration is conducted with a $11 \times 18 \times 13$ Monkhorst-pack grid for the K-point sampling. In the optimized crystal structure, the forces on all the atoms are less than 10^{-4} Ry/au. The calculated lattice parameters of optimized RuB_2 compound along with the experimental values are tabulated in Table 3.1. The calculated lattice parameters are within 1% of the experimental values [54].

The electronic band structure of RuB_2 is shown in Fig. 3.8. It can be seen that several energy bands are crossing the Fermi level E_F confirming that RuB_2 is a

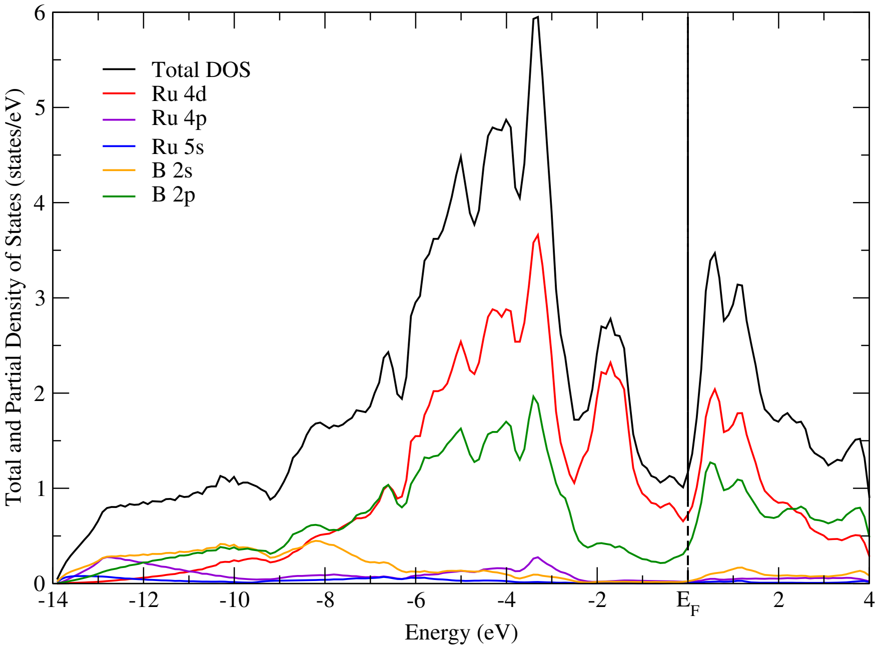

Figure 3.9: Calculated total density of states (DOS) and partial density of states (PDOS) for RuB_2. E_F, represents the Fermi energy and is set at 0 eV.

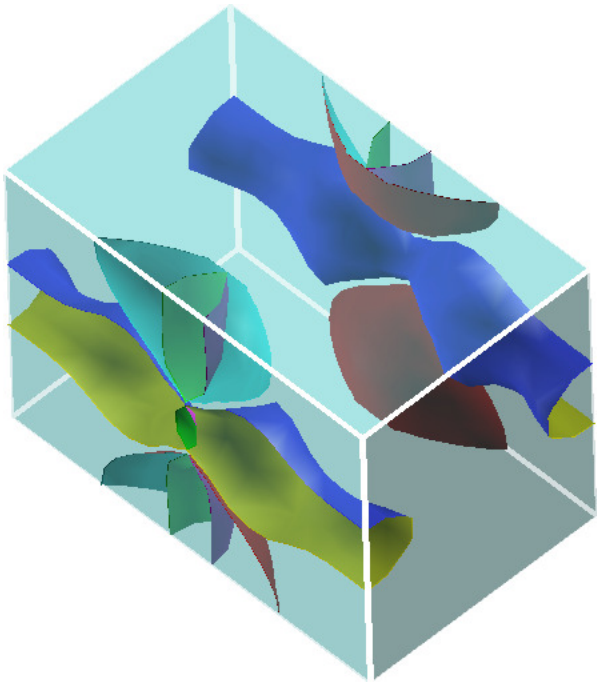

Figure 3.10: The merged Fermi surface (FS) for RuB_2 consisting of 4 different sheets. The parallelepiped is in the first Brillouin zone.

metal. Figure 3.9 shows the total and partial density of states (DOS) in units of states/eV showing the contribution of individual elements and orbitals to the DOS at various energies measured from the Fermi energy E_F. From Fig. 3.9 it can be seen that the $4d$-orbital of Ru and the $2p$-orbital of B make the main contributions to the density of states in the vicinity of the Fermi level. The total DOS at ε_F is found to be $N(\varepsilon_F) = 1.15$ states/eV f.u. for both spin directions. This value is slightly smaller than the value $N(\varepsilon_F) = 1.40$ states/eV f.u. estimated from experimental value of γ. An estimate for the electron-phonon coupling constant λ_{ep} can be made using the following relation:
$N(\varepsilon_F)$ from heat capacity $= (N(\varepsilon_F)$ from band structure $)(1+\lambda_{ep})$.
A comparison of the above experimental and theoretical values of $N(\varepsilon_F)$ gives $\lambda_{ep} \approx 0.22$ which is close but slightly smaller than the values obtained above using McMillan's formula.

We have also obtained the Fermi surface for RuB_2. The merged Fermi surface within the first Brillouin zone is shown in Fig. 3.10. The Fermi surface consists of 4 FS sheets: one quasi-two-dimensional tubular sheet and two nested ellipsoidal sheets very similar to OsB_2 [87]. An additional small 4th sheet nested inside the tubular sheet is also found for RuB_2.

3.5 Conclusion

High-pressure measurements of OsB_2 indicate that the mechanism of superconductivity in this family of compounds is electron-phonon mediated . Using electrical resistivity $\rho(T)$, magnetic susceptibility $\chi(T)$, magnetization $M(H)$, and specific heat $C(T,H)$ data we have confirmed bulk superconductivity in RuB_2 with a superconducting critical temperature $T_c = 1.5$ K. The $T = 0$ critical field is estimated to be $H_c(0) = 122$ Oe. The magnitude of the anomaly in specific heat at T_c in zero field is observed to be $\Delta C/\gamma_s T_c \approx 1.1$, which is much smaller than the value 1.43 expected for a single-gap BCS superconductor. This observation is similar to what has previously been observed for MgB_2 and OsB_2, and suggests multi-gap superconductivity in RuB_2. This is confirmed by the excellent fitting of the electronic specific heat below T_c to a two-gap model with the value of the two gaps estimated as $\Delta_1/k_BT_c \approx 1.88$ and $\Delta_2/k_BT_c \approx 1.13$. The scanning tunneling spectra measured in collaboration with Soumya Datta et al. [98] also confirm the existence of two superconducting gaps on different grains of Polycrystalline RuB_2. Their temperature-dependent tunneling spectra measurements showed that the gaps from different bands evolve with temperature in a different way [98]. The value of $\Delta C/\gamma T_c$ in a magnetic field becomes larger than its zero field value strongly indicating Type-I behaviour. This is also similar to what was observed earlier for OsB_2 and also for other candidate Type-I superconductors like $ScGa_3$ and $LaGa_3$ [93] and $YbSb_2$ [95]. The $M(H_{eff})$ behaviour are also consistent with Type-I superconductivity. This is confirmed by estimates of the Ginzburg-Landau parameter κ which comes out to be $\kappa \approx 0.1$–$0.6 < 0.707$. For comparison of the superconducting state properties of OsB_2 and RuB_2, the various superconducting parameters of these compounds are summarized here in Table 3.2.

Table 3.2: Comparison of superconducting properties of OsB_2 and RuB_2.

	superconducting parameters									
	T_c K	$H_c(0)$ Oe	λ_{ep}	ξ μm	l nm	$\lambda(0)$ nm	κ	$N(\varepsilon_F)$ states/eV f.u.	$\Delta C/\gamma T_c$	Δ_1/k_BT_c, Δ_2/k_BT_c
OsB_2	2.1	153	0.5-1	0.133	137	300	1-3	0.55	1.3	1.25, 1.90
RuB_2	1.5	122	0.37-0.45	0.45	72	47	0.1-0.6	1.40	1.1	1.88, 1.33

These results strongly suggest that RuB_2 is a rare alloy Type-I superconductor and may be the first multi-gap Type-I superconductor. We note that both $YbSb_2$ ($\kappa \approx 0.05$ and $\Delta C/\gamma T_c <$ BCS) [95] and boron-doped SiC ($\kappa \approx 0.35$ and $\Delta C/\gamma T_c <$ BCS) [99] have been reported as Type-I superconductors and have specific heat anomalies smaller than expected for single band BCS superconductivity. However, both reported materials were multi-phase samples and in $YbSb_2$, an additional superconducting phase with a lower T_c than the bulk T_c was also observed, making it complicated to estimate intrinsic superconducting parameters. Thus RuB_2 seems to be the best candidate for two-gap Type-I superconductivity so far.

However, a scenario (anisotropic Type-I superconductivity) like the one recently suggested for OsB_2 [65] could also be at play in RuB_2 and future work like imaging of magnetic flux entering the material may be useful to confirm the type of superconductivity in RuB_2.

CHAPTER 4

Superconducting properties of the rare-earth ternary boride compounds $RRuB_2$ (R = Lu, Y)

4.1 Introduction

The rare-earth earth (R) ternary boride compounds have gained significant attention because of their superconducting and magnetic properties. After discovering superconductivity in the rare-earth rhodium borides compounds like RRh_3B_2 and RRh_4B_4 [100, 101], a considerable amount of experimental and theoretical study on ternary boride superconductors has been conducted with the main emphasis on the interplay between superconductivity and long-range magnetic order [102]. In these materials, the superconducting transition temperature T_c has been found to be relatively high [66]. In all crystal structures of RT_4B_4 (T is a transition metal) compounds, the boron atoms are found to have dimerized into non-interacting B_2 units. In the tetragonal structure of RT_4B_4, the T- atoms form linear or zig-zag chains, whereas, in the orthorhombic structure of these compounds, T atoms are arranged in a three-dimensional cluster that is interpenetrated [103, 101]. Across the entire range of rare-earth elements; tetragonal polytype compounds have higher T_c values than orthorhombic compounds, which shows that the dimensionality of the T clusters may have a significant role in the superconductivity [104].

Another transition metal ternary boride family MTB_2 (M = Sc, Y, Lu and T= Ru, Os) compounds has been found to crystallize in an orthorhombic $LuRuB_2$-type

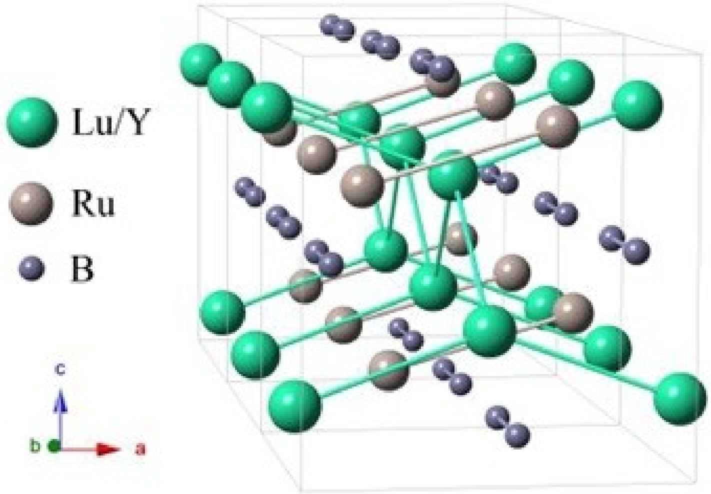

Figure 4.1: Crystal structure of $RRuB_2$ (R = Lu, Y)(Reprinted from **PhysRevB.97.094506**)[1]

structure with space group Pnma and shows transition to the superconducting state [67, 105]. The key features of $LuRuB_2$-type structure are the absence of transition metal clusters, the long distance between Ru atoms and short Lu-Lu interplanner distance. Similar to the RT_4B_4 compounds, boron dimers also appear in this structure and rare-earth atoms are arranged to form zig-zag chains. The boron dimers interact weakly, making straight chains that are perpendicular to the planes of R and T atoms and run parallel to the main R-R zig-zag chains (Fig. 4.1). These structural similarities with RRh_4B_4 suggests that similar high T_cs could be acheived in $RRuB_2$.

The rare-earth ternary borides $RRuB_2$ (with R = Y, Lu) compounds with $LuRuB_2$-type structure have been reported to show superconductivity below T_c = 7.7 and 10.6 K, respectively [67, 68], are significant as reference materials for ternary rare-earth borides with the same crystal structure, because the 4f electron shell is empty in the Y compound and is completely filled in the Lu compound. The high T_c values in these compounds are comparable to the strong coupling superconductors V_3Si (A15 compound) and HfV_2 (C15 Laves-phase compound) [106, 107]. The previous reported estimated values of upper critical field $H_{c2}(0)$ are quite large in these compounds (4.8 T for $YRuB_2$ and 5.7 T for $LuRuB_2$) [67, 68]. These large T_c and $H_{c2}(0)$ values suggest strong electron-phonon coupling in these compounds, with a high superconducting carrier density. However, the μSR (the muon-spin rotation and relaxation) and NMR measurements on these compounds indicate the conventional s-wave superconductivity which can be described within the BCS weak-coupling limit [1, 108]. Both these compounds appear in the same region in the

Uemura plots as borocarbide and rare-earth hexaborides superconductors [1, 109], indicating that the superconductivity in these materials may not be entirely conventional. Additionally, the heat capacity measurements on these compounds show reduced heat capacity anomaly at T_c compared to weak-coupling BCS predictions [110]. Thus there are contrasting reports about the nature of superconductivity in $RRuB_2$ materials.

In this chapter, we will present our investigation on superconducting properties of rare-earth ternary borides $RRuB_2$ (with R = Y, Lu) compounds. The electrical resistivity ρ versus temperature T measurements on these samples in various magnetic fields is performed. The linear trend of upper critical field $H_{c2}(T)$ curve for both the samples suggests unconventional superconducting behavior. For $LuRuB_2$, point contact spectroscopy measurements show the non-BCS temperature dependence of the superconducting gap, which again is a signature of unconventional behavior. We have obtained various superconducting parameters for both the samples using the upper critical field H_{c2} versus temperature T data. On the application of pressure P, suppression in T_c of $LuRuB_2$ is observed, which indicates electron-phonon mediated superconductivity in this family of compounds.

4.2 Experimental Details

Polycrystalline $LuRuB_2$ and $YRuB_2$ samples were prepared by arc melting. First, we have taken Ru powder (99.99%, Sigma Aldrich) and B chunks (99.999%, Alfa Aesar) in stoichiometric ratios and arc melted to form RuB_2 ingot. Then appropriate amount of Lu (or Y) (99.95%, Alfa Aesar) ingot and RuB_2 was arc melted to form $LuRuB_2$ (or $YRuB_2$) sample. All this arc melting was done on a water-cooled copper hearth in a high-purity argon environment with a Ti button acting as an oxygen getter. The samples were flipped and remelted several times (11-12 times) to ensure good homogeneity. Finally, the samples were sealed in evacuated quartz tubes and annealed for 12 days at 1050^0C. Powdered x-ray data showed that the majority of the sample crysttelize in the $LuRuB_2$ structure with small ($\approx 10\%$) amount of non-superconducting impurity phases.

The electrical transport measurements from 2 K to 305 K were done on an annealed sample of $LuRuB_2$ using a commercial Quantum Design Physical Properties Measurements System(QD-PPMS). The heat capacity C data ranged from 2 K to 12 K was collected using a Quantum Design PPMS. The magnetization M versus temperature T data were measured from 7 K to 12 K by applying different pressures

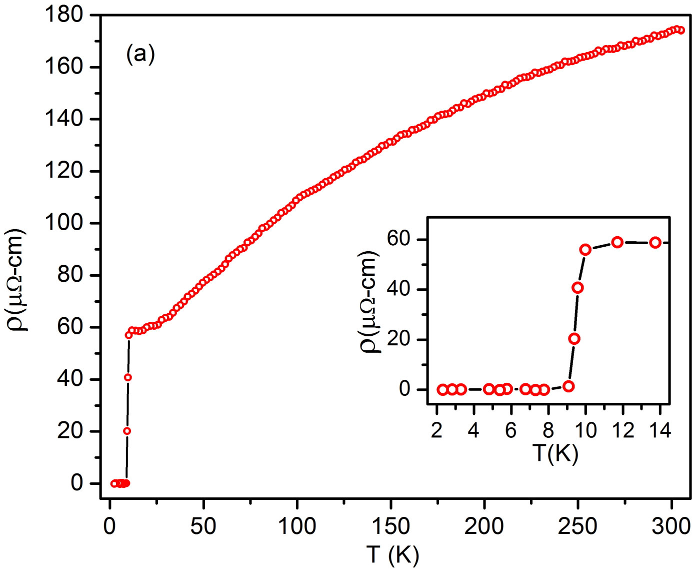

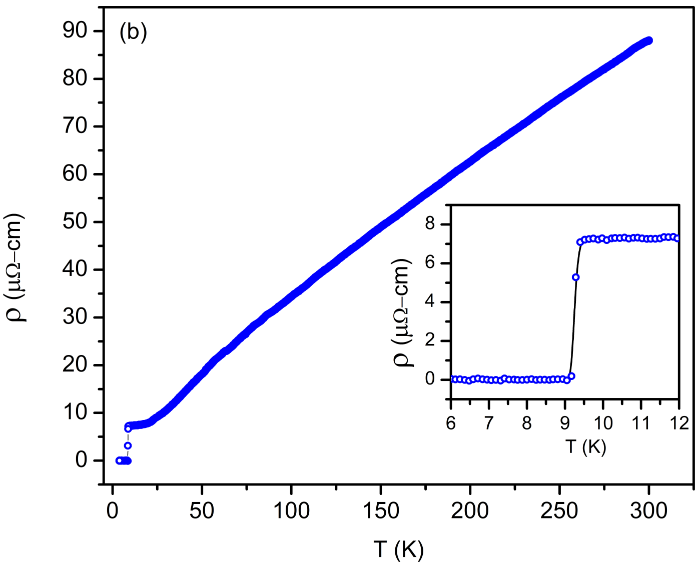

Figure 4.2: (a) The electrical resistivity ρ versus temperature T for LuRuB$_2$ measured in zero magnetic field between $T = 2$–305 K. The inset shows the data below $T = 25$ K to highlight the abrupt drop at $T_c = 9.4$ K signalling the transition to the superconducting state. (b) The electrical resistivity ρ versus temperature T for YRuB$_2$ measured in zero magnetic field between $T = 2$–300 K. The inset shows the data below $T = 12$ K to highlight the abrupt drop at $T_c = 9.2$ K signalling the transition to the superconducting state.

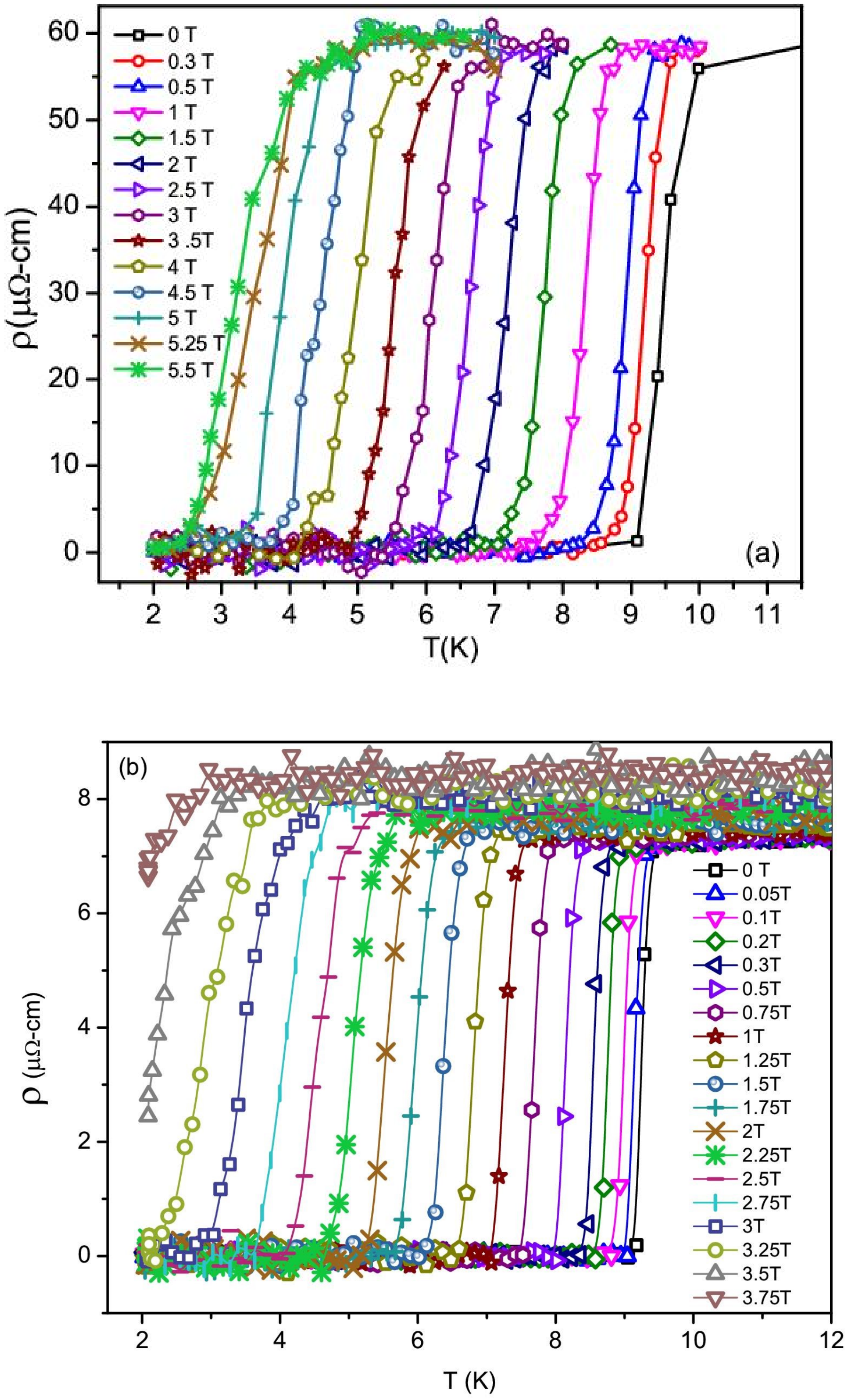

Figure 4.3: (a) The resistivity ρ(T) of $LuRuB_2$ between 12 and 2 K measured with various applied magnetic fields. (b) The resistivity ρ(T) of $YRuB_2$ between 12 and 2 K measured with various applied magnetic fields

using a Cu-Be pressure cell with the VSM option of a Quantum Design PPMS. The point-contact spectroscopy measurements at low temperatures were carried out on a $LuRuB_2$ sample in a liquid helium-based cryostat using sharp tips of pure palladium (Pd) to create a metallic point-contact on the sample. The electrical transport measurements from 2 K to 300 K were performed on an annealed sample of $YRuB_2$ using a commercial PPMS from Cryogenics Limited.

4.3 Electrical Resistivity

The electrical resistivity ρ as a function of temperature T for $LuRuB_2$ from 305 K to 2 K is shown in Fig. 4.2 (a). The negative curvature of the resistivity curve has been observed, which is similar to high-T_c A-15 compounds and is in agreement with previously reported results [110, 68]. The resistivity at T= 305 K is ρ(305K) $\approx$ 168 $\mu\Omega$cm and residual resistivity is $\rho_0(10\text{ K}) \approx 57$ $\mu\Omega$cm, which gives residual resistivity ratio RRR $\approx$ 3. In the inset of Fig. 4.2 (a), we can see resistivity starts dropping abruptly below T $\approx$ 9.9 K and disappear by T$\approx$ 9.1K, giving a transition width $\Delta T \approx$ 800 mK. The superconducting transition temperature T_c is defined by the temperature at the half-height of the normal to the superconducting state transition and is found to be $T_c \approx$ 9.45 K.

Figure 4.2 (b) shows ρ as a function of T for $YRuB_2$ from 300 K to 2 K. At T = 300 K, the resistivity is ρ(300K) $\approx$ 88 $\mu\Omega$cm, and the residual resistivity is $\rho_0(9.5\text{ K}) \approx 7.3$ $\mu\Omega$cm, giving a residual resistivity ratio RRR $\approx$ 12. The $\rho(T)$ data below $T = 12$ K is shown inset in Fig. 4.2 (b) to illustrate the abrupt drop to zero resistance below $T_c = 9.2$ K, confirming the onset of superconductivity in $YRuB_2$. The observed transition temperature T_c value for $YRuB_2$ is slightly higher than the previously reported [68]. The small superconducting transition width $\Delta T \approx 40$ mK, implies a very sharp transition compared to that in $LuRuB_2$. A larger RRR value and a sharp transition reflect the good quality of the $YRuB_2$ sample.

The ρ vs T data measured between $T = 2$ K and 12 K at varied applied magnetic fields H, for $LuRuB_2$ and $YRuB_2$ samples are shown in Fig. 4.3 (a) and Fig. 4.3 (b) respectively. All data were collected by cooling in zero fields to a superconducting state and then measuring while heating up in the desired field. As expected, the superconducting transition temperature in both materials is pushed to lower temperature with increasing field. In $LuRuB_2$, the superconducting transition occurred at $T_c \approx$ 3.2 K when we apply a magnetic field of 5.5 T. In the $YRuB_2$ sample, the superconducting transition occurred at $T_c \approx$ 2.9 K when we apply a magnetic field of 3.25 T. The onset T$_c$ at various magnetic fields H was extracted from these data in Fig. 4.3, and an H–T phase diagram was drawn for both the samples. These data are plotted in Fig. 4.4. We will discuss these data in the next section.

4.4 The Upper Critical Field Measurements and Superconducting Parameters

The upper critical field H$_{c2}$(T) for LuRuB$_2$ was determined using the ρ(T) data in Fig. 4.3(a) for magnetic fields up to H = 55 kOe. For YRuB$_2$ sample, the ρ(T) data in Fig. 4.3(b) for magnetic fields up to H = 40 kOe were used to extract the upper critical field H$_{c2}$(T). The results of the upper critical field H$_{c2}$ as a function of temperature T for annealed samples of LuRuB$_2$ and YRuB$_2$ are shown in Fig. 4.4(a) and Fig. 4.4(b), respectively. An unusual near linear H-T diagram is observed for both materials.

We now make estimates of several superconducting parameters for LuRuB$_2$ and YRuB$_2$. We have used the dirty limit Werthamer-Helfand-Hohenberg (WHH) formula [111] to analyze the critical field data for LuRuB$_2$ compound. The upper critical field H_{c2} at zero temperature is calculated using the weak coupling formula $H_{c2}(0) = 0.693\,(-dH_{c2}/dT)_{T_c}T_c$, where $(dH_{c2}/dT)_{T_c}$ can be find out from the slope of the H_{c2}(T) curve near T$_c$ [112, 113, 114]. In Fig. 4.3(a), the linear fit of data near T$_c$ gives the slope $(dH_{c2}/dT)_{T_c}$= -8.9 kOe/K. This will give $H_{c2}(0)$ = 58.6 kOe, which is nearly same as reported previously [68].

The coefficient of electronic specific heat γ can be estimated using the relation $H_{c2}(0) = 3.06 \times 10^4 \rho_0\, \gamma T_c$, where units of γ are in erg/ cm^3 K^2,H_c in Oe, and ρ_0 in Ωcm [112]. From ρ(T) data the residual resistivity $\rho_0 \approx 57\ \mu\Omega$ cm, this gives $\gamma = 3.56 \times 10^3$ erg/ cm^3 K^2. Using this value of γ in relation $\kappa = 7.49 \times 10^3 \gamma^{1/2}\rho_0$ [115], the value of Ginzburg-Landau parameter is found to be $\kappa \approx 25$. This puts LuRuB$_2$ in the Type-II superconducting regime. The relation $H_c(0) = 4.23\gamma^{1/2}T_c$ [115] gives the thermodynamic critical field $H_c(0) \approx$ 2.4 kOe. From the GL theory the lower critical field $H_{c1}(0)$ is given by the relation [115]:

$$H_{c1}(0) = H_c(0)\ln\kappa/\sqrt{2}\kappa$$

This gives $H_{c1}(0) \approx 0.22$ kOe.

Another estimate of $H_{c2}(0)$ can be obtained by fitting the $H_{c2}(T)$ data using the empirical power law expression $H_{c2}(T) = H_{c2}(0)\left[1-\left(\frac{T}{T_c}\right)^{\alpha}\right]$ with α and $H_{c2}(0)$

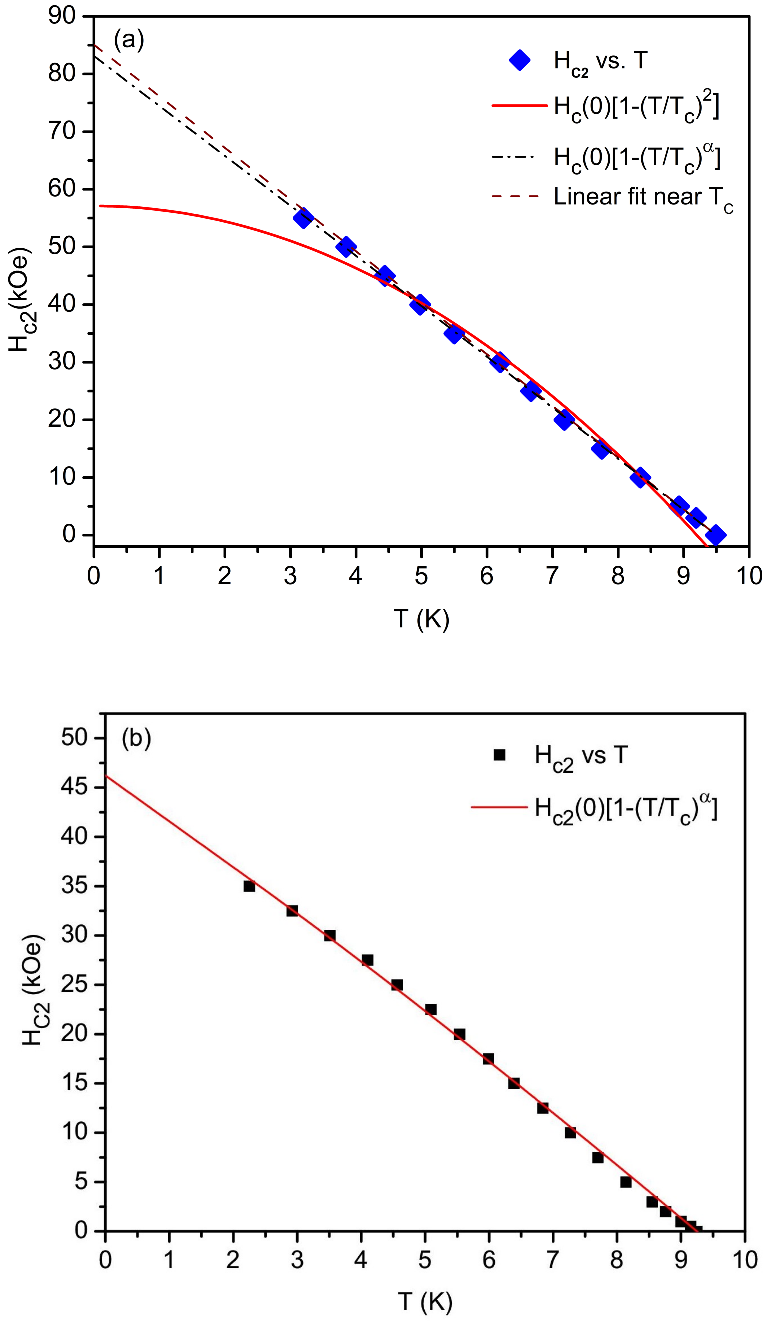

Figure 4.4: (a) Upper critical magnetic field H$_{c2}$ versus temperature T diagram for LuRuB$_2$ sample extracted from three different types of measurements as indicated. The curves through the data are fits to different models (see text for details) The dashed curve is a fit by the expression $H_{c2}(T) = H_{c2}(0)\left[1-\left(\frac{T}{T_c}\right)^{\alpha}\right]$. (b) Upper critical magnetic field H$_{c2}$ versus temperature T for YRuB$_2$ sample, extracted from ρ(T) measurements. The solid curve is a fit by the expression $H_{c2}(T) = H_{c2}(0)\left[1-\left(\frac{T}{T_c}\right)^{\alpha}\right]$

as fitting parameters and with fixed value of $T_c = 9.5$ K. In Fig. 4.3(a), the fit is shown as the dashed brown line curve. From fitting we obtain $H_{c2}(0) = 82.4$ kOe and $\alpha = 1.03$. This estimate of $H_{c2}(0)$ is much higher than the value of 58.6 kOe obtained above using the WHH formula.

The mean free path 'l' can be calculated using resistivity data and relation: $l = 1.27 \times 10^4 \left[\rho_0 n^{2/3} \left(S/S_f\right)\right]^{-1}$, where n is the density of conduction electrons in units of cm^{-3} and S/S_f is the ratio of the area of the Fermi surface to that of a free-electron gas. Both $YRuB_2$ and $LuRuB_2$ has four formula units (f.u.) per unit cell. This means that there are four electrons in one unit cell volume. For $LuRuB_2$, the unit cell volume is $V \approx 190$ Å^3 and for $YRuB_2$, $V \approx 199$ Å^3 [105]. Therefore, the electron density is $n = 4/V = 2.10 \times 10^{-2}$ Å^{-3} in $LuRuB_2$ sample and 2.01×10^{-2} Å^{-3} in $YRuB_2$. Assuming a spherical Fermi surface, i.e., $S/S_f = 1$ and using above value of n in expression of l gives l = 29.3 Å for $LuRuB_2$. For $YRuB_2$, the mean free path is found to be l = 235 Å . The Fermi wave vector can be estimated using the relation $k_F = \left(3n\pi^2\right)^{1/3}$. For $LuRuB_2$, we have found $k_F = 0.85$ Å^{-1} and for $YRuB_2$, $k_F = 0.84$ Å^{-1}. The BCS coherence length is estimated using the BCS expression $\xi = \frac{0.18\hbar^2 k_F}{k_B T_c m^*}$, where m^* is the effective mass of electron. For $LuRuB_2$, $m^* \approx 10m_e$, whereas for $YRuB_2$, $m^* \approx 15m_e$ [68, 1]. This gives $\xi \approx 212$ Å for $LuRuB_2$ and $\xi \approx 97$ Å for $YRuB_2$.

The above estimations of ξ and l for $LuRuB_2$ show that $\xi \gg l$, making $LuRuB_2$ a dirty limit superconductor.

For a type-II superconductor in the dirty limit, the superconducting coherence length ξ can also be estimated using the Ginzburg-Landau relation [22]:

$$H_{c2}(0) = \Phi_0/4.54\xi(0)l$$

where $\phi_0 = hc/2e = 2.068 \times 10^{-7}$Oe cm^2 is a quantum of flux. Using $H_{c2}(T = 0) = 82.4$ kOe, we obtain $\xi(0) \approx 188$ Å .

For $YRuB_2$ sample, the above estimated values of ξ and l shows that $\xi_{\mathrm{BCS}}(0)/l_{\mathrm{tr}}$ is less than 1, making it a clean superconductor. For $YRuB_2$ sample, we have obtained $H_{c2}(0)$ by fitting the $H_{c2}(T)$ data in Fig. 4.3(b) using the expression $H_{c2}(T) = H_{c2}(0)\left[1 - \left(\frac{T}{T_c}\right)^{\alpha}\right]$ with α and $H_{c2}(0)$ as fitting parameters and fixed $T_c = 9.25$ K. From fitting, we obtain $H_{c2}(0) = 45.2$ kOe and $\alpha = 1.11$. The linear fit of data near T_c gives the slope $(dH_{c2}/dT)_{T_c}$= -4.2 kOe/K.

As the upper critical field is smaller than the Pauli paramagnetic limiting field $H_p = 18.6T_c$ (K Oe) [116], the spin effect can be ignored, and the $YRuB_2$ sample can be analyzed using clean limit results of Ginzburg-Landau theory [115]. These results are:

$$\begin{aligned} -(dH_{c2}/dT)_{T_c} &= 9.55 \times 10^{24} \gamma^2 T_c (n)^{-4/3}, \\ \xi(0) &= 7.95 \times 10^{-17} n^{2/3} (\gamma T_c)^{-1}, \\ H_{c2}(0) &= \Phi_0 / 2\pi \xi^2_{\mathrm{GL}}(0) \\ \text{and } \kappa &= 1.60 \times 10^{24} T_c \gamma^{3/2} n^{-4/3}; \end{aligned}$$

where $\xi_{\mathrm{GL}}(0) = 0.74\xi(0)$ is the GL coherence length at $T = 0$ K and the other quantities are same as previously defined. Using these relations for YRuB$_2$, we have obtained $\gamma = 5.09 \times 10^3$ erg/ cm^3 K^2, $\kappa = 9.8$, $\xi(0) \approx 124$ Å and $H_{c2}(0) = 39.1$ kOe.

The enhanced density of states at the Fermi energy can be find out using the relation:

$$N(\varepsilon_F) = \left(\pi^2 k_{\mathrm{B}}^2/3\right)^{-1} \gamma,$$

where $N(\varepsilon_F)$ is in states/ eV f.u. for each spin direction and γ is in units of mJ/mole K^2. For LuRuB$_2$, the value of γ found above is 3.56×10^3 erg/ cm^3 K^2. Using $z = 4$ (f.u/unit cell) and unit cell volume ≈190 Å^3 for LuRuB$_2$, the value of $\gamma = 10.2$ mJ/ mole K^2. Using this, the enhanced density of states for LuRuB$_2$ is N (ε_F) = 0.54 states/ eV atom-spin direction. Similar analysis for YRuB$_2$ has been done which yield N (ε_F) = 0.79 states/ eV atom-spin direction for YRuB$_2$.

4.5 Heat Capacity data for LuRuB$_2$

Fig. 4.6 shows the specific heat C versus T data for LuRuB$_2$ measured between $T = 2$ K and 12 K in the zero magnetic fields. A jump in heat capacity near $T_c = 9.4$ K in the $H = 0$ data is observed. As there are unknown impurity phases in the sample, it is impossible to extract superconducting parameters from C(T) data. However, the jump in the heat capacity data at T$_c$ confirms the bulk superconductivity in LuRuB$_2$.

4.5.1 Point Contact Spectra of LuRuB$_2$

Unconventional superconductivity in RRuB$_2$ was suggested from the nearly linear H-T phase diagram presented above. The unconventional character of superconductivity in LuRuB$_2$ are also visible in point-contact spectroscopy measurements. The spectrum in Fig. 4.6 (a) displays a symmetrical double-peak structure around

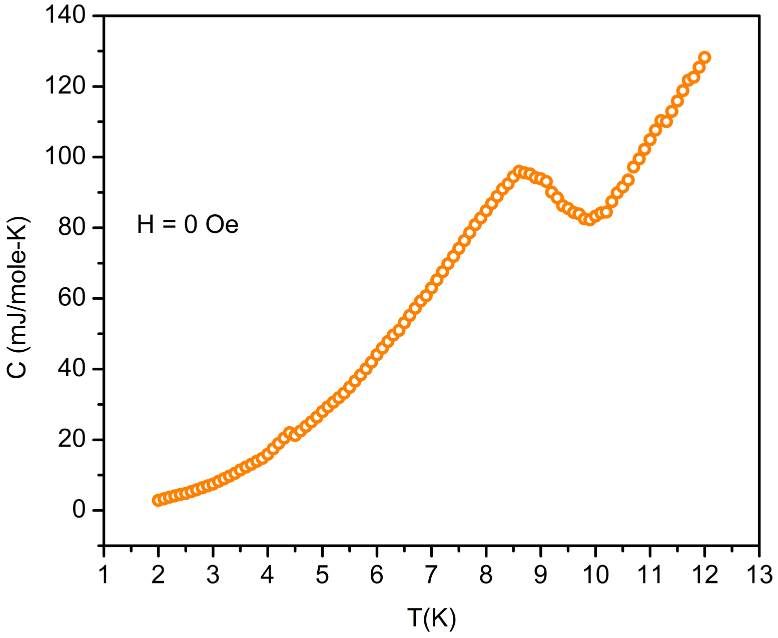

Figure 4.5: The specific heat C versus T data for LuRuB$_2$ measured between $T = 2$ K and 12 K in zero magnetic fields H.

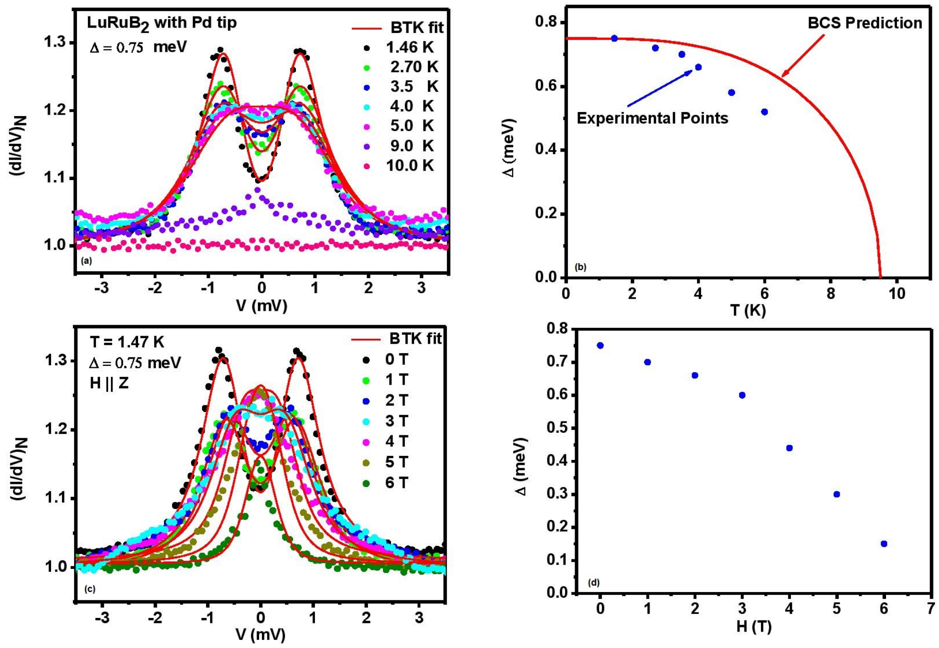

Figure 4.6: (a) The temperature dependence of point-contact spectra for LuRuB$_2$ with BTK fits (indicated by solid lines). The symmetrical double-peak structure in the spectrum is a feature of Andreev's reflection in NS point-contacts. (b) The temperature dependence of superconducting gap delta extracted from BTK analysis of the temperature-dependent spectra. The solid line shows the BCS prediction. (c) Magnetic field dependence of point-contact spectra of LuRuB$_2$. The solid lines show BTK fits. (d) The magnetic field dependence of superconducting gap $\Delta(T)$.

V = 0. Andreev reflection in ballistic normal metal-superconductor (NS) point-contacts is characterised by a double peak structure like this. The amplitude of the superconducting energy gap is estimated by the position of the peaks in such spectra. Based on the Blonder, Tinkham, and Klapwijk (BTK) theoretical model [78] , We have estimated the superconducting energy gap value of 0.75 meV for spectra obtained at 1.46 K. The behaviour of the superconducting energy gap as a function of temperature has been studied. For this, the PCAR spectra at various temperatures have been recorded and fitted using the BTK model. Fig. 4.6 (a) depicts the temperature-dependent spectra as dotted lines and solid lines show the BTK fitting. It is seen that the characteristics associated with Andreev reflection varies gradually with temperature and double-peak structure vanishes at 10 K. Though it can be seen in Fig. 4.6 (a) that spectra become flat at 10 K, a reasonable fitting is possible only up to 6 K. The Fig. 4.6 (b) depicts the temperature dependence of the superconducting energy gap Δ extracted from Fig. 4.6 (a). The temperature dependene of the superconducting gap deviates from the BCS prediction. With a T_c of 9.4 K, the estimated low-temperature gap magnitude is 0.75 meV, which gives $\Delta/k_BT_c\approx1$ which is smaller than the BCS weak coupling lower limit.

Fig. 4.6 (c) shows evolution of the superconducting energy gap in $LuRuB_2$ as a function of the magnetic field H, with solid lines showing respective BTK fits. At a field of around 6 Tesla, at which all double-peak features in the point contact spectra disappears. This gives an estimate of the upper critical field $H_{c2} \approx 6T$. The unusual Δ(T) dependence which deviates from BCS predictions and the small $\Delta/k_BT_c\approx1$ value suggest unconventional superconductivity, supporting conclusions from the H-T phase diagram.

4.6 Pressure Measurements on $LuRuB_2$ Superconductor

The findings of magnetization M versus temperature T data for $LuRuB_2$ measured between 8 K and 10 K at various applied pressures are shown in Figure 4.7 (a). A sharp drop in M at 0 GPa pressure indicates the superconducting transition, with a transition temperature of ≈ 8.8 K. As the pressure is increased, a noticeable shift in T_c to lower values can be seen. Sn was used as a manometer during these measurements. The pressure was calculated using the superconducting T_c for Sn (not shown) at various pressures. To reveal the superconductivity of $LuRuB_2$ over the background of the pressure cell, we had apply a magnetic field of H = 50

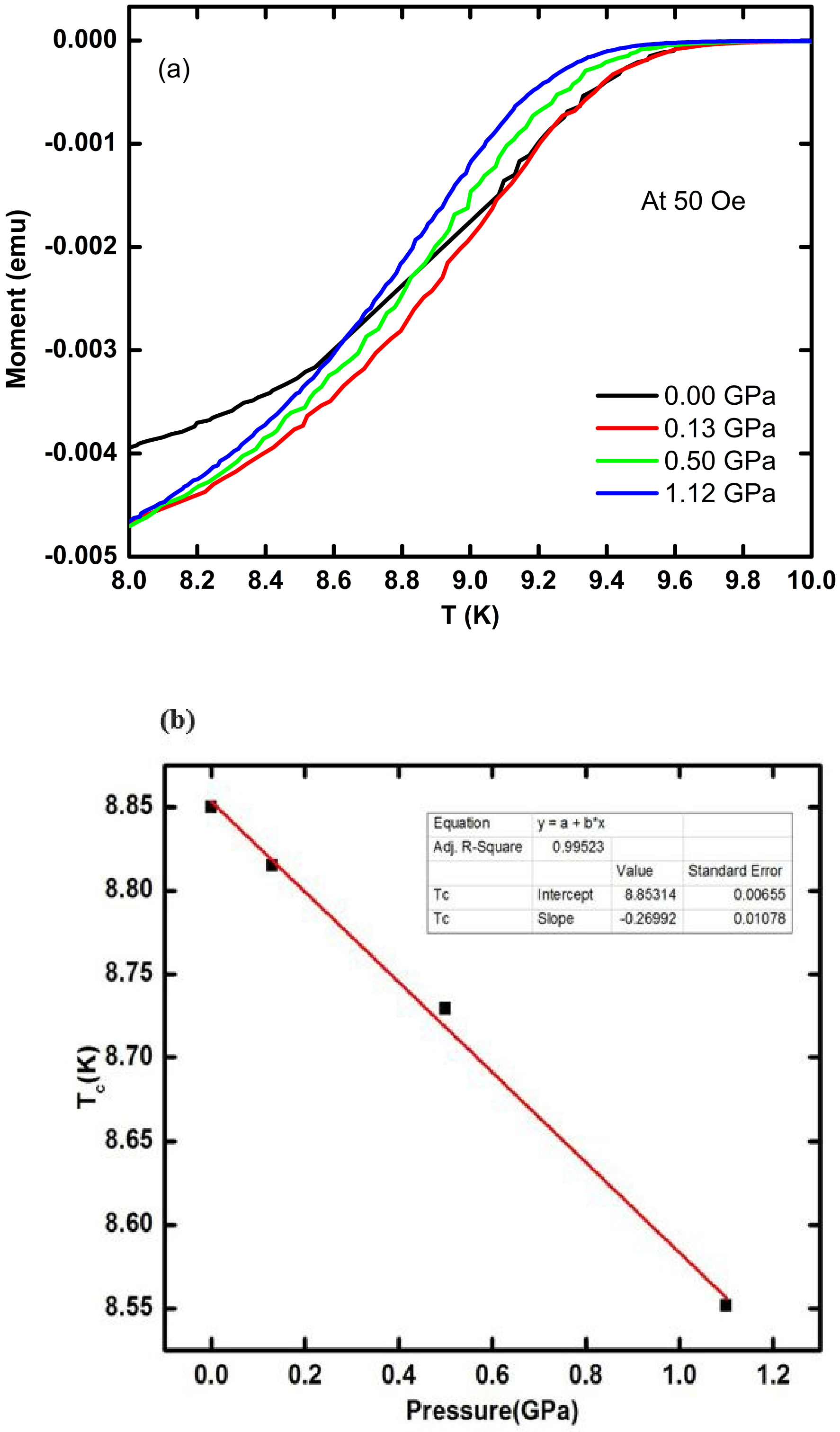

Equation	y = a + b*x		
Adj. R-Square	0.99523		
		Value	Standard Error
Tc	Intercept	8.85314	0.00655
Tc	Slope	-0.26992	0.01078

Figure 4.7: (a) The magnetization M versus temperature T measured at various pressures. (b) The transition temperature T$_c$ versus applied pressure P data extracted from magnetization M versus Temperature T at various pressures.

Oe . Figure 4.7 (a) shows that the T$_c$ for $LuRuB_2$ is suppressed to lower temperatures on increasing pressure and drops below 8.6 K at 1.12 GPa which was the highest pressure possible in our setup. From Eq. (1.40), the superconducting transition temperature for electron-phonon BCS superconductors is related to the lattice spring constant as $T_c \approx \sqrt{k/M} \cdot \exp[-k/\eta]$, where $\eta = N(\varepsilon_F)\left\langle I^2 \right\rangle$ is called the Hopfield parameter and changes very gradually with pressure. The spring constant k rises significantly under pressure. As a result, the drop in the $(-k)$ component of the exponent dominates over the increase in the prefactor $\sqrt{k}$, resulting in a significant fall in T$_c$ with increasing pressure. These data in Figure 4.7 (a) were used to extract the onset T$_c$ for each P. Figure 4.7 (b) shows the P–T phase diagram for LuRuB2 for P $\leq$ 1.2 GPa. We found that the T$_c$ is suppressed almost linearly with pressure at a rate of $\mathrm{d}T_\mathrm{c}/\mathrm{d}P \approx -0.27$ K/GPa. From these findings, we conclude that $LuRuB_2$ is an electron-phonon coupling superconductor.

4.7 Conclusion

In summary, we have synthesized the polycrystalline samples of $LuRuB_2$ and $YRuB_2$ and investigated their properties in the superconducting state. The ρ(T) measurements confirmed the occurrence of superconductivity with a T$_c$ $\approx$ 9.5 K in $LuRuB_2$ and 9.2 K in $YRuB_2$. The magnetic field -temperature (H–T) phase diagram extracted from ρ(T) data in various fields shows a nearly linear trend for both materials. The point contact spectroscopy measurements on $LuRuB_2$ shows the non-BCS temperature dependence of the superconducting gap Δ(T) and a small value of Δ/k$_B$T$_c$ $\approx$ 1 which is less than the BCS value Δ/k$_B$T$_c$= 1.76. These observations point towards the unconventional superconductivity in these compounds. The various superconducting parameters for the $LuRuB_2$ compound have been estimated by analyzing the critical field data in terms of the dirty limit theory of Werthamer, Helfand, and Hohenberg (WHH). For the $YRuB_2$ superconductor, which is in the clean limit, the critical field data are analyzed in terms of the Ginzburg-Landau theory. From the specific heat $C(T)$ data, we have confirmed the bulk superconductivity in $LuRuB_2$. The T = 0 upper critical filed $H_{c2}(0)$ is determined by fitting the H-T data to the empirical relation $H_{c2}(T) = H_{c2}(0)\left[1-\left(\frac{T}{T_c}\right)^{\alpha}\right]$ and is estimated to be 58.6 kOe for $LuRuB_2$ and 45.2 kOe for $YRuB_2$. Additionally, from high pressure magnetic measurements on $LuRuB_2$, we have found that T$_c$ is suppressed to lower temperatures almost linearly with increasing pressure P at a rate $\mathrm{d}T_\mathrm{c}/\mathrm{d}P \approx -0.27$ K/GPa. This suppression of T$_c$ with pressure suggests an electron-phonon mediated superconductivity in these materials. Thus in our investigation, these materials have been found to show conflicting results about the nature (conventional or unconventional) of superconductivity.

CHAPTER 5

Summary and Outlook

5.1 Summary

In this thesis, we have investigated the superconducting properties of rare earth ternary boride $RRuB_2$ (R = Y, Lu) and transition metal boride TB_2 (T = Os, Ru) compounds with the aim of understanding the anomalous behaviors exhibited by these compounds. These materials have layered or quasi-low-dimensional structural motifs, which makes them potential candidates for novel superconductivity. Polycrystalline samples of these compounds were prepared by arc melting. Powder x-ray data showed that the TB_2 (T = Os, Ru) crystallizes in an orthorhombic structure, and the majority of the $RRuB_2$ (R = Y, Lu) sample crystallize in the $LuRuB_2$-type structure with small ($\approx 10\%$) amount of non-superconducting impurity phases. Various experimental techniques such as dc magnetization, resistivity, high pressure, specific heat, and point contact spectroscopic measurements have been performed on these samples. The first-principles density functional theory (DFT) calculations were done for the RuB_2 compound in collaboration.

The first part of this thesis covers the pressure dependence of the superconducting T_c of OsB_2 and a detailed study of bulk superconducting behavior in the isostructural layered transition metal boride RuB_2 with Tc $\approx$ 1.5 K. The T_c for OsB_2 reduces with pressure, supporting an electron-phonon mediated superconductivity. The polycrystalline sample of RuB_2 was subjected to various measurements such as magnetic susceptibility (χ) vs. temperature (T), magnetization (M) vs. the magnetic field (H), resistivity (R) vs. temperature (T), and heat capacity (C) vs. temperature measurements at different fields. The Ginzberg Landau (GL) parameter was found to be $\kappa \approx 0.1$–0.6 showing that RuB_2 is a rare alloy type-I superconductor. A reduced heat capacity anomaly was observed at T_c, which was characterized by $\Delta C/\gamma T_c \approx 1.1$ indicating the presence of multigap superconductivity in this compound. Multigap superconductivity was further supported by the successful fitting of electronic specific heat data to a two-gap superconductivity model with gap values $\Delta/k_BT_c \approx 1.88$ and $\Delta/k_BT_c \approx 1.13$. The M vs. H measurements showed behavior typical of type-1 superconductivity. We also calculate the band structure and obtain the Fermi surface for RuB_2. The Fermi surface consists of one quasi-two-dimensional sheet and two concentric ellipsoidal sheets very similar to OsB_2. An additional small fourth sheet is also found for RuB_2. These calculations also support the possibility of multigap superconductivity in the sample. RuB_2 has thus been shown to be a rare candidate for a two-gap type-1 superconductor.

The second part of this thesis deals with the experimental investigations carried out on (Y, Lu)RuB_2 in their superconducting state. The superconducting state has been thoroughly investigated by employing resistivity (ρ) vs. temperature (T), heat capacity (C) vs. temperature (T), and magnetization (M) vs. temperature (T) measurements at different applied fields. The H_c vs. T phase diagram was constructed from ρ(T) data in various applied fields and was found to show a nearly linear trend for both the samples, suggesting unconventional superconducting behavior. The point contact spectroscopy measurements on $LuRuB_2$ show the small value of $\Delta/k_BT_c \approx 1$ and a non-BCS temperature dependence of Δ(T), which deviates from BCS predictions, suggesting unconventional superconductivity. This supports our conclusions from the H-T phase diagram. Pressure dependent M-T measurements were also carried out on $LuRuB_2$ to check the robustness of the superconducting state under pressure. The application of pressure shifted the T_c to lower temperatures indicating that these materials are electron-phonon coupling superconductors.

5.2 Outlook

The discovery of high T_c superconductivity in MgB_2 with anomalous superconducting behavior and its large-scale applications revived the interest in Boron-containing compounds with similar structures. There is a dispute on whether these anomalous behaviors are caused by a single anisotropic gap or two energy gaps.

The question of whether MgB_2 represents a new class of superconductors is currently being debated. Although in our findings RuB_2 shows two-gap type-I superconductivity, a scenario of anisotropic type-I superconductivity could also be at work in this compound, and further work such as imaging of magnetic flux entering into the material could be helpful in confirming the type of superconductivity. The non-BCS superconducting behaviors of some of the properties in these layered boride compounds are all interesting issues that require further investigation. Future studies of the anisotropic physical properties of single crystals will be very helpful in these regards. These investigations may provide a general protocol for the discovery of other type-I superconducting compounds. Such materials will, in turn, give researchers more direct access to superconductivity regimes away from the common type-II superconductivity mostly observed in alloys, which are particularly interesting in superconductors with multigap or with an anisotropic gap. The High superconducting transition temperatures, as well as the interesting interplay between superconductivity and the magnetic order associated with rare-earth $4f$ electrons are recurrent themes in the rare earth boride compounds. The anomalous behavior of the H-T phase diagram of $RRuB_2$ superconductors needs further investigation, and the single-phase samples of these compounds are required for the study of their intrinsic properties.

Bibliography

[1] J. A. T. Barker, R. P. Singh, A. D. Hillier, and D. M. Paul, Phys. Rev. B **97**, 094506 (2018).

[2] H. KAMERLINGH ONNES, Comm. Phys. Lab. Univ. Leiden **122**, 122 (1911).

[3] W. Meissner and R. Ochsenfeld, Naturwissenschaften **21**, 787 (1933).

[4] C. J. Gorter and H. Casimir, Physica **1**, 306 (1934).

[5] F. London and H. London, Proceedings of the Royal Society of London. Series A - Mathematical and Physical Sciences **149**, 71–88 (1935).

[6] J. N. RJABININ and L. W. SHUBNIKOW, Nature **135**, pages581–582 (1935).

[7] L. D. Landau and V. Ginzburg, Zh. Eksp. Teor. Fiz. **20**, 1064 (1950).

[8] A. A. Abrikosov, Sov. Phys. JETP **5**, 1174 (1957).

[9] E. Maxwell, Phys. Rev. **78**, 477 (1950).

[10] H. Fröhlich, Phys. Rev. **79**, 845 (1950).

[11] J. Bardeen, Physical Review **79**, 167 (1950).

[12] J. Bardeen, L. N. Cooper, and J. R. Schrieffer, Phys. Rev. **106**, 162 (1957).

[13] J. G. Bednorz and K. A. Müller, Zeitschrift für Physik B Condensed Matter **64**, 189 (1986).

[14] P. Monthoux and G. G. Lonzarich, Phys. Rev. B **69**, 064517 (2004).

[15] K. Miyake, S. Schmitt-Rink, and C. M. Varma, Phys. Rev. B **34**, 6554 (1986).

[16] M. Sigrist and K. Ueda, Rev. Mod. Phys. **63**, 239 (1991).

[17] J. Nagamatsu, N. Nakagawa, T. Muranaka, Y. Zenitani, and J. Akimitsu, Nature **410**, 63–64 (2001).

[18] F. Bouquet, R. A. Fisher, N. E. Phillips, D. G. Hinks, and J. D. Jorgensen, Phys. Rev. Lett. **87**, 047001 (2001).

[19] S. V. Shulga, S.-L. Drechsler, G. Fuchs, K.-H. Müller, K. Winzer, M. Heinecke, and K. Krug, Phys. Rev. Lett. **80**, 1730 (1998).

[20] R. Fisher, G. Li, J. Lashley, F. Bouquet, N. Phillips, D. Hinks, J. Jorgensen, and G. Crabtree, Physica C: Superconductivity **385**, 180 (2003).

[21] F. Manzano, A. Carrington, N. E. Hussey, S. Lee, A. Yamamoto, and S. Tajima, Phys. Rev. Lett. **88**, 047002 (2002).

[22] M. Tinkham, *Introduction to superconductivity* (McGraw-Hill, 1996).

[23] A. C. Rose-Innes and E. H. Rhoderick (1969).

[24] A. Pippard, Proceedings of the Royal Society of London **216**, 547–568 (1953).

[25] N. R. Werthamer, E. Helfand, and P. C. Hohenberg, Phys. Rev. **147**, 295 (1966).

[26] in *Collected Papers of L.D. Landau*, edited by D. TER HAAR (Pergamon, 1965) pp. 546–568.

[27] W. A. Little and R. D. Parks, Phys. Rev. Lett. **9**, 9 (1962).

[28] W. H. Kleiner, L. M. Roth, and S. H. Autler, Phys. Rev. **133**, A1226 (1964).

[29] U. Essmann and H. Träuble, Physics Letters A **24**, 526 (1967).

[30] L. N. Cooper, Phys. Rev. **104**, 1189 (1956).

[31] J. Bardeen, L. N. Cooper, and J. R. Schrieffer, Phys. Rev. **108**, 1175 (1957).

[32] L. P. Gor'kov, Sov. Phys. JETP **9**, 1364 (1959).

[33] N. N. Bogolyubov, Nuovo Cim. **7**, 794 (1958).

[34] J. Valatin, Nuovo Cim. **7**, 843–857 (1958).

[35] C. Kittel, *Solid state physics* (Shell Development Co., 1955).

[36] G. Eliashberg, Sov. Phys. JETP. **11**, 966 (1960).

[37] W. L. McMillan, Phys. Rev. **167**, 331 (1968).

[38] J. S. Schilling and J. J. Hamlin, Journal of Physics: Conference Series **121**, 052006 (2008).

[39] K. Shimizu, K. Amaya, and N. Suzuki, Journal of the Physical Society of Japan **74**, 1345–1357 (2005).

[40] J. Hopfield, Physica **55**, 41 (1971).

[41] G. Gaspari and B. Gyorffy, Physical Review Letters **28**, 801 (1972).

[42] B. Lorenz, R. L. Meng, and C. W. Chu, Phys. Rev. B **64**, 012507 (2001).

[43] S. Deemyad, T. Tomita, J. Hamlin, B. Beckett, J. Schilling, D. Hinks, J. Jorgensen, S. Lee, and S. Tajima, Physica C: Superconductivity **385**, 105–116 (2003).

[44] P. W. Anderson and P. Morel, Phys. Rev. **123**, 1911 (1961).

[45] D. J. Van Harlingen, Reviews of Modern Physics **67**, 515 (1995).

[46] H. Suhl, B. T. Matthias, and L. R. Walker, Phys. Rev. Lett. **3**, 552 (1959).

[47] H. J. Choi, D. Roundy, H. Sun, M. L. Cohen, and S. G. Louie, Nature **418**, 758 (2002).

[48] Y. Nakajima, T. Nakagawa, T. Tamegai, and H. Harima, Phys. Rev. Lett. **100**, 157001 (2008).

[49] R. T. Gordon, M. D. Vannette, C. Martin, Y. Nakajima, T. Tamegai, and R. Prozorov, Phys. Rev. B **78**, 024514 (2008).

[50] J. K. Dong, T. Y. Guan, S. Y. Zhou, X. Qiu, L. Ding, C. Zhang, U. Patel, Z. L. Xiao, and S. Y. Li, Phys. Rev. B **80**, 024518 (2009).

[51] J. Xing, H. Lin, Y. Li, S. Li, X. Zhu, H. Yang, and H.-H. Wen, Physical Review B **93** (2016).

[52] M. Tortello, D. Daghero, G. A. Ummarino, V. A. Stepanov, N. D. Zhigadlo, J. Karpinski, J. Jiang, and R. S. Gonnelli, Journal of Superconductivity and Novel Magnetism **25**, 1297 (2012).

[53] C. Buzea and T. Yamashita, Superconductor Science and Technology **14**, R115 (2001).

[54] Y. Singh, A. Niazi, M. D. Vannette, R. Prozorov, and D. C. Johnston, Phys. Rev. B **76**, 214510 (2007).

[55] J. Vandenberg, B. Matthias, E. Corenzwit, and H. Barz, Materials Research Bulletin **10**, 889 (1975).

[56] D. Kaczorowski, A. J. Zaleski, O. J. Zogal, and J. Klamut, Incipient superconductivity in tab$_2$ (2001), arXiv:cond-mat/0103571 [cond-mat.supr-con] .

[57] V. A. Gasparov, N. S. Sidorov, I. I. Zver'kova, and M. P. Kulakov, Journal of Experimental and Theoretical Physics Letters **73**, 532 (2001).

[58] H. Rosner, W. E. Pickett, S.-L. Drechsler, A. Handstein, G. Behr, G. Fuchs, K. Nenkov, K.-H. Müller, and H. Eschrig, Phys. Rev. B **64**, 144516 (2001).

[59] Y. Wang, T. Plackowski, and A. Junod, Physica C: Superconductivity **355**, 179 (2001).

[60] P. Szabó, P. Samuely, J. Kačmarčík, T. Klein, J. Marcus, D. Fruchart, S. Miraglia, C. Marcenat, and A. G. M. Jansen, Phys. Rev. Lett. **87**, 137005 (2001).

[61] F. Giubileo, D. Roditchev, W. Sacks, R. Lamy, D. X. Thanh, J. Klein, S. Miraglia, D. Fruchart, J. Marcus, and P. Monod, Phys. Rev. Lett. **87**, 177008 (2001).

[62] S. Tsuda, T. Yokoya, T. Kiss, Y. Takano, K. Togano, H. Kito, H. Ihara, and S. Shin, Phys. Rev. Lett. **87**, 177006 (2001).

[63] X. K. Chen, M. J. Konstantinović, J. C. Irwin, D. D. Lawrie, and J. P. Franck, Phys. Rev. Lett. **87**, 157002 (2001).

[64] Y. Singh, C. Martin, S. L. Bud'ko, A. Ellern, R. Prozorov, and D. C. Johnston, Phys. Rev. B **82**, 144532 (2010).

[65] J. Bekaert, S. Vercauteren, A. Aperis, L. Komendová, R. Prozorov, B. Partoens, and M. V. Milošević, Phys. Rev. B **94**, 144506 (2016).

[66] C. Wolowiec, B. White, and M. Maple, Physica C: Superconductivity and its Applications **514**, 113 (2015), superconducting Materials: Conventional, Unconventional and Undetermined.

[67] H. Ku and R. Shelton, Materials Research Bulletin **15**, 1441 (1980).

[68] W. H. Lee, S. Appl, and R. N. Shelton, Journal of Low Temperature Physics **68**, 147 (1987).

[69] L. Mo, in *Carbon Dioxide Sequestration in Cementitious Construction Materials*, Woodhead Publishing Series in Civil and Structural Engineering, edited by F. Pacheco-Torgal, C. Shi, and A. P. Sanchez (Woodhead Publishing, 2018) pp. 175–197.

[70] C. G. Pope, Journal of Chemical Education **74**, 129 (1997).

[71] B. H. Toby, Journal of Applied Crystallography **34**, 210 (2001).

[72] ASTM. (American Society for Testing & Materials, 1990).

[73] S. Foner, Review of Scientific Instruments **30**, 548 (1959).

[74] T. H. K. Barron and G. K. White, *Heat Capacity and Thermal Expansion at Low Temperatures* (Springer US, 1999).

[75] Y. Naidyuk and I. Yanson, *Point-contact spectroscopy* (Springer New York).

[76] F. Laube, G. Goll, H. v. Löhneysen, M. Fogelström, and F. Lichtenberg, Phys. Rev. Lett. **84**, 1595 (2000).

[77] A. Andreev, .

[78] G. Blonder, m. M. Tinkham, and k. T. Klapwijk, Physical Review B **25**, 4515 (1982).

[79] E. Boaknin, M. A. Tanatar, J. Paglione, D. Hawthorn, F. Ronning, R. W. Hill, M. Sutherland, L. Taillefer, J. Sonier, S. M. Hayden, and J. W. Brill, Phys. Rev. Lett. **90**, 117003 (2003).

[80] S. V. Shulga, S.-L. Drechsler, G. Fuchs, K.-H. Müller, K. Winzer, M. Heinecke, and K. Krug, Phys. Rev. Lett. **80**, 1730 (1998).

[81] Y. Maeno, T. M. Rice, and M. Sigrist, Physics Today **54**, 42 (2001), https://doi.org/10.1063/1.1349611 .

[82] M. L. Amigó, V. A. Crivillero, D. G. Franco, and G. Nieva, Journal of Physics: Conference Series **568**, 022005 (2014).

[83] S. L. Bud'ko, G. Lapertot, C. Petrovic, C. E. Cunningham, N. Anderson, and P. C. Canfield, Phys. Rev. Lett. **86**, 1877 (2001).

[84] Z. X. Shi, M. Tokunaga, T. Tamegai, Y. Takano, K. Togano, H. Kito, and H. Ihara, Phys. Rev. B **68**, 104513 (2003).

[85] F. Manzano, A. Carrington, N. E. Hussey, S. Lee, A. Yamamoto, and S. Tajima, Phys. Rev. Lett. **88**, 047002 (2002).

[86] E. A. Yelland, J. R. Cooper, A. Carrington, N. E. Hussey, P. J. Meeson, S. Lee, A. Yamamoto, and S. Tajima, Phys. Rev. Lett. **88**, 217002 (2002).

[87] M. Hebbache, physica status solidi (RRL) – Rapid Research Letters **3**, 163 (2009), https://onlinelibrary.wiley.com/doi/pdf/10.1002/pssr.200903133 .

[88] P. Giannozzi, S. Baroni, N. Bonini, M. Calandra, R. Car, C. Cavazzoni, D. Ceresoli, G. L. Chiarotti, M. Cococcioni, I. Dabo, A. D. Corso, S. de Gironcoli, S. Fabris, G. Fratesi, R. Gebauer, U. Gerstmann, C. Gougoussis, A. Kokalj, M. Lazzeri, L. Martin-Samos, N. Marzari, F. Mauri, R. Mazzarello, S. Paolini, A. Pasquarello, L. Paulatto, C. Sbraccia, S. Scandolo, G. Sclauzero, A. P. Seitsonen, A. Smogunov, P. Umari, and R. M. Wentzcovitch, Journal of Physics: Condensed Matter **21**, 395502 (2009).

[89] J. P. Perdew, K. Burke, and M. Ernzerhof, Phys. Rev. Lett. **77**, 3865 (1996).

[90] C. P. Poole, *Superconductivity* (Elsevier, 2007).

[91] F. Bouquet, Y. Wang, R. A. Fisher, D. G. Hinks, J. D. Jorgensen, A. Junod, and N. E. Phillips, Europhysics Letters (EPL) **56**, 856 (2001).

[92] V. Kresin and S. Wolf, Physica C: Superconductivity **169**, 476 (1990).

[93] E. Svanidze and E. Morosan, Phys. Rev. B **85**, 174514 (2012).

[94] S. Yonezawa and Y. Maeno, Phys. Rev. B **72**, 180504 (2005).

[95] L. L. Zhao, S. Lausberg, H. Kim, M. A. Tanatar, M. Brando, R. Prozorov, and E. Morosan, Phys. Rev. B **85**, 214526 (2012).

[96] W. Yue-Qin, Y. Lan-Feng, and Y. Jin-Long, Chinese Physics Letters **25**, 3036 (2008).

[97] W. E. Pickett, Brazilian Journal of Physics **33**, 695–699 (2003).

[98] S. Datta, A. Vasdev, S. Halder, J. Singh, Y. Singh, and G. Sheet, Journal of Physics: Condensed Matter **32**, 315701 (2020).

[99] M. Kriener, Y. Maeno, T. Oguchi, Z.-A. Ren, J. Kato, T. Muranaka, and J. Akimitsu, Phys. Rev. B **78**, 024517 (2008).

[100] C. Horvath and P. Rogl, Materials Research Bulletin **20**, 1273 (1985).

[101] B. T. Matthias, E. Corenzwit, J. M. Vandenberg, and H. E. Barz, Proceedings of the National Academy of Sciences **74**, 1334–1335 (1977).

[102] J. Vandenberg and B. Matthias, Proceedings of the National Academy of Sciences of the United States of America **74**, 1336 (1977).

[103] K. Yvon and D. Johnston, Acta Crystallographica Section B: Structural Crystallography and Crystal Chemistry **38**, 247 (1982).

[104] M. B. Maple and O. Fischer, *Superconductivity in ternary compounds II: Superconductivity and magnetism* (Springer-Verlag, 1982).

[105] R. Shelton, B. Karcher, D. Powell, R. Jacobson, and H. Ku, Materials Research Bulletin **15**, 1445 (1980).

[106] Y. Kishimoto, T. Ohno, and T. Kanashiro, Journal of the Physical Society of Japan **64**, 1275 (1995).

[107] Y. Kishimoto, T. Ohno, T. Hihara, K. Sumiyama, and K. Suzuki, Physical Review B **64**, 024509 (2001).

[108] Y. Kishimoto, Y. Kawasaki, Y. Ideta, S. Endou, T. Tanaka, M. Tanabe, T. Ohno, G. Ghosh, A. Tyagi, and L. C. Gupta, in *Journal of Physics: Conference Series*, Vol. 176 (IOP Publishing, 2009) p. 012039.

[109] A. Hillier and R. Cywinski, Applied Magnetic Resonance **13**, 95 (1997).

[110] R. N. Shelton and H. E. Horng, Phys. Rev. B **33**, 1671 (1986).

[111] N. Werthamer, E. Helfand, and P. Hohenberg, Physical Review **147**, 295 (1966).

[112] K. Maki, Physics Physique Fizika **1**, 21 (1964).

[113] E. Helfand and N. R. Werthamer, Phys. Rev. **147**, 288 (1966).

[114] P. G. Gennes, Physik der Kondensierten Materie **3**, 79–90 (1964).

[115] T. P. Orlando, E. J. McNiff, S. Foner, and M. R. Beasley, Phys. Rev. B **19**, 4545 (1979).

[116] A. M. Clogston, Physical Review Letters **9**, 266 (1962).